Damage assessment of highly-loaded low-speed roller bearings with acoustic emission monitoring

A full-scale laboratory evaluation

Thakoerdajal, N.P.

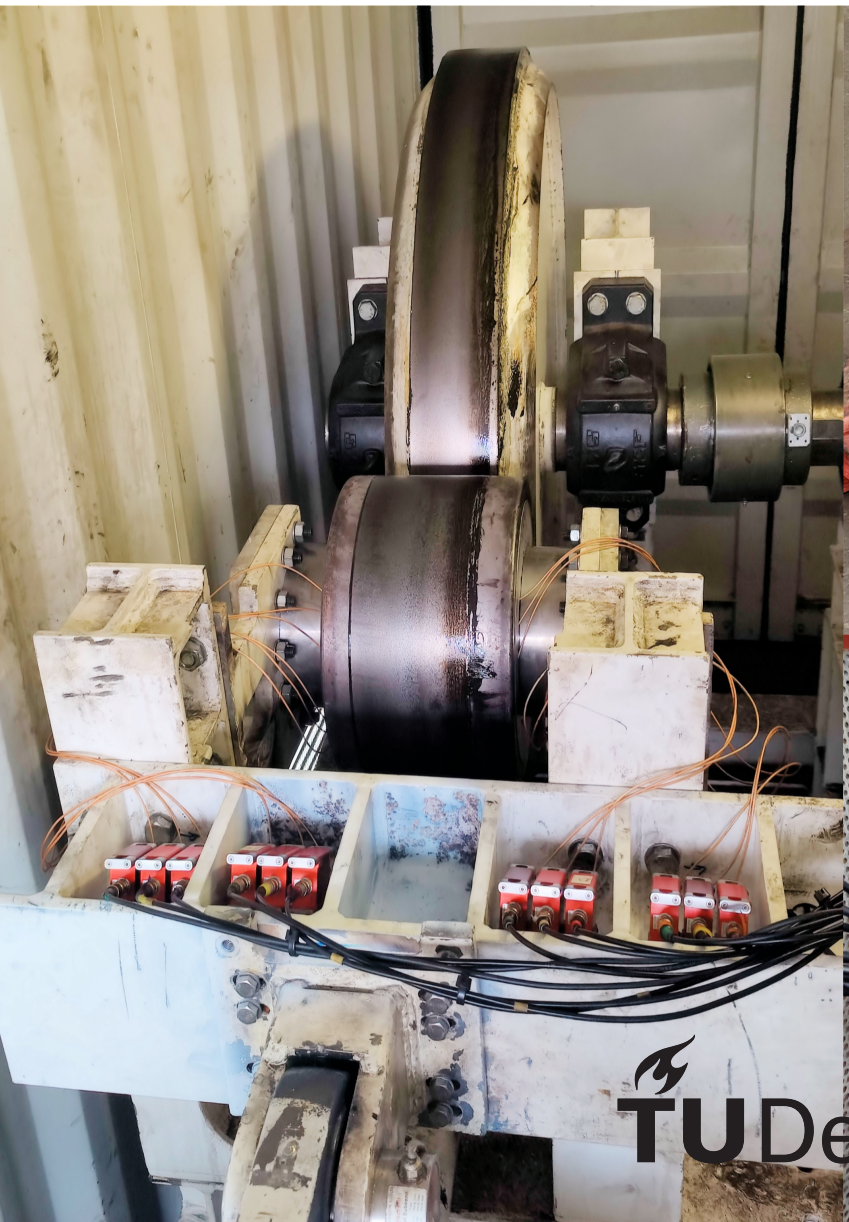

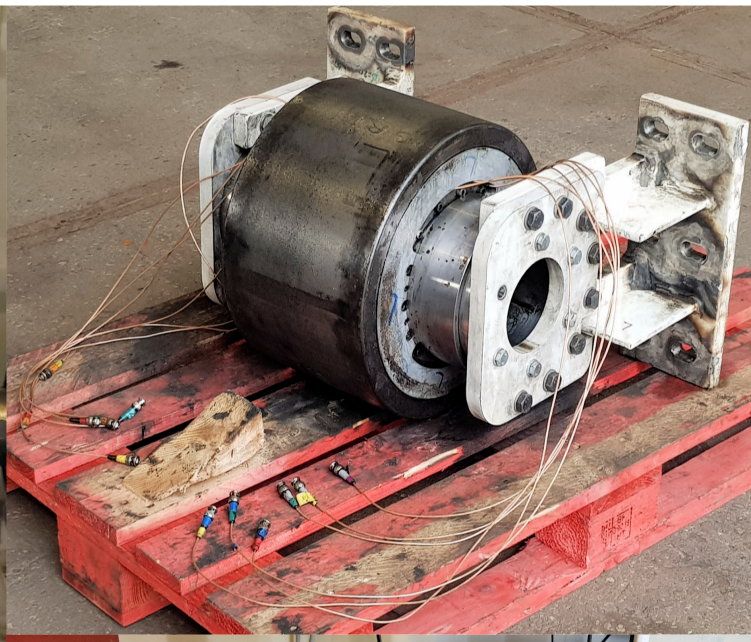

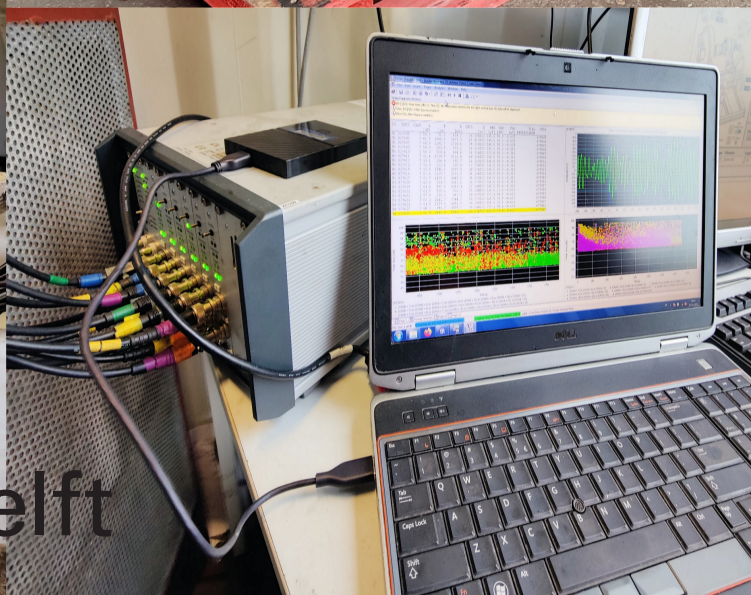

TU Delft

Damage assessment of highly-loaded low-speed roller bearings with acoustic emission monitoring

A full-scale laboratory evaluation

by

Thakoerdajal, N.P.

To obtain the degree of Master of Science in
Offshore and Dredging Engineering

with specialisation in Structural Analysis and Design
at the Delft University of Technology,
to be defended on Monday February 28, 2022 at 9:00.

Student number: 4549678

Thesis committee:		
	Dr. L. Pahlavan,	TU Delft, Supervisor, Chair
	Ir. B. Scheeren,	TU Delft, Daily supervisor
	Prof. Dr. Ir. J. Sietsma,	TU Delft
	Dr. C.L. Walters,	TU Delft
	Ir. A. Smit,	Allseas, Supervisor

This thesis is confidential and cannot be made public until Feb 28, 2024.

HiTeAM TU Delft Allseas

Preface and Acknowledgements

As part of my master program Offshore and Dredging Engineering, a research was conducted on the topic of '*Damage assessment of highly-loaded low-speed roller bearings with acoustic emission monitoring*' in a full-scale laboratory evaluation and was carried out in collaboration with the Innovation's department of Allseas Engineering.

During this research, I have learned a lot of new skills and was able to develop myself professionally as well as personally. Designing machine components and preparing drawings for the fabrication shop was something in which I became more skilled at with help of my colleagues at Allseas. In addition, structural strength analysis with Finite Element Modelling was a new skill I have learned which I will be able to apply in my future work. During the preparation and execution of the experiments, I learned a lot of practical skills for example installation, lifting and disassembly of heavy equipment, and ways to work safely. Furthermore, I have gained more understanding and experience with acoustic emission while performing the measurements and during the processing of the measurement data. Finally, I was able to learn more about my future work as an engineer by my colleagues at Allseas.

Many persons from Allseas Engineering, TU Delft, BOYS yard and Machinefabriek Schaap have helped me during my research which I am very grateful for. I have also learned a lot from them, which I will carry with me for a lifetime. There are too many names to mention, however there are some persons who I would like to give special attention.

First, I would like to thank Pooria Pahlavan and Bart Scheeren for introducing me to this amazingly interesting research topic and engaging me in the HiTeAM project and meetings. I have learned a lot from you about acoustic emission, presenting my findings to public and much more. You were always at anytime available for me for discussions and feedback. I am grateful for your guidance, valuable feedback and willingness for assistance and support. In particular, I would like to thank Bart for all his support during the data processing of the measurements and I am grateful that I was able to drop by your office for a technical discussion anytime.

Furthermore, I would like to thank Adriaan Smit for all his guidance, support and feedback for all engineering and experimental work. I have learned a lot of the engineering work and many things more from you which I cannot express in a few words and I am grateful that I was able to learn from an experienced engineer as you. Also, I am thankful for the introduction and warm welcome you gave in Allseas.

I would also like to thank Micheal Dauda for all his help during performing of the experiments. We have faced quite some challenges and you always motivated me and gave positive energy when things were not going according to plan.

Finally, I would like to thank my family and friends but in particular my parents and brother for their support.

Nitesh Thakoerdajal
Delft, February 2022

Abstract

Highly-loaded low-speed roller bearings are frequently used in equipment offshore e.g. slew bearings in cranes, sheave bearings and FPSO turret bearings. Reducing maintenance costs, increasing productivity, ensuring safety of people and structural integrity and longevity assurance of equipment can be achieved by the condition monitoring of highly-loaded low-speed roller bearings. Condition monitoring using conventional methods e.g. vibration-based monitoring and strain monitoring are not suitable for these low speed applications. Currently, very limited research is performed in the field of condition monitoring with acoustic emission (AE) monitoring for highly-loaded low-speed (<10 rpm) bearings with naturally developed damage.

In this research, the applicability of AE monitoring for damage assessment of highly-loaded low-speed roller bearings is investigated in a full-scale duration test. Furthermore, the influence of contaminated lubricant with steel particles is investigated in the contamination test to study the feasibility of real-time detection of contaminated lubricant during operations, and as a supporting technique for wear debris analysis in lubricant.

From the results, an increase in AE activity expressed in hit-rates is observed for a wide frequency band of 40 - 580 kHz during the duration test where the L_{10} is consumed from 40 to 50%. Wear development in the bearing is observed during visual inspection and has been quantified with lubrication analysis.

A safety limit and an operational limit have been defined with the results of the baseline and duration tests. This research suggests that AE monitoring can be applied on highly-loaded low-speed bearings to assess the damage for representative operational conditions.

From the results of the lubricant contamination test, an increased AE activity of continuous waves for bearing speed levels of 0.15 m/s (7.5 RPM) and 1.25 m/s (60 RPM) with respect to higher lubricant contamination levels were observed. Furthermore with a proper choice of the SNR-threshold, there is no major masking effect of acoustic emission signals due to contaminated lubricant. The results of the contamination tests indicate that contaminated lubricant can be detected with AE monitoring. More research with naturally developed contamination of wear debris in lubricant and its influence on AE is recommended for the future work in preparation for the real application.

Contents

Preface i

Abstract ii

Nomenclature v

List of Figures vii

List of Tables x

1 Introduction 1
- 1.1 HiTeAM JIP . . . 2
- 1.2 Scope of research . . . 2
- 1.3 Layout . . . 2

2 Literature review 3
- 2.1 Roller element bearings and its failure . . . 3
  - 2.1.1 Failure of roller bearings . . . 4
- 2.2 Condition monitoring . . . 10
  - 2.2.1 Vibration-based monitoring . . . 11
  - 2.2.2 Lubrication analysis . . . 14
  - 2.2.3 Acoustic Emission . . . 14

3 Knowledge gap and research questions 21
- 3.1 Knowledge gap . . . 21
  - 3.1.1 Damage assessment of roller bearings with AE . . . 21
  - 3.1.2 Assessment of contamination in roller bearings with AE . . . 22
- 3.2 Research questions . . . 22

4 Methodology 23
- 4.1 Test specimen . . . 24
- 4.2 Preparation of the test set up . . . 27
  - 4.2.1 Modification of test set up . . . 28
- 4.3 Lifetime prediction . . . 31
- 4.4 Test plan . . . 35
- 4.5 Measurement system . . . 37
- 4.6 Data processing methods . . . 40
  - 4.6.1 Pre-processing . . . 40
  - 4.6.2 Processing . . . 41
  - 4.6.3 Post-processing . . . 42

5 Results and discussion 43
- 5.1 Baseline test . . . 43
- 5.2 Test on slightly worn side inner ring . . . 45
- 5.3 Duration test . . . 46
  - 5.3.1 Samples of waveforms . . . 48
  - 5.3.2 Clustering . . . 48
  - 5.3.3 Visual inspection . . . 50
  - 5.3.4 Lubrication samples . . . 51

5.4 Contamination test 55

6 Conclusion and recommendation 58
6.1 Conclusion 58
6.2 Recommendations 59

References 68

A Pictures of bearing parts and failures test set up 69
A.1 Pictures visual inspection during baseline test 69
A.1.1 Dye penetrant test during baseline test 71
A.2 Visual inspection after duration test 72
A.2.1 Dye penetrant test after duration test 74
A.3 Visual inspection contamination test. 74
A.3.1 Pictures bearing before testing 75
A.3.2 Pictures bearing after contamination tests 75
A.4 Failed components of test set up 76

B Appendix B: Results of FEM analyses 78
B.1 Contact stress of modified test wheel 78
B.2 Contact stress of inner ring raceway and roller 79

C Additional results of data processing 81
C.1 Histograms contamination test results. 81

Nomenclature

Abbreviations

Abbreviation	Definition
3mE	Mechanical, Maritime and Materials engineering
AE	Acoustic Emission
CM	Condition Monitoring
FPSO	Floating Production Storage and Offloading
HiTeAM	High-Tech Acoustic Monitoring
ISO	International Standard Organisation
JIP	Joint Industry Project
MTT	Maritime and Transportation Technology
OBS	Outboard Support
O&M	Operation and Maintenance
PTFE	PolyTetraFluoroEthylene
ROI	Return of Investment
SAOS	Ship and Offshore Structures
TLS	Topside Lift System

Symbols

Symbol	Definition	Unit
$B_{bearing}$	Bearing width	[m]
b	Effective half contact width	[m]
b_m	Rating factor	[-]
F_{BPI}	Roller pass frequency inner raceway	[Hz]
F_{BPO}	Roller pass frequency outer raceway	[Hz]
F_{BS}	Roller spin frequency	[Hz]
C_r	Basic dynamic radial load rating	[N]
D_b	Roller diameter bearing	[m]
D_I	Transfer function of coupling between inner raceway and sensor	[-]
D_{pw}	Pitch diameter bearing	[m]
D_O	Transfer function of coupling between outer raceway and sensor	[-]
D_o	Outer diameter bearing	[m]
D_{we}	Diameter roller	[-]
E	E-modulus	[MPa]
f_c	Geometry factor	[-]
i	Number of rows in bearing	[-]
N_b	Number of rolling elements	[-]
$M_{bearing}$	Bearing mass	[kg]
P_{II}	transfer function between the source S_I and sensor at inner ring.	[-]
P_{OI}	transfer function between the source S_I and sensor at outer ring.	[-]
P_m	Mean contact stress	[MPa]
P_{max}	Maximum contact pressure	[MPa]
$P_{m,c}$	Maximum permissible contact pressure	[MPa]
P_r	Dynamic equivalent radial load	[N]
L_{10}	Basic rating lifetime	[-]
L_{we}	Effective roller length	[m]
R'	Effective radius	[m]
$R_{p,0.2}$	Yield strength	[MPa]
S_I	AE source at inner ring	[-]
T	Transmission function interfaces bearing	[-]
t_i	Thickness inner ring	[m]
t_o	Thickness outer ring	[m]
W	Transfer function of wave propagation function through parts in bearing	[-]
Z	Number of rollers	[-]
α	Contact angle between roller and raceway	[rad]
τ_{max}	Maximum contact shear stress	[MPa]
$\tau_{max,c}$	Maximum permissible contact shear stress	[MPa]

List of Figures

2.1 Overview of roller and ball bearing components [12] . . . 3
2.2 Example of a slew bearing [13] . . . 4
2.3 Bearing life and failure data according to [20] . . . 5
2.4 Bearing damage classification according to ISO 15243 [23] . . . 6
2.5 Example of subsurface fatigue development over number of cycles [20] . . . 7
2.6 Example of surface initiated fatigue on raceway [20] . . . 7
2.7 Variable compliance: The rollers acts as springs in the bearing and once the roller pass out the loaded area, a slight downward movement of the inner ring in the direction of the load is created. When a roller passes the loaded area gain, the inner ring moves upward. A relative motion is created. [59] . . . 12
2.8 An example of the RMS vibration level with a comparison between a healthy and damage bearing. The peaks in the right graph provides an indication of possible defects. [59] . . . 13
2.9 An example of a frequency spectrum derived from a vibrations measurement by [59]. Peaks at specific frequencies provides an indication of possible defects at a typical location 13
2.10 An example of a envelope spectrum derived from a vibrations measurement by [59]. A peak at 62.5 Hz and it multiples are highlighted in the graph. This frequency is typical for damage of the rolling element in the bearing. . . . 13
2.11 Overview of AE measurement system [88], AE sensor (left), AE pre-amplifier (center), AE signal processor (right) . . . 15
2.12 An example of a burst type of wave . . . 15
2.13 Wave transmission path [91] . . . 16
2.14 Overview of AE parameters [8] . . . 17
2.15 Number of studies performed with respect to the bearing speed and type of damage [8] 19
2.16 Number of hits with respect to the concentration level of steel M2 particles. [122] . . . 19

4.1 Allseas' Pioneering Spirit . . . 24
4.2 Lifted platform by TLS . . . 24
4.3 Outboard support TLS, yellow circle shows the location of the bearings . . . 24
4.4 Zoomed in picture of the TLS OBS bearings . . . 24
4.5 Slightly worn side on the inner ring . . . 25
4.6 180 degrees rotated inner ring, no wear visible . . . 25
4.7 Raceway of outer ring, 1st inspection. Wear visible on raceway . . . 25
4.8 Test specimen: TLS OBS wheel . . . 26
4.9 3D cross-section of test specimen . . . 26
4.10 2D cross-section of test specimen . . . 26
4.11 2D drawing of original test set up for rollerbox coating testing . . . 27
4.12 Drawing of test set up for roller bearing . . . 28
4.13 Front view test set up . . . 28
4.14 2D drawings of bearing support, (left-top) front view with reference to detail view, (left-bottom) detail view of connection between bearing supporting frame, spacer and shaft, (right-top) isometric view of bearing support and (right-bottom) cross-section at location A-A of bearing support. . . . 30
4.15 FEM analysis of a 300 mm bearing supported on a rail . . . 32
4.16 FEM analysis of a 300 mm bearing radially supported . . . 32

4.17 3D view of roller configuration . . . 32
4.18 Top view of first raceway roller configuration in bearing . . . 32
4.19 Relation between number of steel rollers, basic dynamic load rating C_r and basic rating lifetime L_{10} . . . 33
4.20 FEA of outer ring, VM-stress plotted for outer side. Max. VM-stress = 280 MPa . . . 33
4.21 FEA of outer ring, VM-stress plotted for inner side. Max. VM-stress = 430 MPa . . . 33
4.22 FEM model of test specimen to determine the contact stress, (left) front view bearing model; colors represents bearing parts, (center) isometric view of model and (right) fixed plate geometry . . . 34
4.23 Results for the maximum contact pressure with respect to applied load for FEM and analytical solution . . . 34
4.24 Specification of grease sample locations . . . 36
4.25 AE measurement system installed in test set up . . . 37
4.26 AMSY-6 Measurement system - real time measurement . . . 37
4.27 Sensor responses for the R6α, R15α and WSα . . . 38
4.28 Sensor positioning in set up and its numbering . . . 39
4.29 A set of sensors mounted on the inner ring . . . 39

5.1 Average hitrate baseline test for all test conditions . . . 44
5.2 Average hitrate for baseline test on slightly worn side for all test conditions . . . 45
5.3 Average hitrate during duration test per 1500 cycles for 60 RPM and per 190 cycles for 7.5 RPM . . . 46
5.4 Average hitrate during duration test per 1500 cycles for 60 RPM only . . . 47
5.5 Wave propagation path of the AE source from the failed weld location . . . 47
5.6 Samples of waveforms at specific intervals during duration test, $R6\alpha$ - Ch. 8, $R15\alpha$ - Ch.10 and $WS\alpha$ - Ch. 12 . . . 48
5.7 Clusters originating from channel 5,6 and 12 (High-frequency WSa-sensor) emitted between 10,000 cycles to 18,000 . . . 49
5.8 Clusters between 30,000 and 33,000 cycles for channels 3,5,8,9 and 10 (all frequency types) . . . 49
5.9 Clusters between 50,000 - 53,000 cycles for channels 1,3,5,6,8,9,10,11 and 12. -contains all frequencies . . . 50
5.10 Picture of unworn side of inner ring before duration test. . . . 51
5.11 Picture of worn side of inner ring before duration test. . . . 51
5.12 Developed wear on inner ring with respect to picture 5.10, no wear was present before test. . . . 51
5.13 More development of wear on inner ring with respect to picture 5.11. . . . 51
5.14 Lubrication contamination test: hitrates of raw signals (SNR=0) . . . 55
5.15 Lubrication contamination test: hitrates of burst type signals for SNR-threshold 15 . . . 56
5.16 Lubrication contamination test: hitrates of continuous type signals for SNR-threshold 15 56

A.1 Rollers after first intervention per raceway, from left to right taken as reference from figure 4.25 . . . 69
A.2 Rollers from first raceway . . . 70
A.3 Rollers from second raceway . . . 70
A.4 Rollers from third raceway . . . 70
A.5 Rollers from fourth raceway . . . 70
A.6 Outer ring first picture . . . 70
A.7 Outer ring second picture . . . 70
A.8 Inner ring worn side, taken as reference, 0 degrees . . . 70
A.9 Inner ring, 90 degrees rotated from A.8 . . . 70
A.10 Inner ring, 180 degrees rotated . . . 70
A.11 Inner ring, 270 degrees rotated . . . 70
A.12 One of the flanges . . . 71
A.13 NDT on Inner ring worn side, taken as reference, 0 degrees . . . 71
A.14 NDT Inner ring, 90 degrees rotated from A.8 . . . 71

A.15 Inner ring, 180 degrees rotated . . . 71
A.16 NDT Inner ring, 270 degrees rotated . . . 71
A.17 NDT outer ring . . . 72
A.18 Rollers after duration test shown per raceway. Sorted positioning from most left raceway to most right raceway. Directions left and right are taken as reference from figure 4.25. . . 72
A.19 Roller from first raceway, after duration test. . . . 73
A.20 Roller from second raceway, after duration test. . . . 73
A.21 Roller from third raceway, after duration test. . . . 73
A.22 Roller from fourth raceway, after duration test. . . . 73
A.23 Outer ring raceways, after duration test . . . 73
A.24 Outer ring close up picture of developed wear at raceways . . . 73
A.25 Inner ring worn side, taken as reference, 0 degrees. After duration test . . . 73
A.26 Inner ring, 90 degrees rotated from A.25 . . . 73
A.27 Inner ring, 180 degrees rotated . . . 73
A.28 Inner ring, 270 degrees rotated . . . 73
A.29 One of the flanges after duration test . . . 74
A.30 NDT on Inner ring worn side, taken as reference, 0 degrees . . . 74
A.31 NDT Inner ring, 90 degrees rotated from A.25 . . . 74
A.32 Inner ring, 180 degrees rotated . . . 74
A.33 NDT Inner ring, 270 degrees rotated . . . 74
A.34 NDT outer ring . . . 74
A.35 Worn side of the inner ring taken as reference at 0 degrees. Damage state before contamination test . . . 75
A.36 Inner ring contamination test, 90 degrees rotated from A.35 . . . 75
A.37 Inner ring contamination test, 180 degrees rotated from A.35 . . . 75
A.38 Inner ring contamination test, 270 degrees rotated from A.35 . . . 75
A.39 Outer ring of contamination test; Left view . . . 75
A.40 Outer ring of contamination test; Right view . . . 75
A.41 Worn side of the inner ring taken as reference at 0 degrees. Damage state after contamination test . . . 75
A.42 Inner ring contamination test, 90 degrees rotated from A.41 . . . 75
A.43 Inner ring contamination test, 180 degrees rotated from A.41 . . . 75
A.44 Inner ring contamination test, 270 degrees rotated from A.41 . . . 75
A.45 Outer ring after contamination test; Left view . . . 76
A.46 Outer ring after contamination test; Right view . . . 76
A.47 Warped cylinder hinge connection beam . . . 76
A.48 New design of cylinder hinge connection beam . . . 76
A.49 Failure of test wheel: welded connection between wheel structure and shaft broken . . . 76
A.50 New designed test wheel . . . 77

B.1 General model of finite element analysis of contact stress between test wheel en bearing 78
B.2 Results of FEA contact stress between test wheel and bearing . . . 78
B.3 Location of applied load on FEM model contact stress calculation modified test wheel . 79
B.4 FEM model of test specimen to determine the contact stress, (left) front view bearing model; colors represents bearing parts, (center) isometric view of model and (right) fixed plate geometry . . . 79
B.5 Results of FEA contact stress on the inner ring of the bearing . . . 80
B.6 Results of FEA contact stress on the inner ring of the bearing, zoomed in picture of figure B.5 . . . 80

C.1 Lubrication contamination test: hitrates of burst type signals for SNR 2 . . . 81
C.2 Lubrication contamination test: hitrates of continuous type signals for SNR 2 . . . 82
C.3 Lubrication contamination test: hitrates of burst type signals for SNR 5 . . . 82
C.4 Lubrication contamination test: hitrates of continuous type signals for SNR 5 . . . 83

List of Tables

4.1 Parameters of TLS wheel [127] 26
4.2 Test matrix for baseline test and test on slightly worn side of inner ring 35
4.3 Test matrix contamination test 37

5.1 Main parameters from grease analysis after duration test 52
5.2 Limits of contamination levels for slew bearings [135],[136] and [137] 52

Chapter 1

Introduction

Structural integrity and longevity assurance of highly-loaded low-speed roller bearings are of special interest for operators in the offshore industry [1] [2]. Due to unpredictable high loading conditions, manufacturing defects, improper assembly, installation and maintenance or operation, bearings can get damaged. Inspection of these bearings is often challenging since it is difficult to access them and, furthermore disassembly for inspection results in downtime and risks of damaging the bearing. Also, environmental risks are present and workers are exposed to safety risks.

Nowadays, predictive maintenance strategies for machine components are becoming more interesting for machine owners and operators to efficiently use its lifetime [3],[4],[5]. One of the main types of predictive maintenance techniques, so called condition monitoring can be used to detect early faults, failures and wear of machine components by constantly observing certain parameters i.e. vibration and temperature. The major advantage of this strategy is that the operation and maintenance costs can be reduced in comparison with the nowadays commonly used proactive maintenance strategy. It can support in keeping productive progress smooth, and prevent unplanned downtime and economic loss. Furthermore, maintenance intervals can be extended, which results in less downtime and costs and higher production efficiencies. Safety risks and environmental concerns are reduced since very few inspection and replacements needs to be performed and machine operators are more sustainable making use of their equipment. Additionally, condition monitoring can be of additional value in the enhancement of the development of a more modern equipment manufacturing industry; more insights will be developed in the root cause of failure which can be forwarded as feedback to manufacturers which can eventually improve the quality of their products [1]. From the offshore industry, there is a need to reduce operation and maintenance costs of which predictive maintenance techniques can be helpful to achieve this [6]. By reducing O&M costs, the return of investment increases which makes it more attractive for the industry to invest in projects [7].

Several industrial parties have joined their forces to conduct research on the condition monitoring of roller element bearings with acoustic emission monitoring. Together with the TU Delft, the High-Tech Acoustic Monitoring (HiTeAM) Joint Industry Project (JIP) has been established. With this ultrasonic monitoring technique, the health of these types of bearings will be continuously monitored and will warn the operator in case the bearing is severely damage and unsafe to operate.

1.1 HiTeAM JIP

HiTeAM is a Joint Industry Project originated by the Ship and Offshore Structures (SAOS), section of the Maritime and Transportation Technology (MTT) of the faculty Mechanical, Maritime and Materials engineering (3mE) from the Technical University Delft (TU Delft). The SAOS section focuses on the research and education on structural longevity and integrity of ship and offshore structures.

The HiTeAM project aims at the development and validation of a reliable and quantitative method for condition monitoring of highly-loaded low-speed bearing with the use of Acoustic Emission (AE).
Some applications of this method on bearings in the offshore industry are turret mooring systems on Floating Production Storage and Offloading (FPSO) ships [1] and [8], slew bearings in heavy lift cranes and in the pitch motion of wind turbine blades [2].

The HiTeAM project has been structured in 3 phases of which the 1st [9] and 2nd phase [10] have been completed.

- Phase 1 focused on the assessment of the feasibility of implementing an AE method for condition monitoring of highly-loaded low-speed roller bearings in an offshore environment.
- Phase 2 focused on the characterization and identification of waveform signatures for a selection of damage mechanisms in a laboratory setting.
- Phase 3 focuses on the in-field demonstration of the AE condition-based measurement system.

From the results of HiTeAM phase 1 and 2, observations were made about the AE activity in a linear segmented bearing with a limited stroke while testing multiple degradation mechanims e.g. rolling contact fatigue and corrosion failure. However, the speed was not representable for a real offshore environment.

1.2 Scope of research

The scope of research is defined as investigating the AE activity while performing an endurance test on a full-scale bearing geometry under representative load and speed conditions for an offshore environment. Furthermore, the influence of contaminated lubricant on the AE activity on a full-scale bearing geometry will be investigated as well as its possible masking effect on another degradation mechanism such as rolling contact fatigue.

1.3 Layout

This thesis is composed of 6 main chapters. At first Chapter 1 *Introduction*, argues the importance of predictive maintenance technologies for roller bearings, the HiTeAM JIP, the scope of this research and structure of the report. Secondly, in Chapter 2 *Literature review* the fundamentals and state of the art of roller bearing failures and condition monitoring methods, which forms the basis of this research is presented. After the literature review, the *Knowledge gap* is identified in Chapter 3 and according to this, *research questions* are formulated to provide guidance during the research. In Chapter 4, the *methodology* is presented in which all preparatory work for performing the experiments are described e.g. preparations of the test set up, the test specimen and test plan. Furthermore data processing methods for the obtained measurements are elaborated in this chapter. In Chapter 5, *Results and discussion* the processed results of the experiments are presented, observations are made and discussed. In Chapter 6, *Conclusions and recommendations* conclusions based on the results and recommendations for future research are provided.

Chapter 2

Literature review

The literature research is divided in two main parts, at first roller element bearings in general and their damage mechanisms are discussed. Before assessing the damage by acoustic emission, it is necessary to know, the working principles of rolling bearings and its damage mechanisms. Secondly, condition monitoring systems e.g. vibration analysis, lubrication analysis and acoustic emission, used to identify the damage state in bearings are discussed.

2.1 Roller element bearings and its failure

Roller bearings are widely used machine components which support and guide rotating or oscillating machine elements such as shafts and wheels which rotate relative to each other while ensuring minimal friction. Furthermore, it supports and transmits axial loads, radial loads and overturning moments through its rollers to other machine components [11]. A roller bearing consist of an *outer ring* which is often constraint in a housing, the *inner ring* in which often a rotating machine component is located particularly for sheave and turret bearings and *rolling elements* which allows load transfer and smooth rotations of both rings relative to each other. These components are the main components in roller bearings and schematically drawn in figure 2.1.

Roller bearings consist of two main and basic types of roller elements which are ball and roller elements as shown in figure 2.1. Looking more in detail to the contact between both elements, it can be noticed that a ball bearing makes a point contact between the raceways and a roller bearing a line contact. Since a point contact is much smaller, the contact pressure as a result of loading can be significantly high in comparison with rolling elements which have a larger contact area and lower contact pressure. Ball bearings have limited load-carrying capacity but lower rolling friction which allows higher rotational speeds due to the small contact area. Roller bearings can accommodate higher loads, but lower speeds due to the higher friction as a result of large contact area.

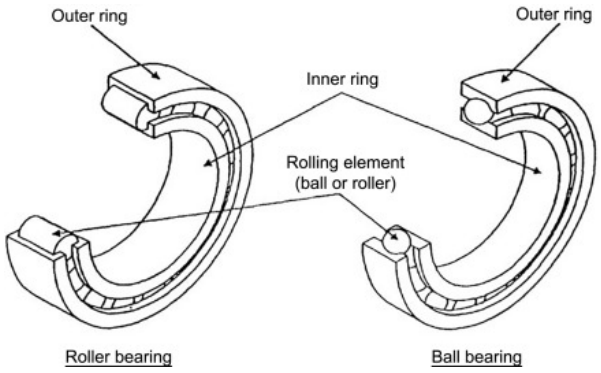

Figure 2.1: Overview of roller and ball bearing components [12]

Slew bearings

In the offshore industry, high radial loads up to several mega Newton, low rotational speeds and oscillating motions are common for bearings in general which makes slew bearings a suitable choice [11][13].

The rolling elements of slew bearings consist of ball or roller elements and can have different rows of rolling elements. According to American National Standard Institute [1], slewing bearings are classified in three types. *Single-row slewing bearings* consist of a single row of rolling elements in which the rolling element is at 4 points in contact with the structure of the slewing bearing. *Double-row slewing bearings* consist of 2 rows of rolling elements in which the top row carries the axial load and positive tilting moment and the bottom row the negative tilting moment. Since the top row rolling elements carries the largest loads, these elements are larger than the bottom row rolling elements. *The three-row slewing bearing* consist of three rows of independent rolling elements. The direction of the rolling elements are perpendicular to the load applied. The more rows a slewing bearing has, the higher the load carrying capacity of the slew bearing is. On the other hand, the more rows it has, the higher its frictional forces are. Sometimes, a gear is incorporated in one of the rings to allow rotation with a motor pinion connection. Usually, holes are drilled in the rings for the ease of fixation on a structure and to assembly a larger slewing bearing (D_{outer} > 2 meter) in segments. Slew bearing diameter size can be as little as 100 mm and up to a maximum of 30.000 mm.

Notable offshore application for slew bearings are, wind turbine pitch blades [14], heavy lift cranes, turntables for FPSO turrets and their main bearings. Other applications are in hoisting and conveying machines e.g. mobile cranes [15][16], material processing machines, harbor machines [17], metallurgic machines e.g. electric arc furnace and caster turrets [18], medical facilities e.g. electron accelerator gantry [19], radar and missile launchers [17][1].

Figure 2.2: Example of a slew bearing [13]

2.1.1 Failure of roller bearings

According to a bearing life and failure analysis of SKF [20] and van Beek [21], 90% of the bearings lifetime was longer than the equipment in which it was installed. 9.5% were replaced because of preventive reasons for example to prevent down-time of equipment or failure of other components as well. Only a small percentage of 0.5 % is replaced because of failure. The 0.5 % is very low in comparison with bearings which do not fail, but in comparison with the yearly worldwide production of bearings, 50 million bearings fail. In combination with the downtime of equipment, this can lead to extremely high costs for equipment owners.

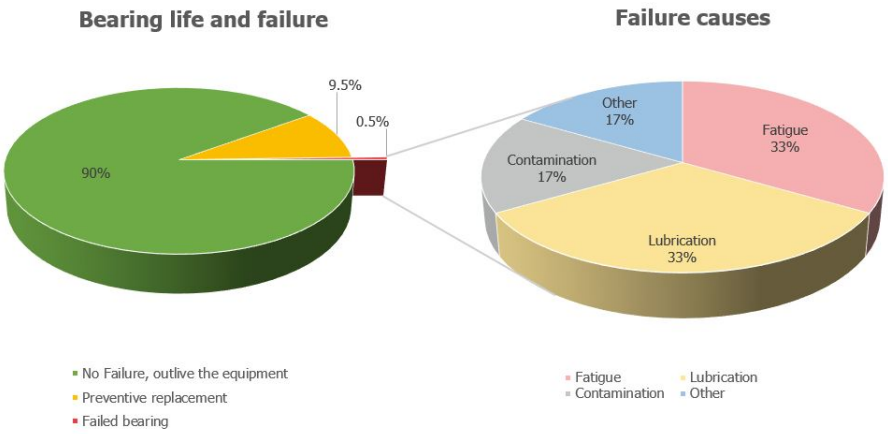

Figure 2.3: Bearing life and failure data according to [20]

The reasons of failure have also been investigated by SKF [20] and can be subdivided in 4 main reasons, as shown in figure 2.3. Most frequently, bearings fail because of rolling contact fatigue and lubrication problems, like wrong/insufficient lubricant and wrong lubrication interval. Less frequently bearings fail due to contamination, for example due to sealings problems through which water can leak and other reasons such as failure due to higher loads than expected.

By visually inspecting a failed bearing, more information about the damage mechanism which caused the failure can be acquired. A load pattern can be observed on a dismantled bearing which can be characteristic for a certain damage mechanism. By understanding the cause of failure, reoccurence of the failure can be prevented. Each failure leaves its own footprint on the bearing.

Damage classification

In the past, quite some research has been performed on bearing damage and failure in which it has been classified in different ways with different terminology according to a review by Halme et al. [22]. In 1995, the ISO defined a workgroup to define a clear and common classification and terminology of bearing damage and failure. In 2004, the ISO standard 15243 was published in which terms, characteristics and causes of damage and failure of bearings are covered [23]. Specifically, it covers all damage occurring in bearings during operation and its characteristic load patterns which relates to a certain failure cause and relies on evaluation of the characteristics obtained by non-destructive analysis.

The defined failure modes and its corresponding sub-modes are shown in figure 2.4 adapted from ISO 15243 [23]. From figure 2.3 and [20], failure by rolling contact fatigue and lubrication problems are often the cause of failure, therefore these failure causes will be discussed more in depth.

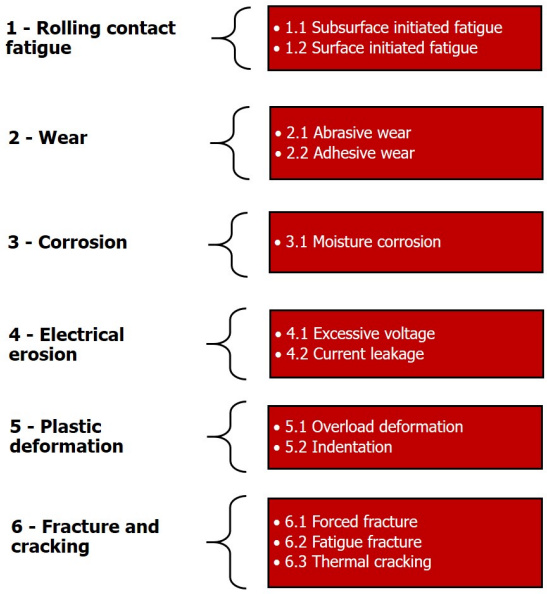

Figure 2.4: Bearing damage classification according to ISO 15243 [23]

Rolling contact fatigue

Fatigue is the accumulation of damage in the material caused by the cyclic stress levels developed between the contact of the raceways and rolling elements [24][25]. Fatigue failure is subdivided in two types, subsurface initiated fatigue which occurs due to material fatigue only and surface initiated fatigue which is caused by damage to the rolling contact surface asperities. The first study in the field of contact mechanics was performed by Hertz, and key parameters as contact pressure and geometry controlling rolling contact fatigue were recognized and proposed [26]. In 1969, Littmann [27] was one of the first to distinguish clearly between 6 different modes of rolling contact fatigue. Extensive amount of illustrations of the damage related to these 6 damage modes were provided. Littman was responsible for the first accepted classification of rolling contact fatigue for roller bearing [28]. However, the systematic study of rolling contact fatigue was performed by Way [29] in 1935 in gears and rail-wheel contacts. The mechanism of rolling contact fatigue has been widely studied in the past [28], currently the focus of research is more on rail contact fatigue which occurs nowadays due to high speed passenger trains and mixed and heavy loads [30].

Subsurface initiation fatigue

During operation of the bearing, the roller elements and raceways are repeatedly in the loaded zone. Cyclic contact stress levels occur. If for example the inner raceway is stationary, a particular contact will be constantly and repeatedly subjected to contact stress levels which consist of compressive and shear stresses. Load, temperature and number of stress cycles over a specific number of time are parameters which can cause material structural changes [31]. Due to the build-up of residual stresses, the material structure changes from randomly oriented grain structure to fracture planes [32]. Due to these planes, sub-surface microcracks occur near the zone of where maximum shear stresses occur typically at 0.1 - 0.5 mm beneath the surface [25]. These micro cracks will propagate and finally result in flaking, which is the peeling off of the material surface. As soon as the first flaking occurs, the bearing is damaged and needs to be repaired or replaced. The small particles can result in excessive wear of the entire bearing.

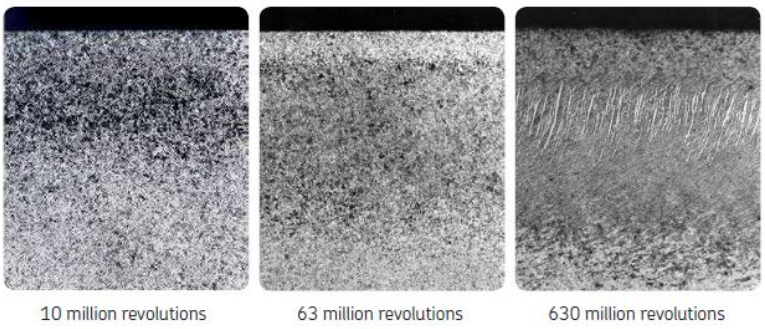

Figure 2.5: Example of subsurface fatigue development over number of cycles [20]

Surface initiated fatigue

Surface initiated fatigue originates from damage to the rolling contact surface asperities which is caused due to metal-to-metal contact between the roller and raceway. Lubrication prevents this metal-to-metal contact and allows for smooth rolling of rollers and rings. The metal-to-metal contact causes the asperities to shear over each other which results in micro-cracks in the asperities and eventually in microspalling. This leads to surface initiated fatigue. A glazed or dull and grey surface is characteristic for this failure mode. In a study by Rycerz et al. [33], it was found that crack initiation due to shearing asperities, occurred in a very early stage of the total bearing lifetime, which was attributed to high asperity stresses due to mixed lubrication regime. Total life to microspalling was dominated by the crack propagation rate. Crack growth was relatively slow and more steady-state than crack initiation. In their study, surface initiated fatigue is further elaborated.

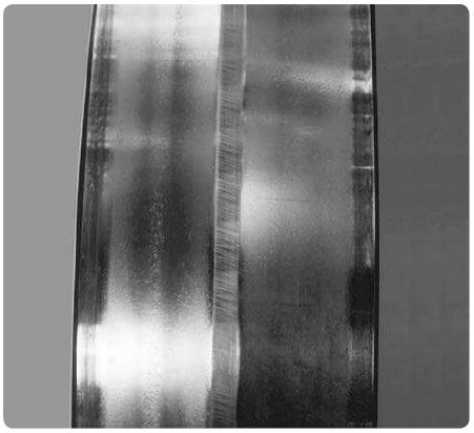

Figure 2.6: Example of surface initiated fatigue on raceway [20]

Wear

Wear is defined as degenerative process of surface material removal which results from relative sliding of the asperities of two contacting surfaces and is subdivided in abrasive and adhesive wear [34].

Abrasive wear

Excessive abrasive wear is the cause of inadequate lubrication or the ingress of solid contamination particles. The particles reduce the effectiveness of the lubricant which eventually can destroy the micro geometry of the bearing [35]. It can also wear down the surfaces of the raceways and rollers. The surfaces can look dull, grey or shiny (mirror-like) depending on the coarseness and nature of the abrasive particles. During service, the particle concentration will increase, since the material is worn away. It becomes an accelerated process which finally results in a failed bearing [36]. Abrasive wear theory was developed during an experiment of metals in sliding contact with hard abrasive papers by

Kruschov [37] in 1956.

Adhesive wear

Adhesive wear is the transfer of material from one surface to the other during relative sliding of two mating surfaces. It is accompanied by frictional heat which produces local stress concentrations which can result in cracking or spalling at contact areas. At sudden accelerations of rolling elements, sliding occurs which results in significant heat development which welds the metal to metal contact areas. This leads to higher friction. This phenomenon is sensitive for not heavily loaded high speed bearings. Adhesive wear was investigated in the early 1950s by Burwell and Stang [38] and Archard and Hirst [39][40].

Corrosion

Corrosion is an electrochemical process which gradually deteriorates certain metals by a chemical reaction by contact of the environment.

Moisture corrosion

Contact with moisture, e.g. water and aggressive liquid contaminants by the raceway and roller can result in oxidation of the contact surface. Next, the formation of corrosion pits occur which finally results in flaking of the surface. The moisture accumulates at the bottom of the contact between the roller and raceway and is mixed with the lubricant.

Frictional corrosion

Fretting corrosion occurs when relative micromovements between mating parts detaches small particles from the surfaces. When exposed to air, these particles are quickly oxidized and results in rust. Corroded areas act as fracture nodes leading to cracking of the ring. This failure is caused by a too loose fit between mating parts.

Brinelling

Brinelling is the phenomenon of indentation of the rolling elements on the inner cage. The material failure is caused by Hertz contact stress which exceed the maximum allowable stress. This can occur if a heavy load is resting on a stationary bearing for a long time. This results in Brinell marks.

False brinelling

At false brinelling the damage looks similar to brinelling but here the damage is caused by fretting wear. It also occurs between the rolling element and raceway contact areas as a result of micro movement caused by vibrations. It results in fretting corrosion between rolling elements and raceways.

Electrical erosion

Electrical erosion is the melting and breaking away of material between the contact surfaces caused by the passage of electric current.

Excessive voltage

If an electric current passes through the raceway and rolling element, sparkling occurs between the contact area since the area is very small, the current flow lines are condensed which results in local heating. A small series of craters will be observed at the contact area .

Current leakage

If the bearing is exposed to current, damage in the form of small shallow craters are initiated. These are positioned very closely to each other. In time, these craters will develop into flutes on the raceway.

Plastic deformation

Plastic deformation occurs when the yield strength of the material is exceeded. This can occur in two different ways,

- Macroscale - Yield strength is exceeded between the raceway and rolling element contact and causes deformation over a substantial portion of the contact area.
- Microscale - A solid particle is over-rolled between the roller and raceway where the yield strength is exceeded over only a small part of the contact area.

Overload

Overloading deformation can occur by a static overloading, shock loads or improper handling. It results in higher contact stress levels between the contact of the rollers and raceway which exceeds the yield strength. Severe deformation is often seen there.

Indentation from debris

Indentation are observed when foreign particles are over-rolled between the raceway and roller element. The indentation depends on the coarseness and nature of the particle.

Fracture and cracking

Cracks are initiated and propagated if the ultimate tensile strength of the material is exceeded. Fracture is a result of crack propagation till the point where there is a complete separation of a part of the component. In a study by Sague and Rumbarger [41] in 1977, core crushing failures of large diameter slew bearings were identified and illustrated. A new design criteria to prevent core crushing was proposed apart from the classical fatigue spalling (rolling contact fatigue), static capacity and surface failure which were commonly used design criteria. Core crushing occurs if the subsurface shear stresses exceeds the properties of the core material. In a study by Kim and Olver [42], it was presented that large roller bearings could fail due to radial cracks which may lead to fracture of the raceway or of the rolling elements. These radial cracks are a result of hoop tensile stress fatigue. The presence of hoop tension can originate from operational conditions or from residual stresses due to heat treatment especially for larger rollers.

2.2 Condition monitoring

The research of condition monitoring and fault diagnosis started in 1960s in the US [1]. Equipment can sometimes fail in an inconvenient time, for example during an operation at night in the weekend in the middle of a key process, which can result in an unplanned downtime, costly replacement of the broken part, safety and environmental concerns [43][44][1][2]. If a sudden failure occurs offshore, then often no spare parts are directly available and subsequently needs to be transported from onshore.
Basically, three main types of maintenance strategies exist and are used for equipments, Reactive maintenance, preventive maintenance and predictive maintenance [43][45][14].

Reactive maintenance

Reactive maintenance is a maintenance strategy which involves the replacement of components in equipment only after it has been broken, also known as the 'run till failure' approach. It is the simplest and cheapest way of maintaining equipment. However, there is a high risk of catastrophic failure of a component which can even result in damage in other related components. Usually, it results in high repair and replacement costs. Furthermore, it results in downtime, loss of key assets, lost production, risk of missing important contract deadline and reduced costumer satisfaction. Finally, there is a higher risk for health, safety and environment.

Preventive maintenance

Preventive maintenance focuses more on preventing failure of machine components in equipment in comparison with reactive maintenance. Components are timely replaced before damage develops and replacements are scheduled on specific times regardless the condition of the component. However, this strategy involves high costs since replaced parts can still have many years of operational life.

Predictive maintenance

Predictive maintenance is a more advanced and modern strategy than preventive and reactive maintenance. This strategy focuses on monitoring the damage state of components constantly during operation and can warn in advance the machine operator if a component is at risk. Maintenance is only performed if the monitoring system indicates if it is necessary and only on specific parts which indicates damage. Certain parameters as vibration, pressure and temperature can be used for the prediction. By this approach, unnecessary maintenance is prevented, number of unplanned downtime is reduced and risk of failure is eliminated. Furthermore, more insights can be developed on why components in equipment have failed and improve efficiency. However, it has high initial costs and requires training of workers, which can be the largest element of operational costs.

Before deciding to implement a condition monitoring system on a component, it is helpfull to perform a proper risk assessment to identify the criticality of the component and to determine its potential return on investment (ROI).

Vibration based monitoring and strain monitoring are known and standardised methods for condition monitoring of roller bearings. However, these are unable to provide a reliable damage diagnosis for low speed applications, [46] [47]. Other alternative condition monitoring methods, like lubrication analysis [48] [49], electrostatic monitoring of wear [50], temperature monitoring [51] and ultrasonic techniques [52] are proposed and explored in review papers. These methods are further elaborated in the reviews by de Azevedo et al. [2], Lu et al. [14], Rai and Upadhyay [53], El-Thalji and Jantunen [54] and Wang et al. [1] and they propose three main condition monitoring methods for roller element bearings; vibration-based monitoring, lubrication analysis and acoustic emission. Each of these systems are further elaborated and compared with each other in the following sections.

2.2.1 Vibration-based monitoring

Vibration-based monitoring is the most common condition monitoring method in industry for any kind of rotating equipment and demonstrated to be effective for detection of damage accumulation in medium- and high-speed roller bearings [55] [56].

The method provides real-time data and can react immediately to changes in the bearing. It can be used for permanent as well as intermittent monitoring. Vibration-based monitoring is not only applied on medium- and high-speed bearings, but also on the condition monitoring of steel bridges and buildings [57].

Working principle

Even in healthy condition, machine components have a certain vibration signature during operation. Most of the vibrations can be linked to a cyclic occurring motion of the machine components, for example the vibration of a shaft or gear tooth meshing. Its frequency can be theoretically determined and identified in the frequency spectrum.

For roller bearings itself, the classification of damage can be done with respect to the bearing elements itself. In general, damage can occur in the inner raceway, outer raceway, rollers or any combination of them. During operation of the bearing, the defects will generate vibration as the surfaces between rolling element and raceway interact which corresponds to specific frequencies. These damage frequencies are dependent on the geometry of the bearing, rotational speeds and in which part the damage is located. The frequencies can be calculated with the following equations [58].

$$F_{BPO} = \frac{1}{2} N_b * (1 - (\frac{N_b}{d_p}) cos(\alpha)) \tag{2.1}$$

$$F_{BPI} = \frac{1}{2} N_b * (1 + (\frac{N_b}{d_p}) cos(\alpha)) \tag{2.2}$$

$$F_{BS} = \frac{1}{2} * \frac{d_p}{d_b} * (1 - ((\frac{d_b}{d_p}) cos(\alpha))^2) \tag{2.3}$$

where F_{BPO} is the ball pass frequency of the outer raceway, F_{BPI} is the ball pass frequency of the inner raceway and F_{BS} the ball spin frequency. N_b is the number of rolling elements, D_p diameter of the roller, α is the contact angle of the radial load between the rollers and raceway. These equations are derived under the assumption that there is no sliding of the roller elements and that they roll over the raceway surfaces. However in practice, this is often not the case, which results in a slight deviation of the measured defect frequencies.

Other vibration sources

Besides the vibrations which are generated by defects, other sources of vibration also exist. The main other sources are variable compliance and geometrical imperfections. [59]. Frequencies of other vibration sources and background noise level can interact with each other which makes it difficult to detect damage.

- *Variable compliance* is a type of bearing vibration which occurs when a radial load is supported by a finite number of rollers which are constantly rotating over time and so not always in line of the load. The roller elements acts as elastic springs and elastically deflects during loading which eventually creates a relative and periodic motion between the inner and outer ring. The base frequency of this vibration is dependent on the rate of rolling elements passing through the load zone.

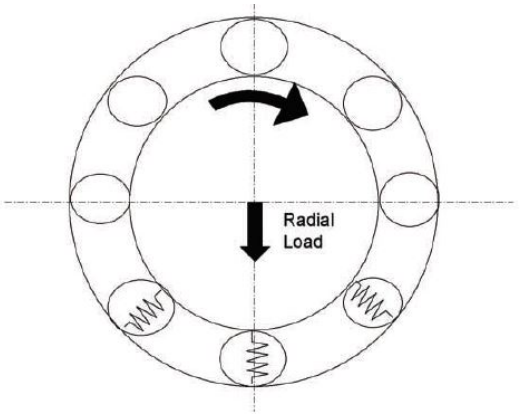

Figure 2.7: Variable compliance: The rollers acts as springs in the bearing and once the roller pass out the loaded area, a slight downward movement of the inner ring in the direction of the load is created. When a roller passes the loaded area gain, the inner ring moves upward. A relative motion is created. [59]

- *Geometrical imperfections*, like surface roughness is a significant source of vibrations if the lubricant film is too thin in comparison with the asperities of the rolling/sliding surfaces. These asperities can even get damaged which results in metal-to-metal contact which causes vibrations. The excited frequencies depends on the surface roughness, lubrication film and rotational speed of the bearing. The frequencies are above 60 times the rotational speed of the bearing. The more metal-to-metal contact occurs, the stronger the amplitudes of the vibrations. Damage can also occur during installation or assembly which initially are very small and difficult to detect but can significantly impact on vibrations and bearing lifetime.

Vibration measurement

For the measurement, vibration sensors are located as close as possible from the bearing, for example at the bearing housing. These sensors are piezo-electric sensors and measure the accelerations of the bearing. These accelerations are transformed to vibrations from which relevant parameters are extracted to make damage identification and development possible. The main three tools commonly used for damage identification and developments are described by Lacey [59] and explained in the following sections. These three ways are used together to obtain a proper and reliable indication of the damage state of roller bearings.

Overall vibration level
The first and simplest way to measure the vibration is by measuring the Root Mean Square (RMS) of the vibration. By measuring this property and monitoring the RMS with respect to time, the defects can be identified. An increase in the RMS-level can indicate a deterioration. A disadvantage of this method is that it is less sensitive the detection of damage initiation. Defects are detected in an advanced stadium, when damage has been further developed. Furthermore, the RMS can be influenced by other sources of vibration as mentioned before. Zhou et al, [60] describes the RMS-level and all other parameters in amplitude domain analysis and its application on condition monitoring and fault diagnosis of roller bearings.

Frequency spectrum
Frequency analysis can provide useful insights in damage detection. By transforming the vibrations from time domain to frequency domain, the number of vibration with respect to its frequency can be determined and plotted. If damage is initiated in the bearing, an increase in number of vibrations and amplitude will be noticed and its correspondence with theoretically determined damage frequencies eq. 2.1, 2.2, 2.3. An elaboration on frequency analysis of vibration measurement and condition monitoring of roller bearings is provided by Jayaswal et al. [61].

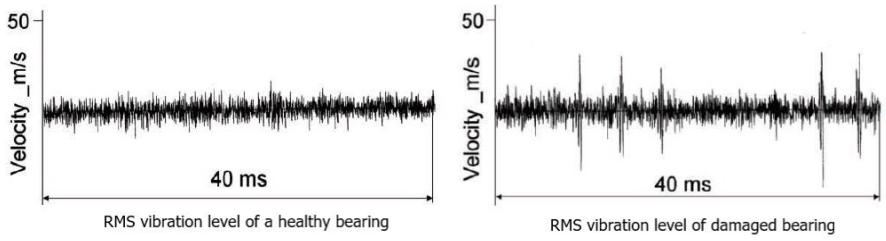

Figure 2.8: An example of the RMS vibration level with a comparison between a healthy and damage bearing. The peaks in the right graph provides an indication of possible defects. [59]

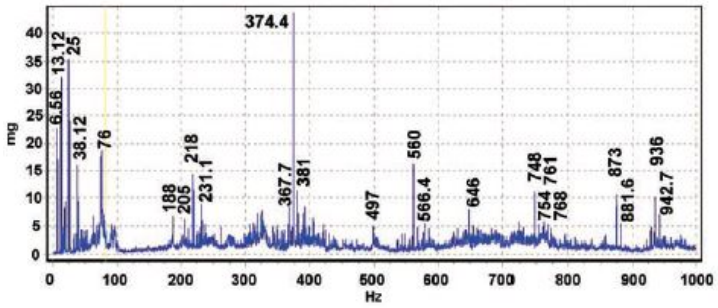

Figure 2.9: An example of a frequency spectrum derived from a vibrations measurement by [59]. Peaks at specific frequencies provides an indication of possible defects at a typical location

Envelope spectrum

When a rolling element passes and hits a defect on a ring, the natural frequency is excited. Generally, the natural frequencies of bearing rings are in the range of kilohertz. The vibration which occurs when a rolling element passes and hits a defect contains high frequency components. In a frequency spectrum, this will not be visible and not be possible to detect. By applying a high-pass frequency, the lower frequency components will be filtered out. After rectifying the signals and then applying a low pass filter, only the envelope of the signal whose frequency corresponds to the cyclic motion at which the roller elements hits the defect on the ring. With this technique, damage in roller bearing can be detected earlier. A more elaborate review on envelope spectrum and condition monitoring of bearing is provided by Borghesani et al. [62].

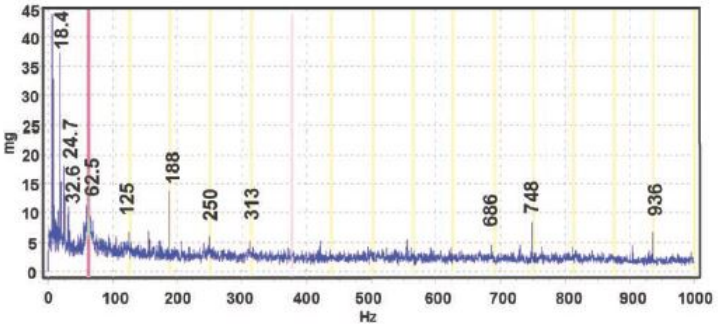

Figure 2.10: An example of a envelope spectrum derived from a vibrations measurement by [59]. A peak at 62.5 Hz and it multiples are highlighted in the graph. This frequency is typical for damage of the rolling element in the bearing.

State of the art

Jayaswal et al. [61], presented vibration analysis techniques on bearings and was able to detect earlier faults in bearings using vibration monitoring. Waters et al. [63], presented a real-time vibration-based

method to detect, localize and identify defects in an application on ocean turbine electric motor. Liu et al. [64], measured radial accelerations in ball bearings and was able to extract features as peak amplitude and peak RMS. Using algorithms, they were able to detect and identify defects. Furthermore, the discrete wavelet transformation method of vibration measurements were successfully applied by Sarvajith et al. [65], Nizwan et al. [66] and Sun et al. [67] to detect defects and faults in roller element bearings. Wavelet transforms have the feature to provide better frequency resolution at low frequencies and better time resolution at high frequencies. Machine learning algorithms like Artificial Neural Networks (ANN) and Support Vector Machine (SVM) are also successfully implemented to detect bearing damage and for classification between healthy and damaged bearing with vibration measurements by Ali et al. [68], Ma et al. [69], Unala et al. [70], Sarvajith et al. [65] and Ziani et al. [71]. For low-speed slew bearing, Caesarendra et al. applied the largest Lyapunov exponent algorithm for feature extraction from vibration analysis to detect defects [72].

2.2.2 Lubrication analysis

Lubrication analysis provides an indication of the bearing's tribological change from particle and liquid contaminants of the bearing's grease. Ferrographical and spectrometric analysis are common techniques used, as described by Bai et al. [73]. With ferrography, the ferromagnetic wear particles in a grease sample are separated by use of a high gradient and a strong magnetic field. The size, concentration, composition and morphology of these wear particles are analysed and can provide an indication of the location, type and degree of defects in the bearing. This analysis method is used in marine ships as described by Isaa et al. [74], machine components of aircrafts by Fan et al. [75] and diesel engines by Qin et al. [76]. Spectrometric analysis, is based on the principle of reflection and refraction. The grease sample is burned in a spark between 2 electrodes. The energy absorbed by the wear particles, emit light with specific wavelength which are characteristic for each element in the sample. The concentration of the wear particles can be determined with the light intensity. This analysis method is widely successfully used in heavy-duty machinery as described by Wei et al. [77] in shipping and Wang et al. [78] and in roller bearings in an aeroplane engine for condition monitoring.

If wear occurs in roller bearings during operation, the generated wear particles mixes with the grease and accumulates near the contact area of the roller and raceway. That makes it difficult to obtain representative grease samples. The wear particles distribution is non-uniform. To have more representative measurements, it is suggested to use a multi-spots sampling method [1][73].

State of the art

Lubrication analysis, demonstrated to be an effective and reliable method being used for condition monitoring of roller bearings according to Jiang et al. [79][80], Wang et al. [1], Bai et al. [73], and Kharche et al. [81]. Jiang et al. [79], presented a post failure analysis of a rolling bearing based on grease samples and showed that grease sampling is an effective condition monitoring method to avoid failure and extend bearings' lifetime. Moreover, Jiang et al. [80], applied an oil monitoring technique based on spectroscopy, ferrographic and other analysis techniques of gearbox oil samples and found that bearing defects in the gearbox can be identified by gear oil sampling. However it is unable to detect early stage damage development according to Bai et al. [73]. Furthermore, it cannot provide a direct indication of the damage state of the bearing. Heavy-loaded low-speed roller bearings are mostly installed offshore, so the grease needs to be transported to shore for further analysis in a laboratory, which is time consuming and can lead to unnecessary down-time.

2.2.3 Acoustic Emission

Fundamentals

Acoustic emission is a passive non-destructive testing technique and defined as a phenomenon whereby transient elastic waves are generated by a rapid release of strain energy from a localized source within a system according to Weng et al. [82]. If a material is loaded within the elastic regime, strain energy is stored in the material. When the applied load goes beyond the material's elastic limit, the stored

strain energy is released and crack initiation or propagation in the material occurs. The remaining strain energy is used to generate heat and sound. This sound is referred as acoustic emission. The emission of waves consists of high-frequency components in the order of up to 1 MHz [83]. The waves are generated inside the material and propagated through the material. These can be measured by a piezoelectric ceramic type of sensor on the surface of a material [84], [85] and [86]. A more elaborate description of acoustic emission is provided by The Japanese Society for Non-Destructive Inspection [87].

Measurement system

An AE measurement system consists of a piezoelectric sensor (AE sensor) which measures pressure differences which results in vibrations of the crystal and transforms it into an electrical vibration, a preamplifier which amplifies and transmits the AE sensor output to the AE signal processor which finally measures and records the electric signals, may perform feature extraction and displaying of the measurements. These hardwares are shown in sequence in figure 2.11 [88].

Figure 2.11: Overview of AE measurement system [88], AE sensor (left), AE pre-amplifier (center), AE signal processor (right)

AE waves

An AE wave is defined as an elastic stress wave which is generated at an AE source. Examples of AE sources are crack formation, plastic deformation and sliding/slipping [87]. AE waves consist of two types of waves, burst and continuous type. The emission of burst type of AE waves are related to crack initiation or propagation in the material [89]. Continuous type waves are often related to noise or plastic deformation in the material. An example of a burst type of wave is shown in 2.12.

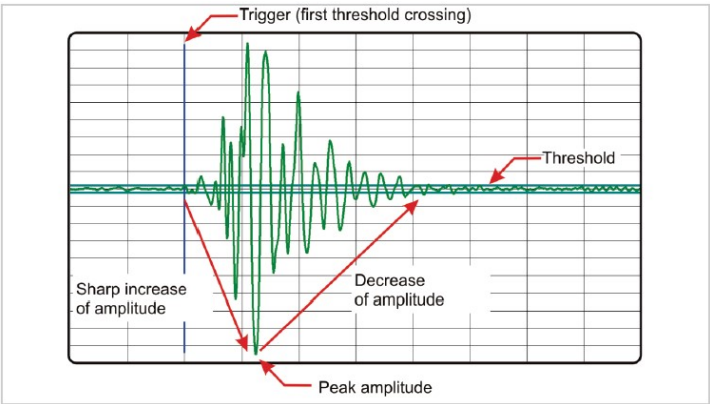

Figure 2.12: An example of a burst type of wave

In a research by Scheeren et al. [90], a feasibility study was performed on the implementation of a condition monitoring system on heavy loaded low-speed sheave bearings with the use of AE. The focus was on the investigation of wave transmission through the inner parts of the bearings and its interfaces. AE signals, released due to crack development in the inner parts of the bearing, propagate through all solid parts, grease and interfaces, see figure 2.13. During propagation, the waves get reflected,

scattered and diffracted. If the waves still consist of sufficient energy, then these can be detected from the outer surfaces. The transfer path is shown in figure 2.13, where S_I is the AE source at the inner ring, $D_{O,I}$ the coupling between raceway and sensor, W_1, W_2 and W_3 the wave propagation functions through the inner raceway, roller and outer raceway respectively and T_{12},T_{23} the transmission functions of the interface between the roller and raceway inner ring and interface between roller and raceway outer ring.

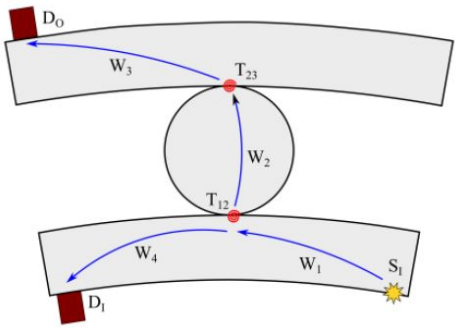

Figure 2.13: Wave transmission path [91]

From the results from [90], it has been concluded that the transmission of AE signals through the rollers and its interfaces is potentially of sufficiently strength to be detected and can be distinguished from the background noise. There is an attenuation of the amplitude from one raceway to the other of around 20-30 dB independent of the sensor types used in their experiment.

AE parameters for data processing

When a crack is initiating or propagating, burst types of signals are emitted [89]. A burst wave is characterized by a sharp increase of amplitude within a short amount of time and a rapid decay of the signal. Once a burst signal crosses a certain pre-defined amplitude threshold, a hit is identified. The hit is an important parameter for the identification of damage with AE. Hits are an indication of AE activity. For bearings with rotating speeds lower than 10 RPM, counts and peak amplitude hits are the most commonly used parameters to extract information [8]. The main AE features used for data processing of roller bearing condition monitoring were elaborated in a review by Caesarendra et al. [8] and described below.

Hit
A hit is defined as the first and last crossing of the signal's amplitude of the threshold, shown in yellow in figure 2.14.

Peak amplitude
The amplitude of all waves is measured in microvolts (μV) and translated to decibel (dB). When a signal, crosses a certain pre-defined amplitude threshold, it is being recorded. The maximum amplitude of that signal is stored and further used for analysis.

Counts
The number of waves passing the treshold is being stored and counted. These counts occur within a hit and are used to provide more information on the damage development.

Duration
The duration is defined as the time interval between the first and last count of a hit.

Energy
The energy of the wave is defined as the numerical integral of the squared voltage integrated over the duration of the wave.

Rise time

The rise time of a wave is defined as the time-interval between the first crossing of the threshold and time of the peak amplitude.

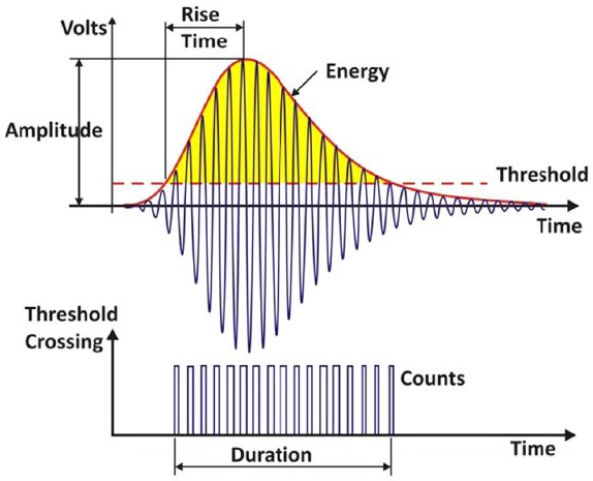

Figure 2.14: Overview of AE parameters [8]

Development of research in the field of AE

Balderston [92], demonstrated at first in 1969 the potential of detecting defects with AE prior to failure in a laboratory evaluation. Subsequently in 1979, Rogers [93] demonstrated the potential of AE in field on a slewing bearing of an offshore crane. In the following years, more studies investigated the applicability of acoustic emission for condition monitoring of bearings in comparison with vibration based monitoring, [94], [95], [96]. In particular for high-noise and low-speed applications, the studies proposes acoustic emission as an alternative to vibration monitoring. Furthermore, the potential use of AE as an early warning system was proposed by Cornal et al. based on the probable detection of early-stage subsurface cracking in an endurance test of a bearing [97].

Comparison of AE and vibration monitoring

Vibrations originating from the accelerations of roller bearings are not being measured and are not part of acoustic emission. Furthermore, ultrasonic testing for the detection of subsurface cracks is different from acoustic emission testing. With ultrasonic testing, a transducer emits a waveform which is again measured by a sensor on a different location. If the reflection of the wave is measured, then a crack can be detected.

Vibration-based condition monitoring has been studied better and more frequently used in comparison with acoustic emission [96][94]. Vibration analysis is simpler and data acquisition and analysis tools are well developed. However, in some case acoustic emission-based condition monitoring has more advantages over vibration-based condition monitoring.

- AE has been demonstrated to be able to detect early defects and can provide an indication of the crack size [98], [97].
- AE demonstrated to be effective and more reliable than vibration analysis in the detection of an artificial defect in the outer ring with AE peak amplitudes than RMS of the vibration signal [96].
- AE demonstrated to be more sensitive in the tracking of surface and subsurface micro-damage development in comparison with vibration-based method [94][2].

- AE is less sensitive to noise originating from accelerations of other machine components, since AE signals have a minimum frequency of around 50 kHz and maximum of 1 MHz [96]. Furthermore, its frequency band is broader.

However, AE requires a reference (baseline) measurement for roller element bearings in order to distinguish the AE activity of a healthy and damaged bearing [8][9]. Furthermore, AE for roller bearing condition monitoring is sensitive to operational conditions and highly dependent on sensor location and type [99]. He et al. [100] have shown that the bearing operating speed greatly influences the AE parameters for rotational speeds between 200 - 500 RPM. All speeds lower than 600 RPM are generally considered as low speed [101]. For much lower speeds, Miettinen and Pataniity have proved that the detectability of AE signals decreases with decreasing speeds in the range of 0.5-5 RPM [102]. However, through classification approaches by autoregressive coefficients, it was possible for Mba et al. [103] to successfully separate noise from damage induced signals of natural origin and Jamaludin et al. [104] for artificial damage origin.

State of the art

So far, monitoring of damage with acoustic emission has been reported successfully in different applications e.g. for steel bridges [105] [106], [107], concrete structures [108], [109],[86] [110] and composite laminates [85], [111], [84] [112].

The state of the art of AE focuses on improving robustness for damage detection [99], [113], [114], and the estimation of damage severity [115], [116], [117], [89], and localization [118][86]. Moreover, signal-based clustering shows promising results in the differentiation between different degradation mechanisms [86]. Clustering is a process in which a set of waveforms are grouped into categories according to for example waveform similarity by cross-corelation. van Steen et al. [86], proposed a signal-based hierarchical clustering algorithm for AE waveforms. The shape of an observed waveform at a certain location is unique for emission from a typical degradation mechanism. Similarity of waveforms originate from similar degradation sources. Localisation of damage can be accurately localised in 1D and 3D, as proved by van Steen et al., in concrete structures. For 1D, 2 sensors are needed and for 3D, 6 sensors are needed. Localisation of damage is dependent on the time of arrival of AE signals, source time and wave velocity. For 3D localisation, Geiger's method, a nonlinear iteration process is used.

Machine learning techniques like discrete hidden Markov models [119], neural networks [120], deep learning [121] shows promising first results for AE source localization. Furthermore, these studies show potential for defect location identification through classification of wavelet transformed signals, however, these successes are tempered by their inclusion of only artificial defect. Defect size are being determined using parameters such as the duration of or time between AE bursts signals.

According to a review of Caeserandra et al. [8] of AE condition monitoring for low speed slew bearings, most research articles focuses on rotational speeds around and higher than 600 RPM and artificially damaged bearings. For very low speed bearings (speed < 10 RPM) with naturally induced damage as well as artificially made damage, very limited research has been performed. An overview of the number of research articles found in this field is shown in figure 2.15.

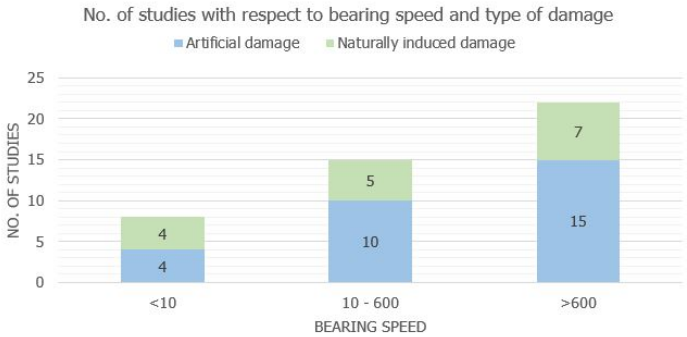

Figure 2.15: Number of studies performed with respect to the bearing speed and type of damage [8]

Contaminated grease and its influence on AE signals
From chapter 2.1: Roller element bearings and its failure, it becomes evident that contamination particles in grease like steel can result into faster development of damage inside bearings. Furthermore, from chapter 2.2.2: Lubrication analysis, a rough indication of damage inside bearings can be obtained with help of grease sampling and analysing it. Therefore, contaminated grease is highly related to the lifetime of bearings.

In a study by Miettinen and Andersson [122], the influence of contaminants in the grease of roller bearings on AE signals were investigated. For the research, experimental work was performed with a 62 mm outer diameter ball bearing on a rotational speed of 400 RPM. A load of 1950 N was applied, which corresponds to a mean contact pressure of around 2800 MPa. Spherical HSS steel grade M2 contaminant particles of 20 µm diameter with concentrations of 0.75 g, 7.5g and 75g per kg grease were used for the bearing in the experiment. An AE resonance type sensor with 150 kHz centre frequency was used for the measurement.

From the measurements, it was observed that the least contaminated lubricant (0.75g/kg grease) induced a much higher (250x more) amount of hits/pulses than a clean lubricant. The total number of hits during the test of the different concentrations of HSS steel M2 particles is shown in figure 2.16. From the results it was concluded that there is a clear increase in hits with contaminated lubricant. A higher concentration of contaminants results in a higher amount of hits. However, there is not a linear relation with the concentration and number of hits. With increasing concentration, there is a certain saturation of the number of hits. In a study by Jiang et al.[123], a similar trend of number of hits with respect to the concentration of steel particles were observed.

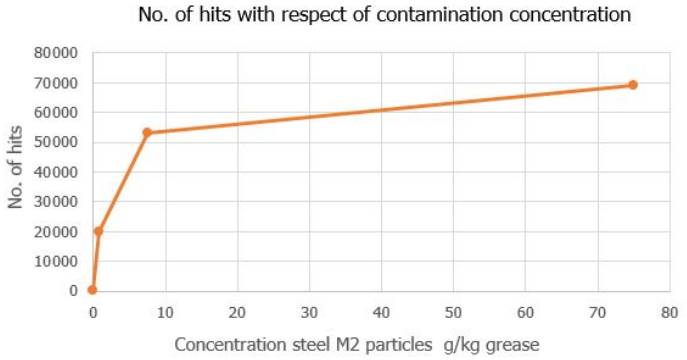

Figure 2.16: Number of hits with respect to the concentration level of steel M2 particles. [122]

Furthermore, from the results it was observed that hard steel particles results in higher AE activity. Due to high pressures and deformation in the contact zone by hard particles, high AE peak amplitudes are induced. From AE time signal analysis, it can be observed that particles with higher hardness, have

higher peak amplitudes. In the experiment, a comparison between relative soft Iron particles and hard steel M2 particles were performed to obtain this observation.

Chapter 3

Knowledge gap and research questions

3.1 Knowledge gap

According to the problem statement and literature study, a knowledge gap has been identified and research questions have been formulated. From the literature study, it becomes evident that failure of roller bearing can result in severe consequences for machine owners. Condition monitoring of roller bearings can support the machine operator in the detection of faults in an earlier stage. However, for heavy loaded low-speed roller bearings, condition monitoring techniques are not well enough studied, although AE shows promising results.

3.1.1 Damage assessment of roller bearings with AE

Three main condition monitoring methods for roller bearings were proposed in the literature review namely, vibration based monitoring, lubrication analysis and acoustic emission. For the condition monitoring of low speed bearings, vibration based monitoring is unable to detect early stage damage development. Furthermore it is unable to detect subsurface micro damage. AE monitoring is able to detect these and shows promising results for the condition monitoring of highly-loaded low-speed bearings.

In a review by Caesarendra et al. [8] it was shown that very few studies have been performed on very low speed bearings (<10 RPM). Furthermore in these limited studies, the size and applied load of the bearings were relatively small in comparison with the commonly applied bearings in the offshore industry. Turret and slew bearings in offshore application have an average linear speed of 0.15 m/s and maximum of 1 m/s according to a study of Naciri and Chitrapu [124]. Besides that, more research can be performed with naturally developed damage in bearings. This can be performed by conducting a fatigue test till failure of a bearing while measuring the AE activity for example. Naturally developed damage, consist of representative defects which will correspond to more representative emission of AE signals. With artificially made damage there is no clear indication that the damage is sufficiently representative and whether these AE signals are representative for naturally developed damage. This means that more research is needed on AE signal emission and damage development on very low speeds.

Furthermore, there is a potential for the use of AE monitoring of highly-loaded low-speed roller bearings. From the study of Scheeren et al. [91], it was observed that the AE events occurring somewhere in the bearing can be detected and recorded by the measurement system. This means that it is feasible to measure the AE signals while having a sensor attached to the inner or outer ring.

3.1.2 Assessment of contamination in roller bearings with AE

Contaminated lubricant plays an important role on the lifetime of bearings. From the study of Miettinen and Andersson [122] a new possibility of research can be identified. Since contaminated grease results in higher AE activity, then it could be possible to provide an indication of the concentration contamination particles in grease. AE measurement can provide real-time data, and could be of additional value in bearings used offshore if it is possible to retrieve information about the development of contamination in grease. Traditional grease sampling and analysing require quite some time, especially if the bearing is offshore. Furthermore it would also be interesting to know between which frequency band, signals for contaminated grease are originated. On the other side, the study performed by Miettinen and Andersson [122], used a small bearing in comparison with the general size of offshore bearings and performed the tests in a high speed regime.

3.2 Research questions

The following research questions are formulated with subsequent subquestions according to the knowledge gap identified in 3.1.1: Damage assessment of roller bearings with AE.

How can Acoustic Emission be applied to assess the damage of highly-loaded slow-speed roller bearings?

- *How is the AE activity of an undamaged bearing under representative operational conditions?*
- *How is the AE activity of a worn bearing under representative operational conditions?*

According to the knowledge gap identified in 3.1.2: Assessment of contamination in roller bearing with AE, the following research questions are posed:

What is the influence of contaminated lubricant on the emission of AE signals in highly-loaded low-speed roller bearings?

- *What is the masking effect of AE signals emitted by contaminated grease and other damage degradation mechanisms?*

Chapter 4

Methodology

Experimental research has been carried out to investigate in how acoustic emission monitoring can be applied on highly-loaded low-speed roller bearings to assess the damage. The results of this experiment will help to answer the research question posed in chapter 3.2: Research questions.

To answer the first research question and its subquestions, a full-scale duration test will be performed on a roller bearing which is already slightly damaged under operational conditions and by means of developing damage inside the bearing the AE activity will continuously be monitored. The measurements will provide more insights in the relation between AE signals and damage development, how it relates to visual damage and verification of the results with obtained results from the HiTeAM project.

To answer the second research question, the aim to investigate the influence of contaminated lubricant on AE will be performed by means of an experiment carried out on a second roller bearing with lubrication contaminated with iron particles. The results will be compared with the results obtained from the baseline and fatigue test.

In this chapter, the experimental work will be discussed. At first the roller bearing which will be the test specimen and its lifetime calculations are discussed. Secondly, the preparation of the existing test set up and test plan are elaborated. Thirdly, the measurement system and data processing techniques are described.

4.1 Test specimen

The roller bearing used for the experiments originates from the Pioneering Spirit of Allseas and was used to support the beams of the Topside Lifting System (TLS). The Pioneering Spirit is the world's largest construction vessel designed for the removal and installation of large gas and oil platforms and for pipe laying [125]. The installation and removal is performed with the Topside Lift System which has a lift capacity of 48,000 tonnes kg. The TLS is mounted on the fore of the ship, at its characteristic bows where it can sail in between the platform, see figure 4.2. On the aft main deck, the Jacket Lift System will be installed which will be able to install and remove jacket structures.

Figure 4.1: Allseas' Pioneering Spirit

Figure 4.2: Lifted platform by TLS

Topside Lifting System

The TLS consist of 16 beams which can translate towards the bow and along both starboard and port side of the ship. This allows for exact positioning of the beams before the lifting operation. During an operation, the beams work in pairs in order to allow for vessel motion compensation in 6 directions. These beams form together a so called fork lift unit. With hydraulic cylinders installed inside the beams, the platform is lifted.

Each beam is supported on two supports: one support on the outboard side of the bow and one support on the inboard side of the bow. Both the outboard support (OBS) and the inboard support (IBS) allow for movement in longitudinal and transverse direction along the bow. In figure 4.3 the outboard support is shown and figure 4.4 shows the wheel inside the OBS.

Figure 4.3: Outboard support TLS, yellow circle shows the location of the bearings

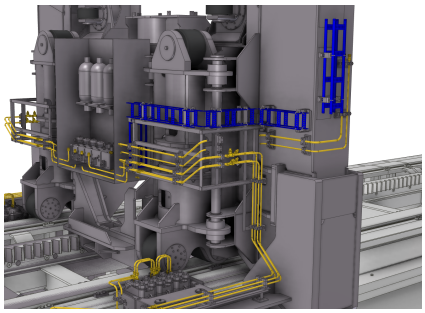

Figure 4.4: Zoomed in picture of the TLS OBS bearings

Prior lifetime consumption

These wheels are actually a roller bearing where the outer ring is used as a wheel. Several of these failed due to overloading and therefore all these wheels have been replaced by larger wheels. As the old wheels had no purpose anymore, they could be used for testing purposes. The wheels that were made available for testing consumed approximately 40% of its basic rating lifetime L_{10} [126]. Therefore less time is needed to fully damage the bearing i.e. to reach 100% of its L_{10} in a fatigue test compared to a new bearing. The damage was developed during operations however the wheels were loaded outside its design limits resulting in excessive plastic deformation and premature failure. In normal circumstances if the wheel was used within its design limits, another type of failure would occur after a longer time. Therefore the failure of the wheels are not fully comparable with failure of a wheel used within its design limits.

To visually inspect the damage, the available bearings were opened up. From the outer ring, it can be observed that traces of wear are visible over the entire raceway. Grooves at the raceway are visible at the locations of the sides of the rollers. The raceway of the outer ring is shown in figure 4.7. The pictures of the inner ring are shown in figure 4.5 and 4.6. Only on a specific side of the inner ring, traces of wear were observed, see figure 4.5. The reason for wear only on this specific side is that the inner ring was stationary and most often loaded in one direction. The outer ring was continuously rotating. The inner ring rotated 180 degrees with respect to figure 4.5, no clear indication of wear was visible, see figure 4.6. During opening up of the bearing, sufficient lubrication of all components was observed.

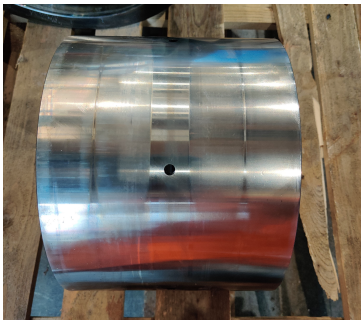

Figure 4.5: Slightly worn side on the inner ring

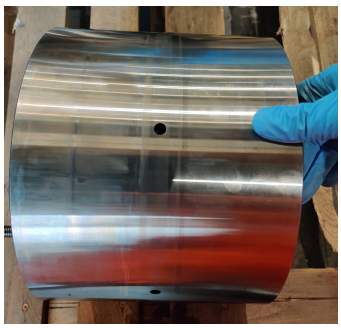

Figure 4.6: 180 degrees rotated inner ring, no wear visible

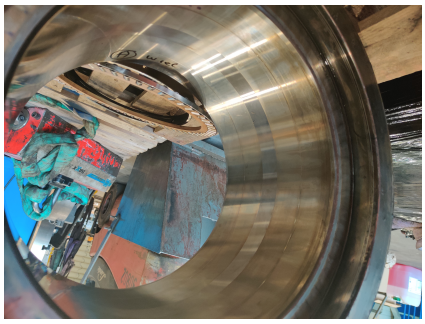

Figure 4.7: Raceway of outer ring, 1st inspection. Wear visible on raceway

Dimensions

The bearing consist of 6 main parts: the outer ring, the inner ring, the rollers, the flange, the spacer and axial rolling elements including its cage, all shown in figure 4.10. A 3D model of the bearing is shown in figure 4.8 and a 3D cross-section is shown in figure 4.9. It has an outer diameter D_o of 400 mm, inner diameter D_i of 200 mm and consist of 4 raceways with each having 42 rollers. The main dimensions are provided in table 4.1. The bearing's dimensions are suitable to be installed in the test set up described in section 4.2: preparation of the test set up.

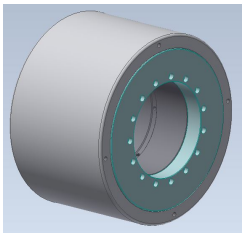

Figure 4.8: Test specimen: TLS OBS wheel

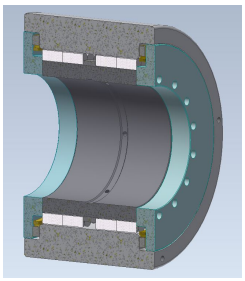

Figure 4.9: 3D cross-section of test specimen

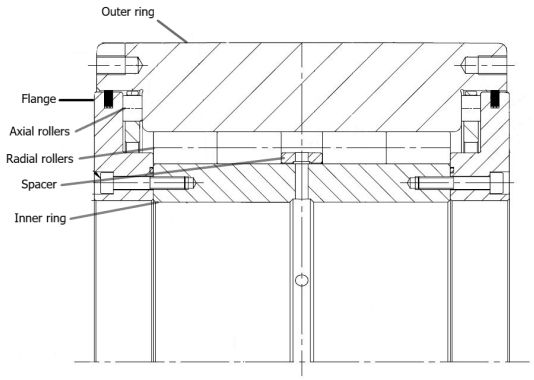

Figure 4.10: 2D cross-section of test specimen

Parameter	Symbol	Dimension	Unit
Outer diameter	D_o	400	[mm]
Inner diameter	D_i	200	[mm]
Width bearing	$B_{bearing}$	258	[mm]
Roller diameter	D_{rwe}	20	[mm]
Roller length	L_{we}	40	[mm]
Thickness outer ring	t_o	50	[mm]
Thickness inner ring	t_i	30	[mm]
No. of raceways	i	4	[-]
No. of rollers per raceway	Z	42	[-]
Weight	$M_{bearing}$	178	[kg]

Table 4.1: Parameters of TLS wheel [127]

Material properties

Both inner and outer ring are made of 42CrMo4, an alloy steel for quenching and tempering and have a yield strength $R_{p0.2,rings}$ of 635 MPa and tensile strength of 825 MPa [128]. The Rockwell scale hardness HRC is 58. Both rings have been quenched and tempered. However, the material properties are not constant over the thickness of both rings, since they are hardened. The rollers are made of 100Cr6 steel alloy.

4.2 Preparation of the test set up

To primarily load and rotate the test specimen, an existing in-house machine designed by Allseas is used to perform the experiments. The machine was originally used to improve polyurethane (PU) coatings on rollers. These rollers are installed on the stinger of Allseas pipelay vessels to support and roll pipes towards the seabed. A drawing of the original set up is shown in figure 4.11.

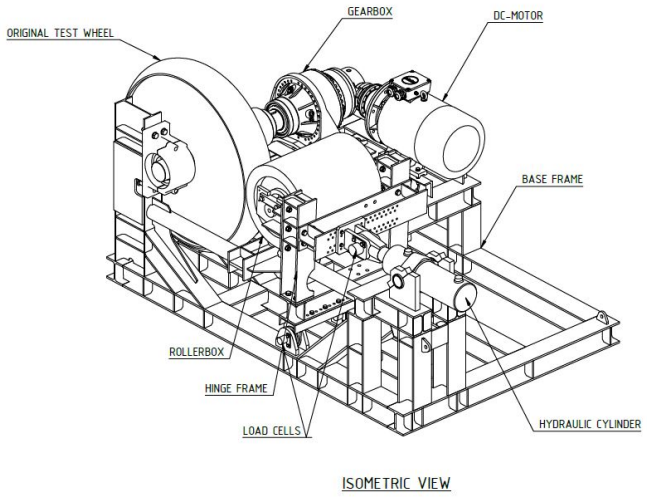

Figure 4.11: 2D drawing of original test set up for rollerbox coating testing

The working principle of the machine is as follows. A test specimen can be installed at the location of the roller. Behind the test specimen, a hydraulic cylinder is pressing the test specimen to a large test wheel with an outer diameter of 1360 mm that models an infinite length of pipe. The load is transferred from the hinge frame where the cylinder is pushing at. Via the supports of the shaft and the shaft itself, the bearing is pressed against the test wheel. The test wheel is connected to an electric motor which drives the test wheel via a gearbox. The machine can be controlled from the control unit (not shown in figure 4.12) in a manual and automatic mode.

The hydraulic cylinder can exert a maximum compressive load of 490 kN. The machine is equipped with several measuring devices, these include a 50t load cell to measure the load applied to the bearing wheel, a pressure sensor to measure the actual pressure applied in the cylinder, and a position sensor to measure the extension of the hydraulic cylinder. All measuring data are stored using a data logger.

The electric motor has a power output of 4 kW and the output speed of the gearbox ranges from an advised minimum of 7.2 RPM and maximum 18 RPM to the test wheel. In case, a lower speed is necessary, the speed of the electric motor can be adjusted as long as a forced cooling is applied on the motor.
The pressure in the cylinder and speed of the electric motor are entered via the control panel on the cabinet or PC. The desired force needs to be converted in the applied pressure of the cylinder. From the control software on the PC, the speed, pressure and pushing force can be read out. Via the PC, the run time and a time for a break of the machine can be set up, which allows automatic running of the machine. The control panel of the cabinet allows only for manual operation. Due to the size difference between the bearing and the test wheel, the bearing rotates at 3.4 times the speed of the larger test pipe. As such, the TLS wheel can reach a rotational speed of 60 rpm, representing a linear speed of 1.22 m/s.

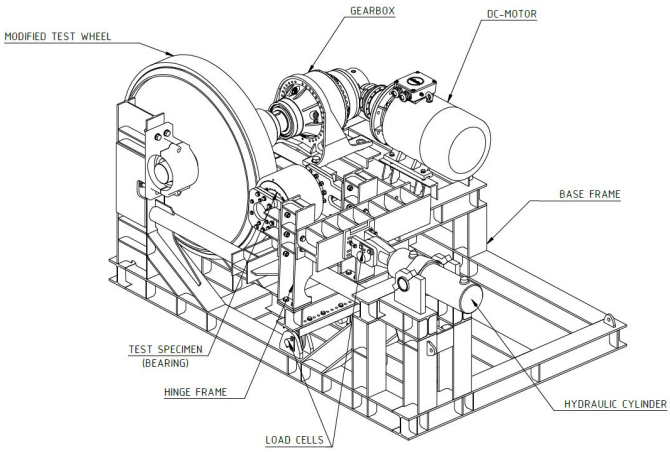

Figure 4.12: Drawing of test set up for roller bearing

Figure 4.13: Front view test set up

4.2.1 Modification of test set up

The original test set-up was not suitable to perform the experiments on, modification of existing parts and designing new parts was required. The modification is divided in 2 parts, modification of the test wheel and design of the bearing support.

Modification of test wheel

The original test wheel, made of S355 steel and shown in figure 4.11, is not strong enough to resist the load of the bearing. Since the wheel has a curvature at the exterior, a point load will be acting between the wheel and bearing. Because the contact stress is far too high at a maximum load of 50t kg ($\pm$ 3000 MPa) on the test wheel and the bending stress inside the test wheel too ($\pm$ 300 MPa), the wheel would have failed during the experiment. To reduce the contact stress, the contact zone of the test wheel is flattened, additionally a hardened ring (Quard 400) is fitted around the wheel to improve the yield limit. Quard 400 is a high strength abrasion resistant steel sort with applications in mining and dredging industry. It has a hardness of 400 HBW and yield strength $R_{p,0.2}$ of 1160 MPa [129].

To determine if the contact stress in the modified wheel is allowable, a FEM analysis has been performed and Hertz contact theory is used for validation. In figures B.1 and B.2 the FEM model and the results of the contact stress are shown. The bearing and test wheel are modelled as a contact connection and a load of 490 kN is applied downwards on the bearing. The contact stress at the modified test wheel is around 1100 MPa from the results of the FEM model. More information about the FEM model can be found in Appendix B.1: Contact stress in modified test wheel.

The contact stresses are determined with the Hertz contact theory [26] for cylinders with flat surfaces as follows. The maximum contact stress P_{max} can be determined by,

$$P_{max} = \frac{4}{\pi} P_m, \tag{4.1}$$

where P_m is the mean contact stress. Subsequently, the mean contact stress can be determined by

$$P_m = \frac{F}{2bl} \tag{4.2}$$

where F is the applied load, b is the effective half contact width and l the effective contact length.

The effective half contact width b is,

$$b = 2 * (\frac{2}{\pi})^{0.5} (\frac{F}{l})^{0.5} (\frac{R'}{E})^{0.5} \tag{4.3}$$

where, R' is the effective radius and E the Young's Modulus.
Eventually, the maximum shear stress can be determined by,

$$\tau_{max} = 0.387 * P_m \tag{4.4}$$

The maximum allowable contact and shear stresses in the material can be determined by,

$$P_{m,c} = 1.29 * R_{p,0.2} \tag{4.5}$$

$$\tau_{max,c} = 0.5 * R_{p,0.2} \tag{4.6}$$

The effective contact length l is 100 mm determined by the FEM model and applied load F is 490 kN. The maximum contact stress P_{max} is 973 MPa and maximum shear stress τ_{max} is 295 MPa. Comparing the results from the FEM and analytical solution, the differences of the maximum contact pressures are relatively small. Furthermore, the highest maximum contact pressure is still below the maximum allowable contact stress of the hardened ring. From the results, it becomes evident that S355 steel is not strong enough. Therefore, Quard 400 is used since it has a maximum allowable contact stress of 1496 MPa and maximum allowable shear stress of 580 MPa [129].

Bearing support in test set up

To hold the bearing in the test set up, a support frame had to be designed. A hollow shaft was designed with the same outer diameter and tolerance as the shaft used in the TLS-wheel on board. The shaft was made hollow for easy installation and for the ease of injecting the grease by hand. Six lubrication ports were made in order to inject the grease equally over the circumference of the bearing. To install the bearing and shaft in the set up, supporting frames were designed which are connected to the hinge frame and connects the bearing shaft assembly. A disk on each side of the frame is designed to resist axial loading and to keep the shaft and bearing at its place. In between the bearing supporting frames, spacers are designed which prevents the bearing not to translate along the shaft. By tightening the bolts between the disc and shaft, all parts in between the bearing supporting frames are under compression. The spacers presses against the inner ring of the bearing which prevents the shaft and the bearing, except the outer ring and rollers, to rotate. The inner ring of the bearing will not rotate and constantly cyclic loaded in the test set up. This will result in more development of damage inside the inner ring than other parts of the bearing. In figure 4.14, a drawings of the bearing support is shown. In the left-top, a front view of the bearing support is shown with references to the cross-section A-A and detailed view 1. At the right-top, a isometric view of the bearing support is shown with references to the different components. At the left-bottom side, a detailed view is provided for the section shown in the base view. In this view, the bolted connection between the disk and shaft can be noticed. In the right-bottom side, the cross section at the location shown in the base view is shown.

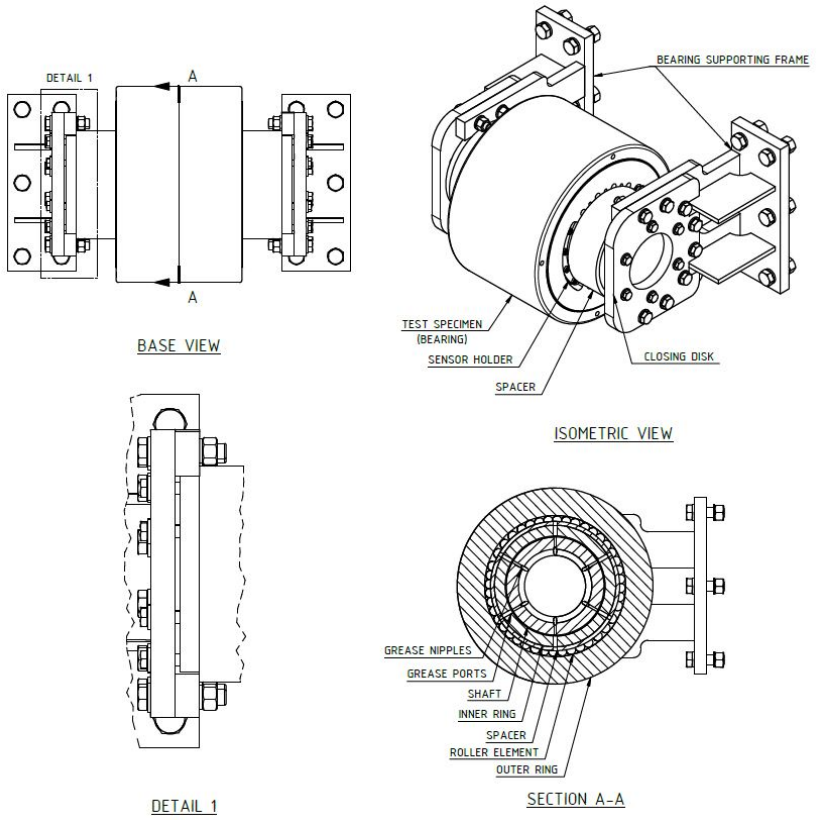

Figure 4.14: 2D drawings of bearing support, (left-top) front view with reference to detail view, (left-bottom) detail view of connection between bearing supporting frame, spacer and shaft, (right-top) isometric view of bearing support and (right-bottom) cross-section at location A-A of bearing support.

4.3 Lifetime prediction

To determine the lifetime of the bearing, the basic rating lifetime L_{10} is used. The L_{10} is defined as the lifetime in number of cycles associated with 90% reliability and 10% probability of failure of the bearing operating under similar load and speed conditions according to ISO 281 [130]. In a tribological study by Allseas [126] it was observed that the rollers have insufficient crowning which caused raised edges in both raceways. It is expected that when the L_{10} is fully consumed, fatigue damage will be developed.

The procedure to calculate the basic rating lifetime for roller bearings is defined by ISO 281 [130], which states that

$$L_{10} = (\frac{C_r}{P_r})^{\frac{10}{3}}, \tag{4.7}$$

in which C_r is the basic dynamic radial load rating [N] and P_r the dynamic equivalent radial load [N].

The basic dynamic radial load rating C_r can be determined by

$$C_r = b_m f_c (i L_{we} cos(\alpha))^{\frac{7}{9}} * Z^{\frac{3}{4}} * D_{we}^{\frac{29}{27}}, \tag{4.8}$$

where b_m is the rating factor [-], D_{we} the diameter of the roller [m], i is the number of rows [-], f_c is the geometry factor [-], L_{we} the effective length of the roller [m], Z the number of rollers [-] and α the contact angle.

The geometrical factor can be determined by:

$$f_c = \frac{D_{we} cos(\alpha)}{D_{pw}} \tag{4.9}$$

where D_{pw} is the pitch diameter of the bearing.

The maximum load which the test set up can exert is 490 kN. The bearing is not radially supported but is supported on a flat surface (line contact) see figures 4.15 and 4.16 respectively. In the definitions of ISO 281, it is assumed that the outer ring has a stiff and radial support to maintain the relatively small elastic deformations in comparison to the Hertzian deformation at the contact between elements in the rolling contact. This assumption is not valid for the test conditions with the test specimen. Due to the deformations of the outer ring, it has a significant influence on the load distribution over the rollers.

From an earlier finite element analysis by Allseas [131], it has been concluded that supporting the wheel on a rail results in an increased load on the bearing in comparison with a radial support. If the wheel is supported on the rail, the rollers are subjected to a load which is 1.7 times higher than a wheel which is supported radially. This factor is only valid for the 400 mm TLS wheel. For other wheel sizes, different factorial increases were concluded. This means that the dynamic equivalent radial load P_r should be multiplied by this factor to compensate for the rail support.

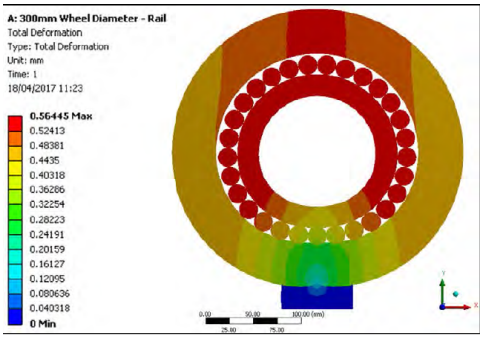

Figure 4.15: FEM analysis of a 300 mm bearing supported on a rail

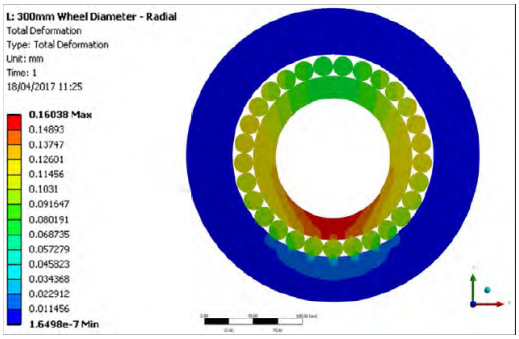

Figure 4.16: FEM analysis of a 300 mm bearing radially supported

The basic dynamic load rating $C_r = 1749$ kN and its corresponding $L_{10} = 11 * 10^6$ cycles. The maximum speed of the bearing is 60 rpm, which relates to 3056 hours of testing. Within the scope of the research, it is not efficient to run the test for such a long time. In order to reduce the amount of cycles, 34 rollers per raceway are removed and replaced by polytetrafluoroethylene (PTFE) rollers of 19.5 mm diameter. So, 8 steel rollers will remain per raceway. The PTFE rollers have the function to keep the steel rollers at their place. It is assumed that they do not carry significant load. By reducing the number of steel rollers, the applied load on the bearing is distributed on less steel rollers which results in an increase of contact stresses between the rollers and raceways. Thus, the damage development will occur faster. According to the equations 4.1 - 4.3, the dynamic load rating for 8 steel rollers per raceway is $C_{r,8} = 504kN$ and corresponding basic rating life time $L_{10} = 1.75 * 10^5$ cycles for a load of 490 kN. However due to failure of a beam in the test set up, the maximum load applied on the bearing was reduced to 343 kN for safety of the machine. More details can be found in 4.4 Test plan: Baseline test. According to the reduced maximum load, the total basic rating lifetime is $L_{10} = 6.33 * 10^5$ cycles. Since the bearing consumed already 40% of its L_{10}, the number of cycles left to fully consume its lifetime is reduced to $\mathbf{3.8 * 10^5}$ **cycles** which corresponds to **105 hours** of testing. The relation between the number of rollers, basic dynamic load rating and basic rating lifetime is shown in figure 4.19.

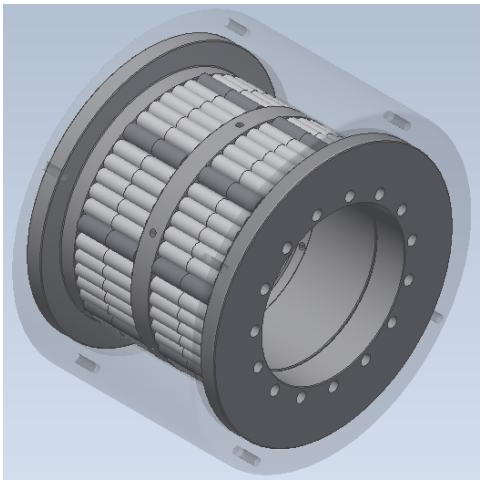

Figure 4.17: 3D view of roller configuration

Figure 4.18: Top view of first raceway roller configuration in bearing

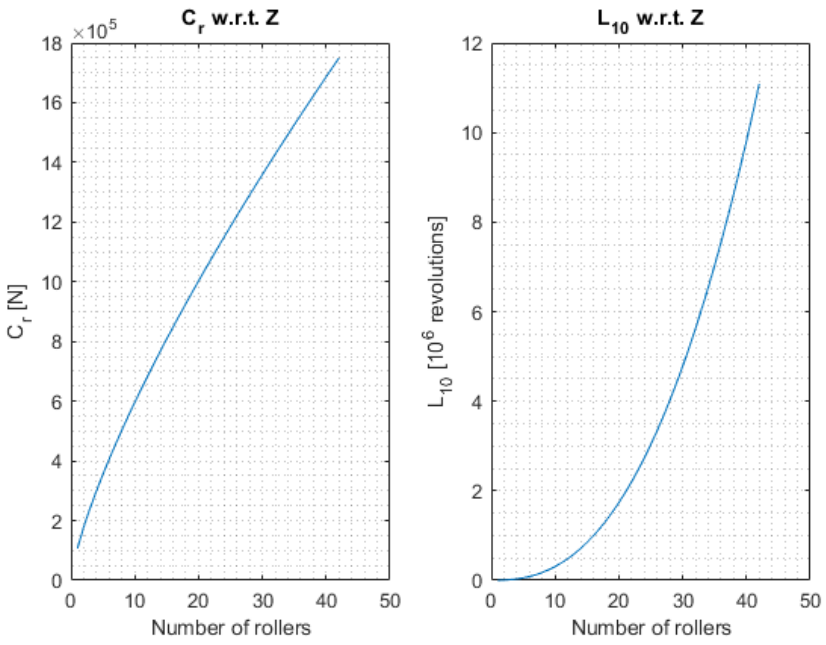

Figure 4.19: Relation between number of steel rollers, basic dynamic load rating C_r and basic rating lifetime L_{10}

The choice of 8 rollers depends on the L_{10}, deformation of the outer ring and stresses in the outer ring. Reducing the number of steel rollers results in a lower L_{10} and thus faster damage development. On the other side, the distance between two rollers increases which results in a distance in which the outer ring is not supported by rollers. This results in higher stresses, deformations and possible earlier failure of the outer ring itself. This is undesirable since the aim is to create damage in the inner ring. The inner ring remains stationary and will continuously cyclically loaded on the same area by the steel rollers passing by. Damage is mostly expected to create there, which makes it a suitable location for taking measurements. Furthermore, deformation of the outer ring can result in loading and deformation of the PTFE rollers. From a FEA and analytical strength calculation it becomes clear that the stresses and deformation of the outer ring are more acceptable with a 8 steel roller configuration than with a 4 steel roller configuration. With a 8 steel roller configuration per raceway, the bending stress of the outer side is reduced from 280 MPa to 130 MPa and for the inner side from 430 MPa to 200 MPa.

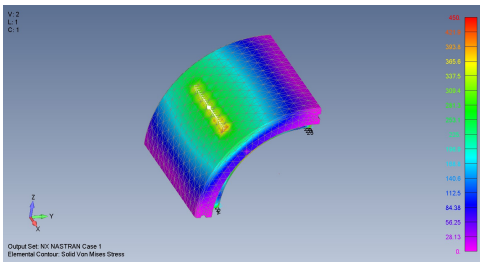

Figure 4.20: FEA of outer ring, VM-stress plotted for outer side. Max. VM-stress = 280 MPa

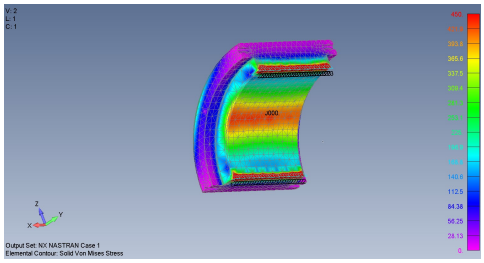

Figure 4.21: FEA of outer ring, VM-stress plotted for inner side. Max. VM-stress = 430 MPa

Contact stress at inner ring

Bearings differ in size and capability and to better compare the applied loads in the experiments on different sizes of bearings, the contact stress between the roller and inner ring is calculated.

To determine the contact stresses for different loads on the test specimen in the specific test set up, a finite element model has been made. An analytical approach has also been used to determine the contact stresses, for validation. For calculation of the contact stresses, a finite element model has been

made with the same conditions as in the test set up. In the model, the shaft of the bearing is pushing the bearing on a fixed plate geometry. The fixed plate geometry represents the rigid large modified test pipe. At the contact points of the rollers, inner ring and outer ring, a very fine mesh has been applied to accurately determine the contact stresses. With help of the finite element model, the load distribution on the rollers is identified and is used as input for the analytical solution. For the analytical solution, the equation for the Hertz contact stress as shown in eq. 4.1 - 4.3 are used.

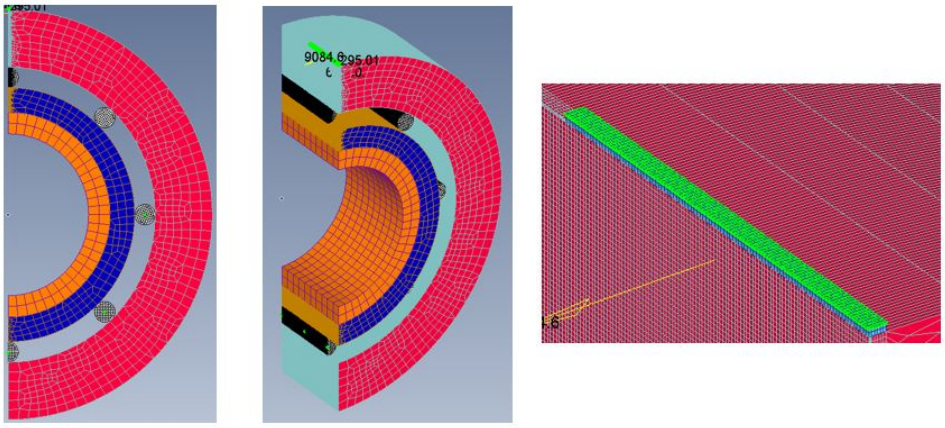

Figure 4.22: FEM model of test specimen to determine the contact stress, (left) front view bearing model; colors represents bearing parts, (center) isometric view of model and (right) fixed plate geometry

From the FEA, the maximum contact stresses at the inner ring were determined and are plotted for six load cases in figure 4.23. The analytical solution for the maximum contact stress is also plotted in the same figure. From the results, it is observed that the contact stresses of both methods corresponds. The mean between these contact stress values will be chosen to proceed with. The loads marked with a red star, will be applied on the test specimen during the baseline test and influence of operational conditions test, which will be motivated in the section 4.4 test plan.

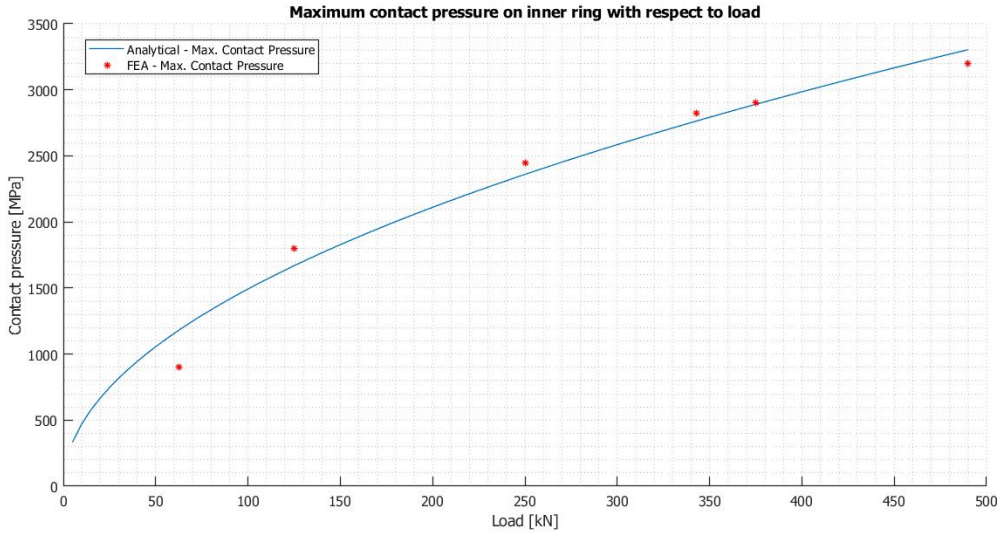

Figure 4.23: Results for the maximum contact pressure with respect to applied load for FEM and analytical solution

4.4 Test plan

As mentioned in the introduction, the aim is to perform 4 types of experiments. At first, a baseline test will be performed, secondly a test to investigate the influence of AE activity by loading the slightly worn side of the inner ring of the bearing, thirdly the fatigue test will be performed and finally the contamination lubricant test. In this section, the way all test will be performed will be further discussed.

Baseline test

The objective of the baseline experiment is to capture the ultrasonic background of the intact bearing and test machine at different operational conditions without the aim of creating damage. This will be used as a reference for the AE activity during the fatigue test and test on slightly worn inner ring. For this test, the most reliable results would have been obtained in case a new bearing would be used as test specimen. Regarding the costs, this option has not been chosen. Since the aim of the fatigue test is to create damage in the inner ring the undamaged side (fig. 4.6) will be faced towards the test wheel. It is not expected that the undamaged side would create AE signals since there are no cracks or traces of wear.

To get more insights on the influence of load and speed conditions in the acoustic emission of the baseline test, the test will be performed for a range of speed and load conditions. The load and speed conditions are the test input parameters used for the experiments. These and the sequence of testing are provided in the test matrix shown in figure 4.2. The applied load conditions and corresponding contact stresses are determined according to experiences of machine operators and by a study of Yunfeng and Lei [132]. The commonly appearing contact pressures for slew bearings in offshore cranes are between a range of 2750 MPa and 4000 MPa and for turret bearings, 1500 MPa is experienced as a safe limit according to machine operators. The study of Yunfeng and Lei verifies that the contact pressure in slew bearings is within the above mentioned range. The intention was to include the maximum load the test set up can exert in the test matrix, however during a preparatory test at 490 kN the cylinder connection beam failed instantly, see figure A.47. A new beam was design with stiffeners to proceed with the baseline test, see figure A.48. More information can be found in chapter 5.1 Results and discussion: Baseline test. To reduce the risk for failure of other components, the maximum applied load for the all experiments were decreased to 343 kN which corresponds to a contact stress of 2800 MPa. According to these properties, contact pressures between a range of 1050 to 2800 MPa are used for the load conditions.

Bearing speed **Contact stress and applied load**	**7.5 RPM 0.16 m/s**	**15 RPM 0.31 m/s**	**30 RPM 0.63 m/s**	**60 RPM 1.25 m/s**
1050 MPa 62.5 kN	225 rev. 30 min	375 rev. 25 min	600 rev. 20 min	900 rev. 15 min
1750 MPa 125 kN	225 rev. 30 min	375 rev. 25 min	600 rev. 20 min	900 rev. 15 min
2400 MPa 250 kN	225 rev. 30 min	375 rev. 25 min	600 rev. 20 min	900 rev. 15 min
2800 MPa 343 kN	225 rev. 30 min	375 rev. 25 min	600 rev. 20 min	900 rev. 15 min

Table 4.2: Test matrix for baseline test and test on slightly worn side of inner ring

Test on slightly worn side of inner ring

To understand the acoustic emission on a slightly worn side of the inner ring (fig. 4.5), the same test conditions as the baseline test are performed. The slightly worn side consist of tracks of wear and with this test insights will be developed in how the AE signals can be measured on a worn inner ring. The measurements will be compared with the baseline test.

Duration test

The aim of the fatigue test is to develop damage in the bearing, especially in the inner ring by constantly cyclic loading it while measuring the AE activity. With these measurements, it will be possible to relate these with the visual damage and lubrication analysis. For this experiment, the same bearing used for the baseline test and test on slightly worn inner ring will be used. The slightly worn side of the inner ring will be faced opposite to the test wheel, and will be constantly cyclic loaded.

Since the maximum applied load was lowered to 343 kN instead of 490 kN, the basic rating lifetime L_{10} still available increased to $3.8 * 10^5 cycles$ which corresponds to 105 hours of testing at 60 rpm bearing speed. The expectation is that every working day, 6 hours of testing can be reasonable achieved. Continuously unattended overnight testing is not considered due to safety concerns. The intention is to perform an intervention if $\frac{1}{3}$ of the remaining L_{10} is consumed which corresponds to approximately 34 hours. During the intervention, the bearing assembly as shown in figure 4.14 will be disassembled and the damage of the bearing parts will be inspected. A visual inspection and dye-penetrant inspection of the damage will be performed. Furthermore, lubrication analysis will be performed on 3 grease samples taken from different locations of the bearing, 2 samples are taken at the loaded side of the bearing and 1 sample 180 degrees opposite, see figure 4.24 for more specifications. With the lubrication analysis, an indication of the developed wear will be made possible.

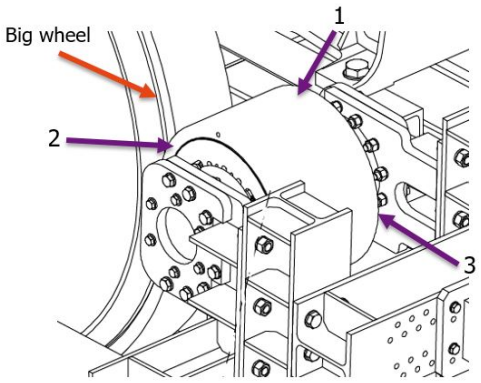

Figure 4.24: Specification of grease sample locations

Contamination experiment

The aim of the contamination test is to understand the influence of contamination particles on the AE activity. Furthermore, it will be investigated whether it is possible to provide an indication of contaminated lubricant with AE activity. For this, another TLS-wheel will be used with similar traces of wear and a same consumed basic rating life time. In this test, no PTFE rollers will be used, since the aim is not to create damage. The lubricant will be contaminated with 10 μm iron particles in 3 different concentrations. At first, the bearing will be tested with clean grease on a load 343 kN and speeds of 7.5 RPM and 60 RPM. Hereafter, the bearing will be tested with contaminated grease. According to the contamination limits of Rothe Erde [133], a slew bearing manufacturer, a report by Gulf Marine [134] and experiences by machine operators, the contamination levels were determined. A safe concentration is below 1500 mg Iron per kg grease. A level to pay attention is set at 10.000 mg/kg and a level for immediate action is set at 20.000 mg/kg. Mixing of the grease will be performed by an electric mixer and measurement with a scale of accuracy 10 mg. A test matrix is provided in table 4.3.

	Bearing speed	**7.5 RPM 0.16 m/s**	**60 RPM 1.25 m/s**
	Contact stress and applied load		
Clean grease 0 mg Fe/kg grease	1900 MPa, 170 kN	113 Rev. 15 min	900 Rev. 15 min
	2800 MPa, 343 kN	225 Rev. 30 min	1800 Rev. 30 min
Sample 1 1.5 mg Fe/kg grease	1900 MPa, 170 kN	113 Rev. 15 min	900 Rev. 15 min
	2800 MPa, 343 kN	225 Rev. 30 min	1800 Rev. 30 min
Sample 2 10 mg Fe/kg grease	1900 MPa, 170 kN	113 Rev. 15 min	900 Rev. 15 min
	2800 MPa, 343 kN	225 Rev. 30 min	1800 Rev. 30 min
Sample 3 20 mg Fe/kg grease	1900 MPa, 170 kN	113 Rev. 15 min	900 Rev. 15 min
	2800 MPa, 343 kN	225 Rev. 30 min	1800 Rev. 30 min

Table 4.3: Test matrix contamination test

4.5 Measurement system

The AE measurements are performed with the AMSY-6 measurement system of Vallen Systeme [88]. This measurement system consist of the MB6-V1 chassis which is composed of 6 dual channel signal processors connected to 12 AEP5 preamplifiers and 12 AE sensors. A simplified overview of this measurement system is shown in figure 2.11. The measurement system in the test set up is shown in figure 4.25 and a real time measurement with the measurement system is shown in figure 4.26.

Figure 4.25: AE measurement system installed in test set up

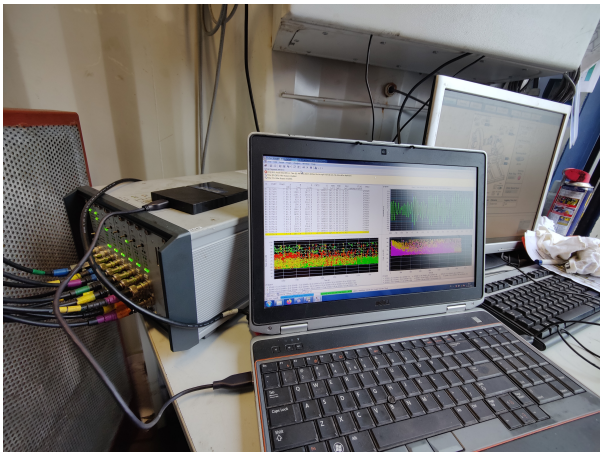

Figure 4.26: AMSY-6 Measurement system - real time measurement

To measure a broad frequency band of signals, 3 different types of AE sensors are used with a measurable

frequency range of 40 kHz to 580 kHz. AE sensors are piezoelectric sensors with a piezoceramic element which consist of high sensitivity in measuring microscopical deformations due to AE waves. The low-frequency signals are being measured by the R6α sensor having a 60 kHz resonant frequency and frequency range of 40 kHz to 100 kHz. The mid-frequency signals are being measured with the R15α sensor having a resonant frequency of 150 kHz and frequency range of 95 kHz to 180 kHz. The R6α and R15α are resonant type sensors which are highly sensitive for AE waves with a certain resonance frequency. AE waves with this resonance frequency will be repeatedly reflected and emphasized within the transfer element of the sensor. Other frequency components are more quickly attenuated within the transfer element. For the measurement of high-frequency signals, the broad band WSα sensor with a frequency range of 180 kHz to 580 kHz is used. The broad band sensor has a relative uniform frequency response in comparison with resonant sensors. The transfer element in the sensor is covered with a damping material to prevent resonance of waves. Broad band sensors are often used for waveform analysis. The sensitivity of the sensors is shown in figure 4.27.

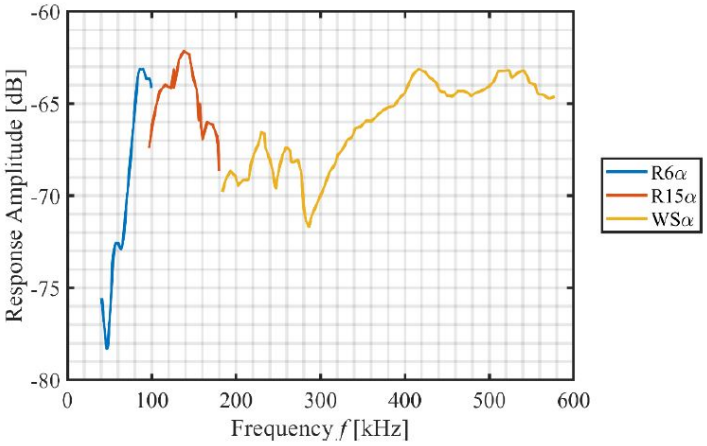

Figure 4.27: Sensor responses for the R6α, R15α and WSα

The measured transient waves are sampled with 5 MHz sampling rate and a threshold of 55 dB is applied. AE waves are recorded if its amplitude is beyond 55 dB. The threshold is determined by performing a dummy test on the bearing with the test conditions applied from the fatigue test. The peak amplitude of the noise and an addition of 6 dB is taken as the threshold as recommended by Vallen Systeme [88]. Silicon grease is used as coupling medium, to prevent any gaps between the connection. Grease does not deteriorate or run down during the measurement.

Sensor positioning

Since the aim of the fatigue test is to create damage at the inner ring and the inner ring is stationary, the sensors will be positioned at the inner ring. In this way, the sensors will be positioned as close as possible to the AE sources. To create space for the sensors at the inner ring, the flanges of the bearing are modified by milling pieces around the circumference. The 3 different types of sensors mentioned before will be placed together as a set on the inner ring, to capture the broad frequency of signals at the same spot. 4 of these sets of sensors will be positioned to obtain an indication of the damage location in circumferential and longitudinal direction. An overview of the sensor positioning in the test set up, and its numbering is provided in figure 4.28.

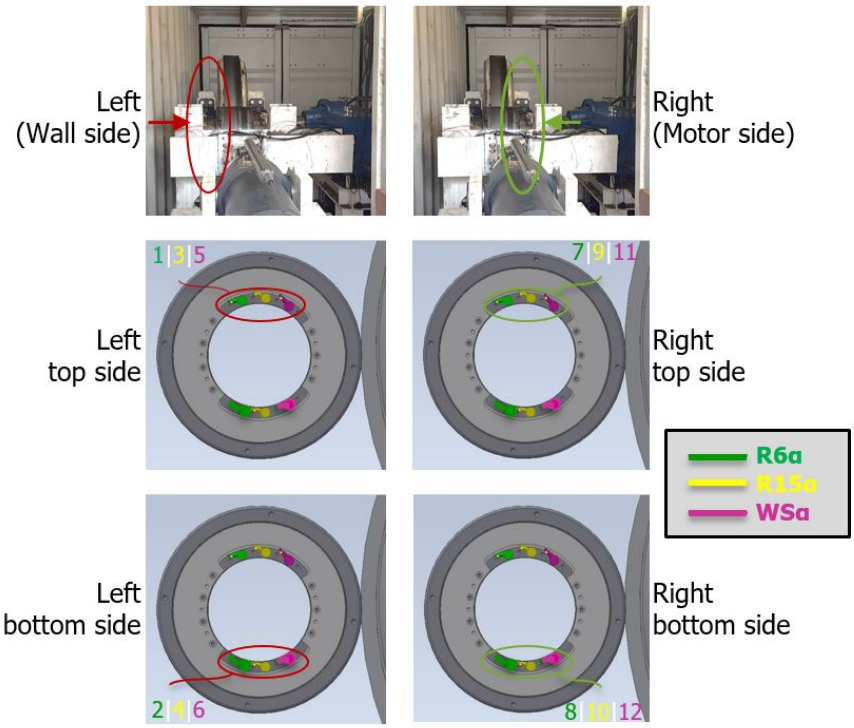

Figure 4.28: Sensor positioning in set up and its numbering

Mounting

The sensors are mounted with a steel plate which presses on top of the sensors and keeps them on their place. To prevent gaps between the connection of the inner ring and sensor and to enhance signal transmission, silicon grease is used as a coupling medium. Silicon grease will not deteriorate or run down during the time of measurement. Before and after conducting an experiment, the sensitivity and mounting of the sensors are checked by performing pencil lead breaks. The responses by the sensors are checked and should not differ more than 3dB. A set of sensors mounted on the inner ring, is shown in figure 4.29.

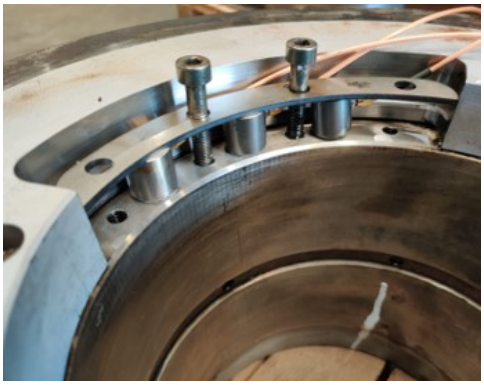

Figure 4.29: A set of sensors mounted on the inner ring

4.6 Data processing methods

From the performed experiments, raw measurement data is obtained which needs to be processed to be well interpreted. The data processing consist of three steps, pre-processing, processing and post-processing. In the first step, pre-processing, a signal-to-noise filter (SNR-filter) is applied on the AE measurement data to distinguish between burst and continuous type of signals and the cycles are counted using the same measurement data. The second step, processing, the processed AE measurement are evaluated to detect trends in AE activity and similarity of wave forms is studied. In the post-processing part, ways for visualizing the measurements are presented.

4.6.1 Pre-processing

In the pre-processing step, the SNR-filter and cycle counting method are applied and further elaborated in this section.

Signal-to-noise filter

AE signals can be distinguished between burst type and continuous type of signals as was mentioned earlier in the literature review. Burst type of waves are characteristic for crack initiation and propagation. By distinguishing this type of signals from the raw data, meaningful data about damage development can be extracted. Separation of both types of signals can be achieved by applying a signal-to-noise ratio filter. The signal-to-noise ratio is defined as the ratio between the peak amplitude of the signal (A_p) and peak amplitude of the noise (A_n).

$$r_{SNR} = \frac{A_p}{A_n} \tag{4.10}$$

The peak amplitude of the signal is obtained by calculating the maximum amplitude from the signal $f(t)$.
Before the noise amplitude can be determined, a time window is defined. This window depends on the length of the recorded pre-trigger. The pre-trigger is the onset recorded signal prior to crossing the threshold, so before the rise in amplitude. The time window is defined by,

$$t_{SNR} = \begin{cases} 0 & \text{if}, t_{preT} \leq t_{preTmin} \\ (1 - (\frac{t_{preT} - t_{preTmin}}{2t_{preTmin}}))t_{preT} & \text{if}, t_{preTmin} < t_{preT} < 2t_{preTmin} \\ \frac{1}{2}t_{preT} & \text{if}, 2t_{preTmin} \leq t_{preT} \end{cases} \tag{4.11}$$

where, t_{SNR} is the length of signal-to-noise time window, t_{preT} the pre-trigger time and $t_{preTmin}$ the minimum prescribed pre-trigger time.
Within the described time window, the peak amplitude of the noise can be determined by,

$$A_n = max(f(t < t_{SNR})) \tag{4.12}$$

Using the SNR ratio, noise amplitude and signal amplitude, all waveforms from the raw data are classified between burst and continuous waves.

$$\begin{cases} r_{SNR}A_n \leq A_p & \text{classified as burst} \\ r_{SNR}A_n > A_p & \text{classified as continuous} \end{cases} \tag{4.13}$$

In case $t_{SNR} = 0$, no noise amplitude is calculated and is automatically classified as a continuous wave.

Cycle counting

The number of cycles are determined according to the constant bearing speed and the duration of the set of experiment. According to the start time of the AE measurement and stop time of the machine, the duration of the test is determined. Recording of the measurement started simultaneously with the start of the machine. The test specimen stopped rotating instantly after the stop time of the machine was reached.

4.6.2 Processing

In the processing part, the filtered raw data is used to calculate the hit-rate and similarity of waveforms to detect trends.

Hit-rate

Within the scope of the research, the hit-rate is defined as the number of measured burst waves per cycle. By defining the hit-rate with respect to the number of cycles, the differences in speed are normalised and it is more meaningful in comparison with time. The AE measurements are coupled with its cycles and are used to calculate the hit-rate.

Clustering

The emission mechanism and propagation path, defines the shape of the waveform at a specific location. In case similarities exists between waveforms, it provides an indication that the waveform is emitted from a similar AE source. The similarity between waveforms can be identified using waveform clustering. By studying the similarity between waveforms, it is possible to identify damage mechanisms and to distinguish between different damage mechanisms. Cross-corelation can be applied to quantify the similarity between two waveforms as a function of a time shift applied to one of them. This is also known as the sliding dot product. The cross-correlation is defined as,

$$(f \star g)(\tau) \equiv \int_{-\infty}^{\infty} \overline{f}(t-\tau) g(t) dt \tag{4.14}$$

where f and g are two arbitrary waveforms in the time domain. The cross-correlation is determined for each time step τ between $-t$ and t. From this range of cross-correlation values, the maximum absolute value indicates the highest similarity. If peaks or troughs aligns, the contribution on the correlation value is large. The highest similarity is used as a value to evaluate whether waves originates from the same source. The normalised cross-corelation is used to determine the similarity which varies between 0 and 1. If two waveforms have the same shape or are its polar opposite, the value is 1. In case the waveforms are not similar at all, the value is 0.

$$s_{f,g} = \max \left| \frac{(g \star f)}{\sqrt{(g \star g)(0)(f \star f)(0)}} \right| \tag{4.15}$$

For the procedure of clustering, the positive similarity values need to be converted to a negative dissimilarity value $d_{f,g}$ which is defined as,

$$d_{f,g} = 1 - s_{f,g} \tag{4.16}$$

When a large number of signals are compared to each other, considering distance rather than closeness provides a more robust procedure. As clusters form and begin to grow, it's necessary to compare various signals and thus many dissimilarities to one another. For the comparison of a new signal g to an existing cluster c, the mean dissimilarity d_g^c is used and determined by,

$$d_g^c = \frac{1}{N}\sum_{f=1}^{N} d_{f,g} \quad \text{wherein} \quad f \in c \tag{4.17}$$

The mean dissimilarity between signal g and N numbers of signal f that are elements in cluster c is determined by equation 4.17. If the cluster is large enough, the developed algorithm limits the number of signals N to be considered in this comparison to 9. These 9 signals are selected at random in threes from the original 10 signals that comprise the cluster, the last 10 signals added to the cluster, and any other wave that is a part of the cluster. If the cluster dissimilarity c g d is less than 0.3, signal g will be added to cluster c. If no cluster fits this condition, signal g is compared to the previous 500 unclustered signals. A new cluster is created if the dissimilarity with any of these signals is less than 0.3. If not, the signal is added to a collection of the last 500 unclustered signals.

4.6.3 Post-processing

The processed data is visualized in the post-processing step so that it can provide a direct indication of relevant AE activity. Bar chart are used to visualise the hit-rates with respect to speed and loading conditions during the baseline test and influence of operational conditions test. For the fatigue test, the hit-rates are plotted with respect to the number of cycles. Furthermore, the hit-rates between different sensor types are distinguished and plotted in the bar charts.

Chapter 5

Results and discussion

In this chapter, the processed measurement data are reported for the baseline test, test on slightly worn side, duration test and contamination test. Furthermore, the results and observations are discussed and research questions are answered. All experiments were performed according to the test plan described in chapter 4 - Methodology.

Before and after each test, pulsing and pencil lead break tests were performed to check for possible variations in coupling quality of the sensors. During the pulsing mode, every sensor transmits a set of waves inside the material which is detected by the other connected sensors. This procedures is repeated till every sensor transmitted a set of waves. According to the detectability of the sensors, variations in the coupling quality of the sensors can be identified. No variations in coupling quality were observed for all the performed tests. During all tests, the machine and measurements system were continuously monitored.

5.1 Baseline test

The aim of the baseline test was to investigate the AE activity for the undamaged side of the inner ring and to quantify the background AE acitivity in operational conditions (safe limit) which will be used as a reference for the test on a slightly worn side of the inner ring and the duration test. The formulated research subquestion to be answered with the results of the baseline test is,

> How is the AE activity of an undamaged bearing under representative operational conditions?

During the test, the test matrix as shown in table 4.2 was followed. To prevent overheating of the electric motor, a break of 5 minutes was introduced for the tests on 7.5 RPM after 15 minutes of testing and for 15 RPM after 12.5 minutes testing. However during the test at a load of 490 kN, the cylinder connection beam failed, see Appendix A.3 for more information. An additional intervention took place where the bearing was disassembled. Pictures of the bearing are shown in the Appendix A.1. From visual inspection of the bearing, no traces of increased wear than before the test were observed. Furthermore, a dye-penetrant test was performed on the inner and outer ring and no cracks were observed, pictures are shown in Appendix A.1. After the repair of the beam, the baseline test was resumed at a load case of 343 kN instead the 490 kN.

The results of the measured AE activity during the baseline test are presented in figure 5.1. The average hit-rate during each load and speed condition is plotted for each sensor type. The average hit-rate is determined by taking into account all measured hits which passed the filter. The 4 subplots provides an overview of the AE activity for different load and speed conditions and specific sensor type.

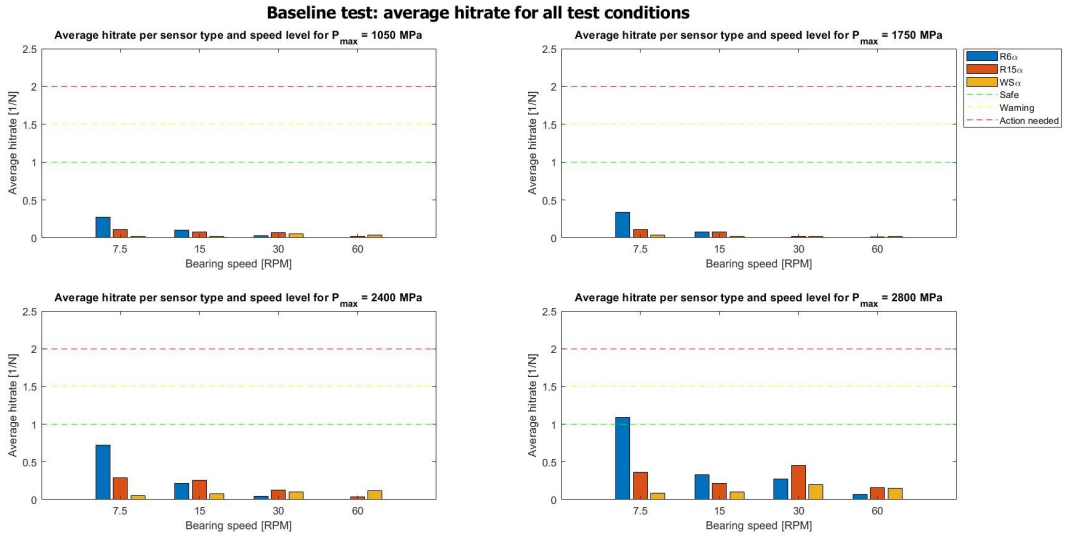

Figure 5.1: Average hitrate baseline test for all test conditions

Observations: Baseline test

- **General** - It is observed that the hitrates during the baseline test remains below 1 hits/cycle, except for the R6α sensor at 350 kN and 7.5 RPM. In that case, there was a starting effect of the bearing and acceleration in load by the hydraulic cylinder for the first 20 cycles and mixing of the grease which resulted in a much higher hitrate than the average hitrate for this speed and load level. From this test, no damage was created and a safe limit of signal emission can be defined.
- **Influence of speed** - For the different speed levels, it can be observed that there is a decreasing activity of low-frequency signals measured by the R6α with respect to increasing speed levels. When comparing the hitrate for every 10 cycles for the R6α sensor, the decreasing trend in hitrates is still noticable. For sensor types R15α and WSα no significant difference in hitrates between different speed levels is observed.
  - For example for a load of 350 kN and comparing the hitrates of the R6α with a speed of 7.5 RPM and 60 RPM: The hitrate for 7.5 RPM is 1.1 hits/cycle and 60 RPM is 0.1 hits/cycle. The difference in hitrate can be explained due to frictional effects and rubbing of the roller and raceways at low speed which generate AE signals. For 60 RPM, more mid- and high-frequency type signals are emitted.
  - The activity of low-frequency is more prominently present for 7.5 RPM. Frictional effects are detected by this sensor.
- **Influence of load** - An increase in hitrates can be observed for an increased load, however the increase is not significant and the hitrates for all sensor types remains below 1 hits/cyle.

From the observations of the baseline test, the posed research subquestion can be answered. The baseline test has been performed under representative speed and load levels for bearings used in the offshore industry. The AE activity expressed in average hitrate for these representative speed and load levels is shown in figure 5.1. In general, the AE activity remains below 1 hits/cycle for all speed and load conditions and all sensor types. However at a speed of 7.5 RPM and load of 343 kN an increased AE activity is observed for the R6α sensor. At speeds below 10 RPM, AE burst waves of low frequency content often originate from frictional and rubbing effects of the rollers and raceway. Therefore results of R6α at 7.5 RPM are not fully reliable to define a safe level and are not taken into account. According to the observations, an average hitrate of 1 hits/cycle is defined as a safe level for the AE activity in bearings. This is the AE activity of an undamaged bearing under representative operational conditions.

5.2 Test on slightly worn side inner ring

The aim of this test is to investigate the influence of AE activity on a slightly worn side of the inner ring and how it compares with the baseline test. The level of wear is described in 4.1 Test specimen: Prior lifetime consumption. This test was performed after the baseline test. The inner ring was 180 degrees rotated with respect to the position of the inner ring in the baseline test. The test matrix shown in table 4.2 is applied for this test. The results of this test will help in answering the following research subquestion,

> How is the AE activity of a worn bearing under representative operational conditions?

The average hitrate for each speed and load condition and per sensor type is presented in figure 5.2. The results are presented in the same visuals as the results of the baseline test in figure 5.1 for convenient comparison.

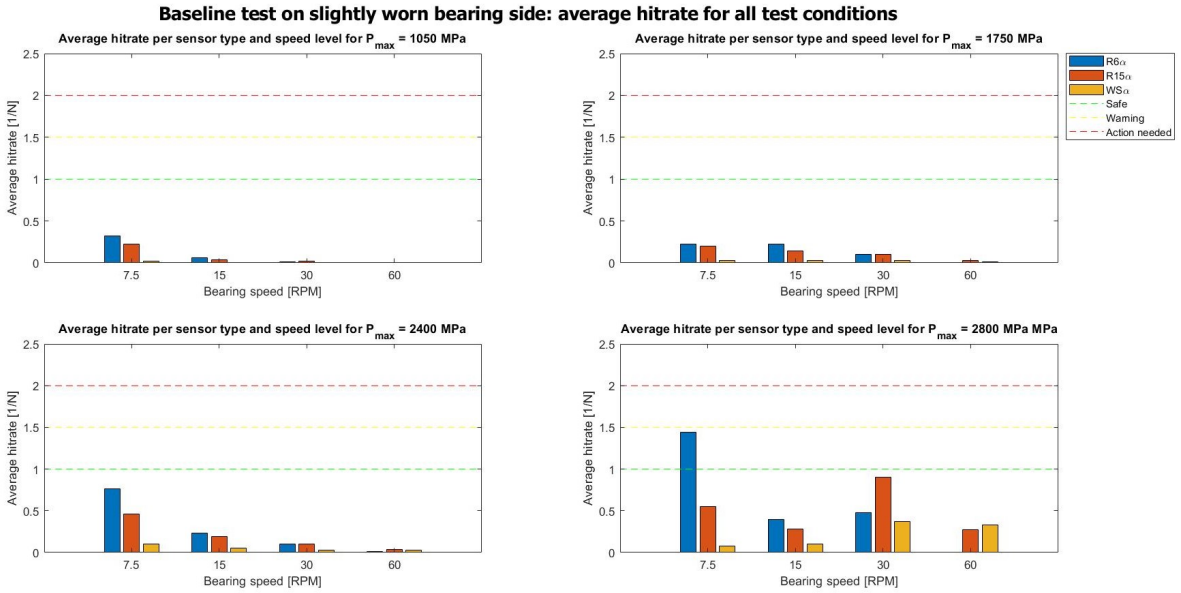

Figure 5.2: Average hitrate for baseline test on slightly worn side for all test conditions

After this test, the fatigue test was directly started without performing an intervention. So no visual inspection was performed on the bearing.

Observations: Test on worn side inner ring

- **General** - No significant difference in average hitrate was observed for the different load and speed conditions and sensor types for this test on a slightly worn side, in comparison with the baseline test.
- **Influence of speed and load** - The influence of speed and load on the average hitrates is similar as the baseline test.

From these observations, the posed research subquestion can be answered. The AE activity of a worn bearing under representative operational conditions is comparable with the baseline test, no significant difference in hitrate is observed. The bearing was not sufficiently long loaded to develop wear, therefore the AE activity is similar as the baseline test. The presence of wear can result in small differences in hitrates.

5.3 Duration test

The aim of the duration test is to investigate the AE activity with the aim of developing damage by constantly cyclic loading of the bearing and to provide an indication of damage development with the AE measurements. The testing procedures are described in chapter 4.4 Test plan: Duration test. The results will help to answer one of the main research questions of this thesis:

> How can Acoustic Emission be applied to assess the damage of highly-loaded low-speed roller bearings?

During the fatigue test, the modified test wheel broke down due to failure of the welds between the structure of the wheel and its shafts due to high axial loads. The wheel was repaired by modified the connection between the shaft and wheel structure by a press fit connection and by increasing the thickness of the wheel structure. Pictures of the failed wheel and the new designed wheel are shown in figure A.49 and figure A.50 respectively.

The test was performed at 60 RPM and 350 kN load for 60,000 cycles. After every 1,500 cycles which corresponds to 25 minutes, a break of 5 minutes was performed to cool the electric motor in the machine. At the end of each day, a last test at 7.5 RPM for 190 cycles was performed to provide an indication of the AE activity at a low speed. After 60,000 cycles, the large modified test wheel failed and the test was stopped. Only, 50% of the L_10 was consumed and the bearing was tested for only 16.7 hours. The results of the average hitrate per 1,500 cycles for 60 RPM and per 190 cycles for 7.5 RPM for each sensor type is provided in a bar chart in figure 5.3. The results of the average hitrate for only 60 RPM are provided in figure 5.4.

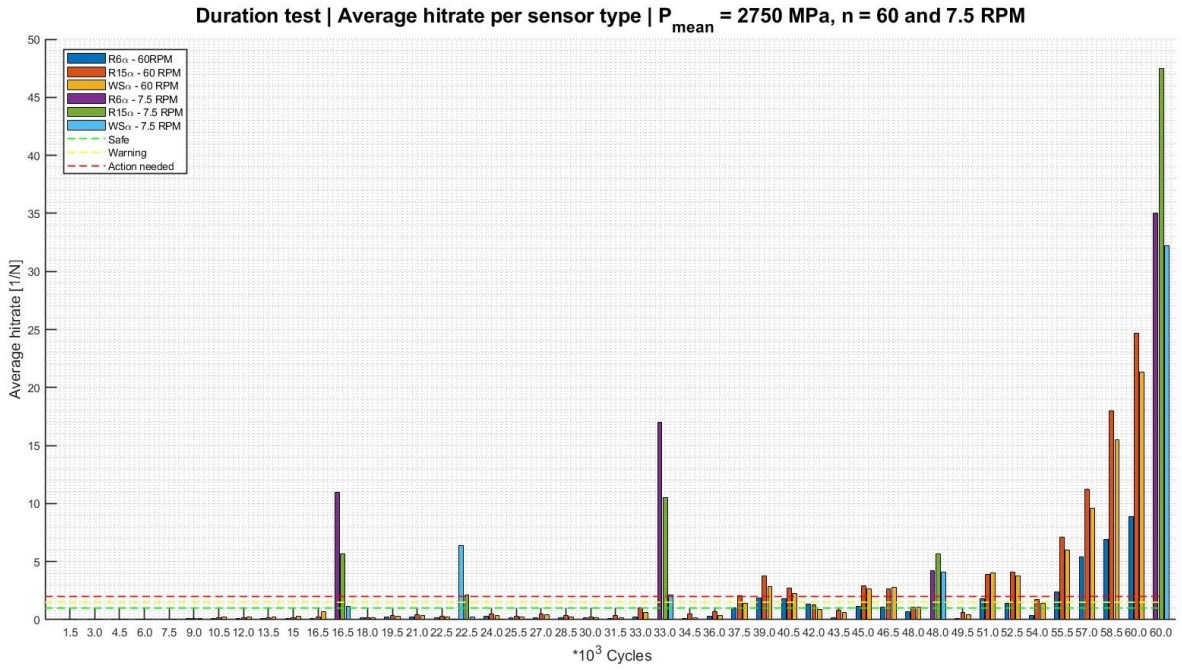

Figure 5.3: Average hitrate during duration test per 1500 cycles for 60 RPM and per 190 cycles for 7.5 RPM

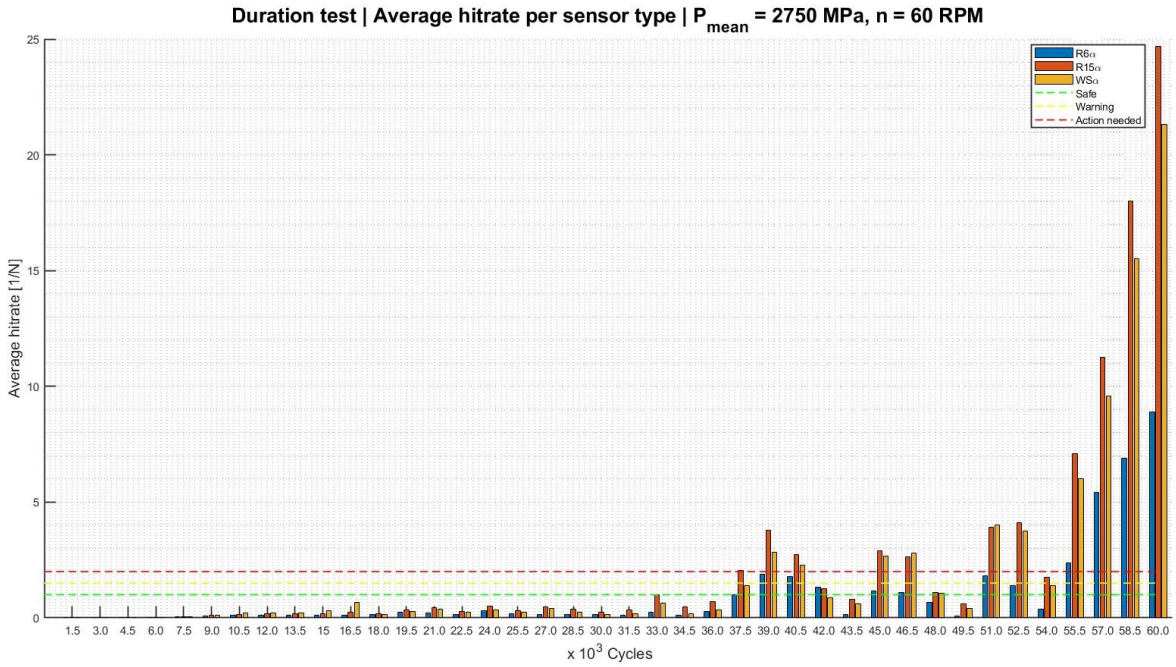

Figure 5.4: Average hitrate during duration test per 1500 cycles for 60 RPM only

Wave propagation path

Due to cracking of the welds at the shaft of the large modified test wheel, the wheel failed and the duration test was suspended. By cracking of the welds AE waves were also emitted, however these waves are not measured by the sensors attached on the inner ring of the bearing. The wave propagation path is too long and it needs to cross six interfaces before the signal reaches the sensor. The propagation path is shown in figure 5.5. Every interface the signal needs to cross, results in an attenuation of at least 20 dB, see Chapter 2.2 - Condition monitoring: AE waves for more specifications. The maximum strength of the AE signal at the source is around 100 dB [91], crossing six interfaces results in an attenuation of more than 100 dB. So the AE signals will lose all its strength. Furthermore, pencil lead break tests were performed at the location indicated with the yellow star in figure 5.5 and no signals were measured from the sensors attached on the inner ring.

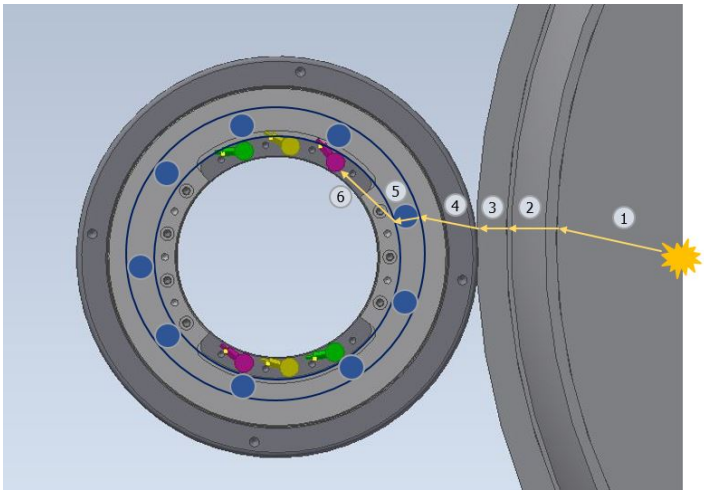

Figure 5.5: Wave propagation path of the AE source from the failed weld location

5.3.1 Samples of waveforms

Samples of waveforms were taken at specific number of cycles (1.000 - 60.000 cycles) and for each sensor type and shown in figure 5.6. From this figure, the evolution in of the waveform during the duration test is made visible. It can be observed that during the duration test, the waveforms increased in amplitude which provides an indication of wear development

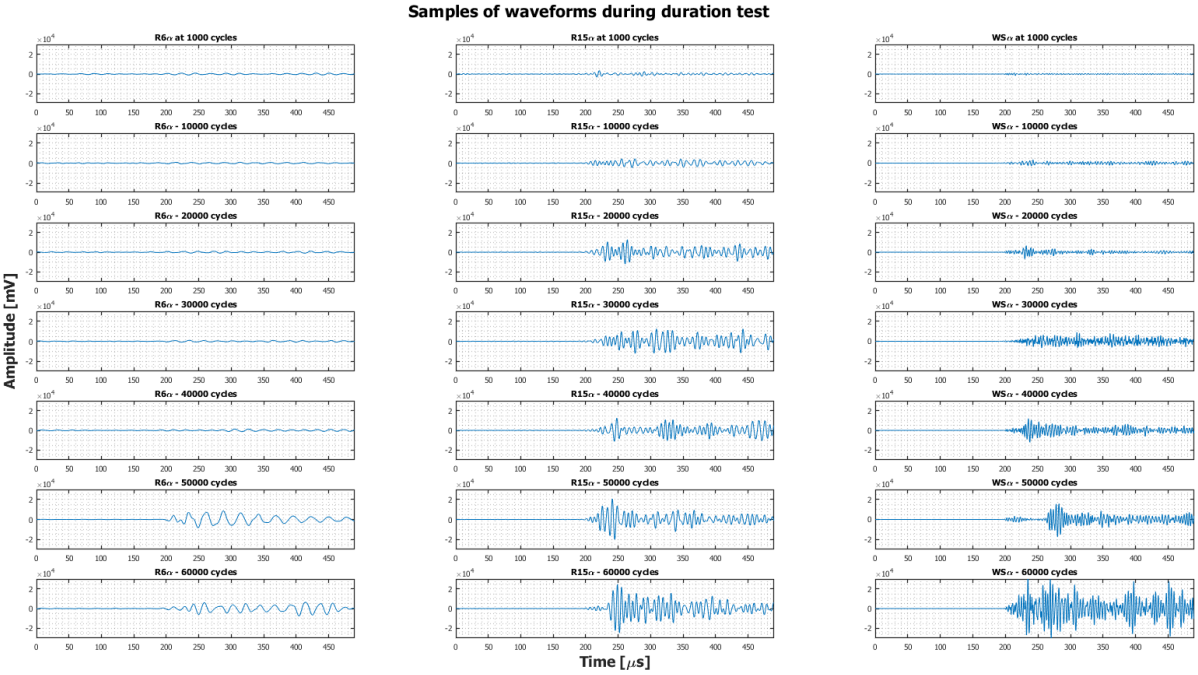

Figure 5.6: Samples of waveforms at specific intervals during duration test, $R6\alpha$ - Ch. 8, $R15\alpha$ - Ch.10 and $WS\alpha$ - Ch. 12

5.3.2 Clustering

With help of the clustering algorithm described in Chapter 4.6: Data processing methods, similarities between waveforms during the duration test were investigated. The clustering algorithm was applied on specific cycle ranges especially at locations were possible clusters of waveforms were expected from the data for the sake of computational efficiency. These clusters are shown in the figures 5.7 to 5.9, where similar waveforms are plotted at its peak amplitude and its number of cycle. Furthermore in the legend, the cluster ID is provided of which only the first number from the start represent the channel number. From the channel number, the location of the sensor in the bearing can be found in figure 4.28. By comparing the clusters of the first 18,000 cycles (figures 5.7) with the clusters at 50,000 cycles (figure 5.9) it can be noticed that the clusters increase in size and density, and waveforms increase in amplitude. These clusters show indications of wear development in the bearing. Furthermore, by comparing the peak amplitudes of the clusters and its corresponding channel number, indications of the possible location of damage development can be identified. Higher peak amplitudes and earlier starting of clusters from a specific sensor type, indicates that wear development started earlier and is more severe at the sensor location.

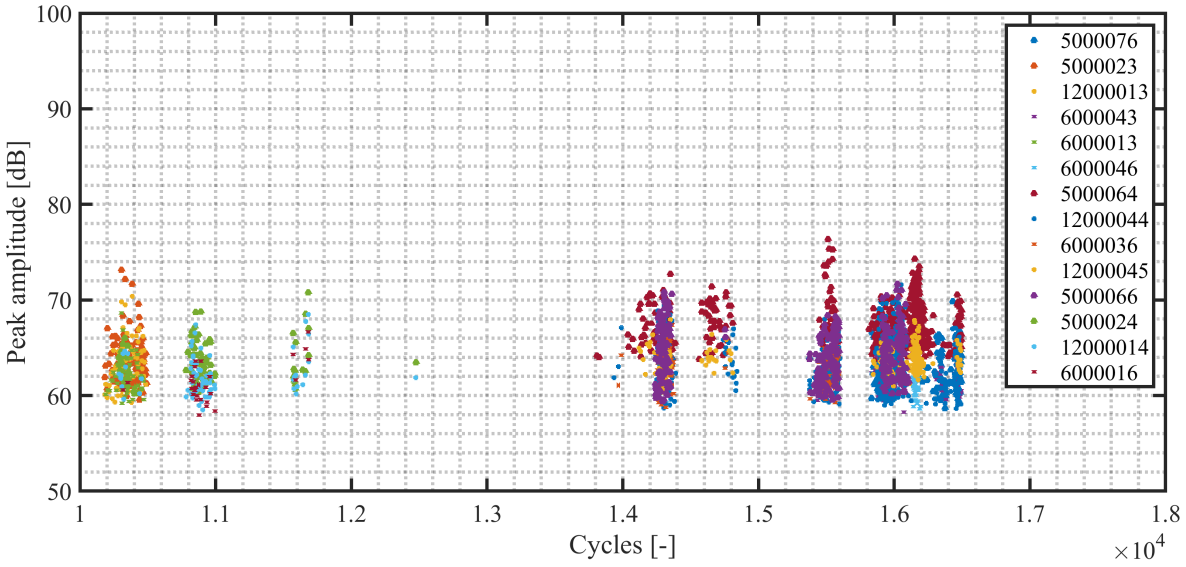

Figure 5.7: Clusters originating from channel 5,6 and 12 (High-frequency WSa-sensor) emitted between 10,000 cycles to 18,000

From 10,000 cycles till 18,000 cycles, it can be observed from figure 5.4 that the hit-rates are increasing, however still remain below 1 hits/cycle. On average, the hit-rates remain around 0.5 hits/cycle. The hit-rate corresponds to the clusters plotted in figure 5.7. At around 16,500 cycles, a higher hitrate (0.85 hits/cycles) is observed for the high-frequency waves which results in more and dense clusters. By carefully observing the clusters around 16,000 cycles, it can be noticed that the clusters originates from channel 5, 6 and 12. The peak amplitudes of channel 5 are higher than channel 12, which might imply the possibility of more damage initiation in comparison with channel 12.

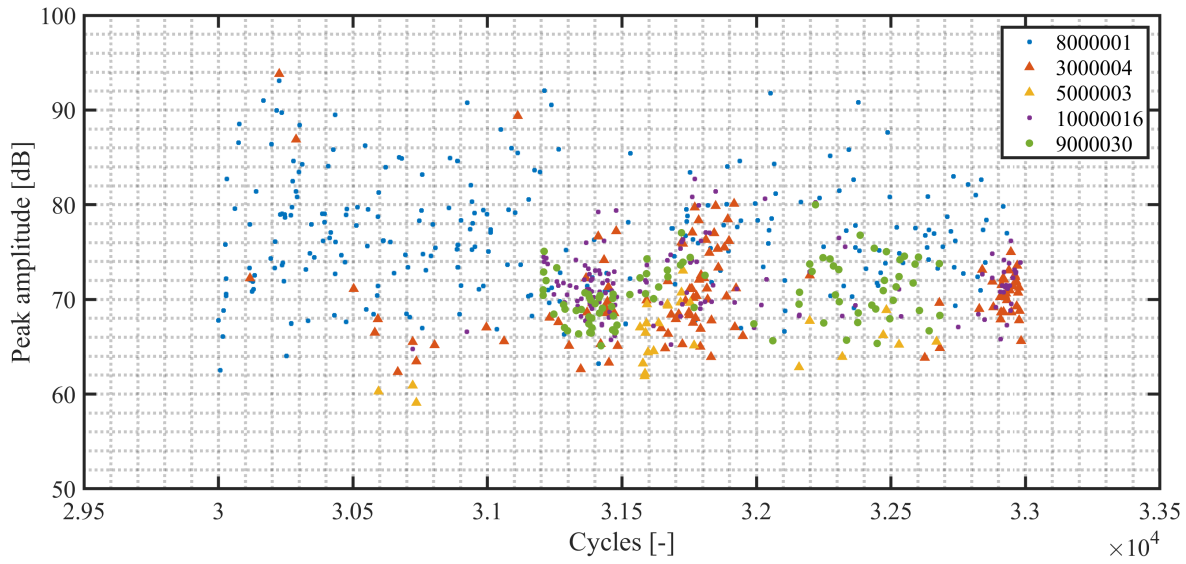

Figure 5.8: Clusters between 30,000 and 33,000 cycles for channels 3,5,8,9 and 10 (all frequency types)

The clusters between 30,000 and 33,000 cycles are not as dense as the clusters shown in figure 5.7. Although the difference is not significant, this may suggest that the start of the test is generally more noisy until the components are better settled in bearing.

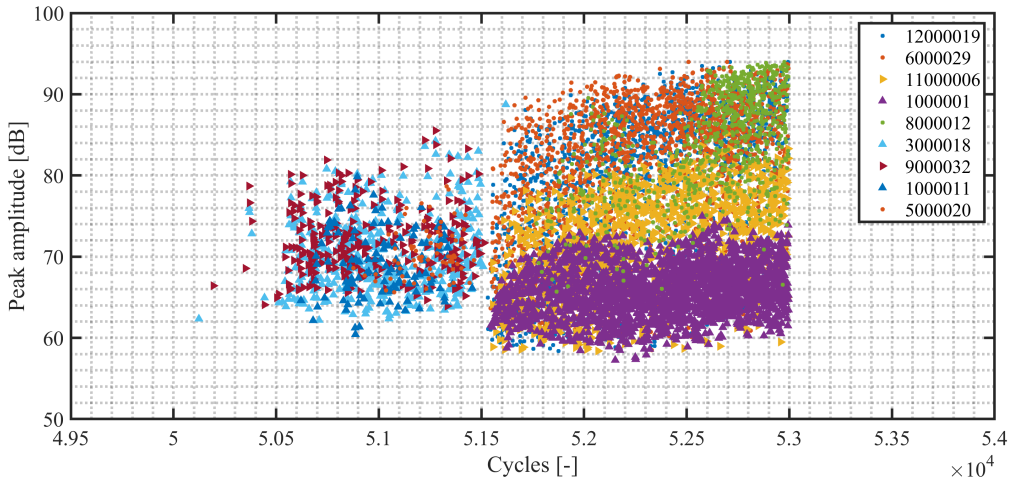

Figure 5.9: Clusters between 50,000 - 53,000 cycles for channels 1,3,5,6,8,9,10,11 and 12. -contains all frequencies

From 50,000 cycles, the clusters of waveforms starts to increase in density and in size. During testing, the test was started at 50,000 cycles and stopped at 51,500 cycles for a five minutes break. In between, the bearing was continuously running. From 51,500 cycles the test was resumed and stopped at 53,000. From 51,500 cycles, the clusters starts to increase in size, amplitude and density with respect to the previous observed clusters. A hit-rate of 2 hits/cycle for low-frequency waves and 4 hits/cycle for mid- and high-frequency waves occurs between this cycle range. By carefully investigating the clusters starting from 51,500 cycles, it can be observed that the peak amplitudes of channels 6 and 12 are higher in comparison with the peak amplitudes of channel 1 and channel 11. This means that at the locations of channel 6 and 12 most of the damage is developing. Since the peak amplitudes and the density of waveforms from channel 6 started earlier in comparison with channel 12, it means that the damage development started earlier at the location of channel 6.

5.3.3 Visual inspection

After failure of the modified test wheel, the inner ring, outer ring, radial rollers of each raceway and flanges were visually inspected for wear. A comparison of the inner ring before the duration test and after are shown in figures 5.10 till 5.13. All other pictures are provided in Appendix A.2 for all other parts. From these pictures, it can clearly be observed that more wear was developed in the inner ring. The grooves at the raceways are deeper, the worn side surface looks more shiny and mirror-like surface. Furthermore, more pitting is observed at the raceways of the outer ring and mirror-like surface is observed at the radial rollers. The raceway of the axial rollers at the flanges shows more surface pitting. Finally, a dye-penetrant inspection was performed, but no cracks were visible. The pictures of this inspection are provided in Appendix A.2.

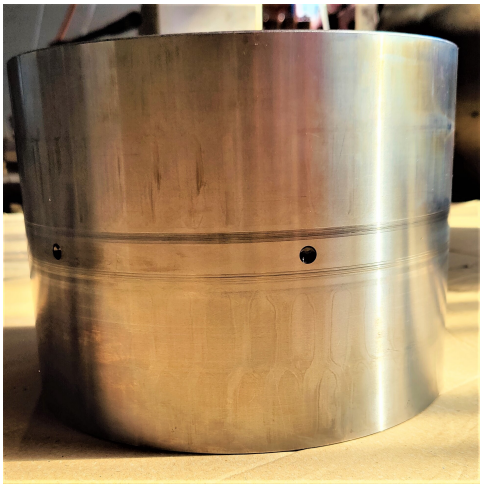

Figure 5.10: Picture of unworn side of inner ring before duration test.

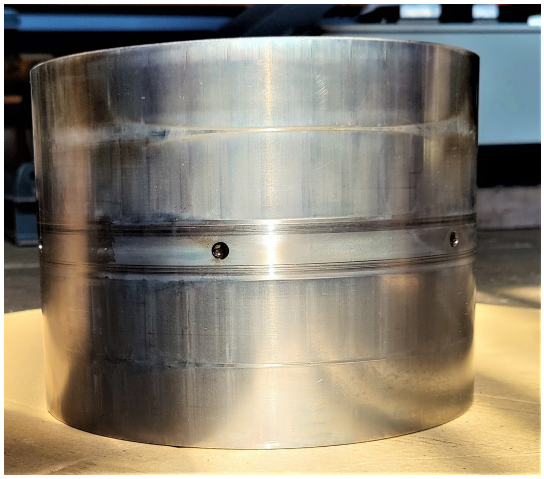

Figure 5.11: Picture of worn side of inner ring before duration test.

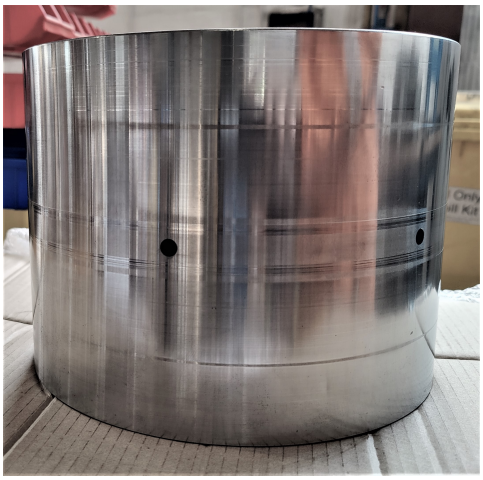

Figure 5.12: Developed wear on inner ring with respect to picture 5.10, no wear was present before test.

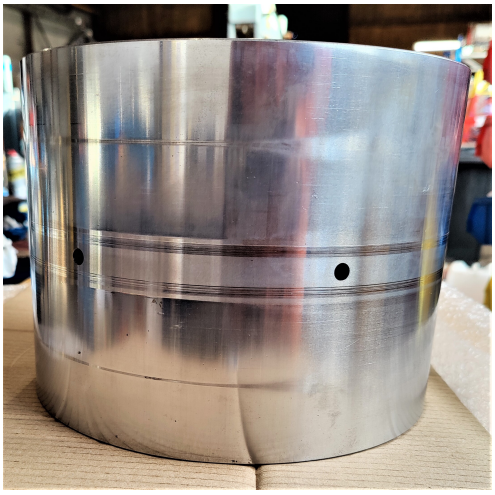

Figure 5.13: More development of wear on inner ring with respect to picture 5.11.

5.3.4 Lubrication samples

During the intervention, three grease samples were taken at different locations in the bearing as specified in figure 4.24. One sample of clean grease was taken before the test for reference. The concentration iron particles of size 5 $\mu m \leq$ in ppm and Wear Particle Index (WPI) for iron particles of size $\geq 5\mu m$ are parameters used to make observations about the wear development in bearings. The concentration limits for warning levels of bearing safety are provided by the ASTM.

The warning levels for the Iron concentration and WPI are provided in figure 5.2. The results of the analysed grease from the laboratory are summarized in figure 5.1. From the results of the grease analysis, it can be observed that all three grease samples are at attention level for the iron particle concentration and are on warning level for the WPI Index. On average, the iron concentration in the sampled grease after the test was 5,5x times larger and WPI 10x times larger compared to the clean grease level. The clean grease sample was on a safe concentration level. These results indicates the development of iron content, so wear development during the duration test.

Grease analysis results after duration test	Location				
	1 Right-front	2 Right-aft	3 Left-front	1-2-3 Average	4 Clean
Quantity					
Iron (Fe) particles <5 micron [PPM]	**5255**	**1333**	**1741**	**2776**	**522**
Iron (Fe) particles <5 micron [g/kg]	**5,3**	**1,3**	**1,7**	**2,8**	**0,5**
PQ (Partical Quantifier) Index (WPI) > 5 micron [-]	**1875**	**2507**	**1725**	**2036**	**191**

Table 5.1: Main parameters from grease analysis after duration test

Fe (PPM) (ASTM D6595)	PQ Index (Particle Quantifier) (ASTM D8184)	Water (PPM) (ASTM(D6304)	Warning Level
≤ 1500	≤ 500	≤ 2000	Bearing is Safe
≤ 10000	≤ 1500	≤ 3000	Bearing Needs Attention
> 10000	> 1500	> 3000	Bearing is at Risk

Table 5.2: Limits of contamination levels for slew bearings [135],[136] and [137]

Observations: Duration test

- **General** - From figures 5.3 and 5.4, it can be observed that the hitrates for all sensor types are increasing with respect to the number of cycles.
  - In the first 36,000 cycles, the hitrates of all sensor types remains below the safe limit. From 37,500 to 40,500 cycles, the hitrates passes the safe limit. At 37,500 cycles, there is a more or less 300% increase in hitrate with respect to the average hitrates at 36,000 cycles, which was not noticed before. This sudden increase provides an indication of possible wear development. Therefore, an action-needed limit of 2 hits/cycle was established. In between, a limit of attention of 1.5 hits/cycle is defined.
  - Three sudden increases and decreases in hitrates is noticed with peaks at 39,000, 45,000 and 51,500 cycles 3 times in the graph and after this, a sharp increase in hitrate is observed from 55,500 cycles. If zoomed in the raw data for these specific mentioned cycles, clusters of waveforms, which increase and decrease in density are observed.
  - After the duration test, wear development was visible in all parts of the bearing from visual inspection and wear development was quantified with lubrication sampling.
- **Sensor type** - From 33,000 cycles, the average hitrates of the mid-frequency waves measured by the R15α sensors are the highest in comparison with the R6α and WSα. The average hitrates are the lowest for the R6α sensor. The mid-frequency waves seems to provide a proper indication of burst wave emission (hit-rates) related to wear development.
- **Effect of speed** - 7.5 RPM shows larger hitrates in comparison with 60 RPM, especially for the R6α and R15α sensors.
  - For the R6α sensor, it is known that frictional effects generate burst waves within this low-frequency range at this low speed. Since frictional effects are also mixed in the hitrates at 7.5 RPM, it is not reliable to trust on the hitrates of R6α sensor for the purpose of detecting wear.
  - For the R15α sensor, the hitrates are very high, however the number of cycles performed in 1 set of testing are 200 cycles in comparison with the 1,500 cycles at 60 rpm. Upon normalisation of the hitrates with respect to the cycles, the hitrates from R15α remain beyond the action needed level.
  - For the WSα, it is known that within this range of frequency burst waves associated with wear development are measured and there is no significant influence of frictional effects. The hitrates do not cross the action-needed level. By monitoring the average hitrate of the WSα sensor, indication of wear development can be confirmed for the low speed (7.5 RPM) level.
- **Clustering and waveforms** By comparing the waveforms from the start of the duration test and the end, it can be observed that the waves starts to increase in amplitude. Furthermore, the clustering algorithm is applied on specific ranges of cycles from the duration test data which indicates an increase in size, density and amplitude of the clusters with increasing number of cycles. These two observations provide an indication of wear development.

From the observations, an answer to the research question posed in the beginning of this section can be provided. During the duration test, an increased AE activity with respect to the number of cycles is observed for all sensor types. Furthermore, by analysing the waveforms and applying the clustering algorithm on the data it can be observed that the waveforms increase in amplitude and waveform clusters increases in size, density and amplitude with increasing number of cycles. After the visual inspection and lubrication analysis, evidence of wear development in all parts of the bearing is provided. With these observations, it becomes evident that wear development in the bearing can be detected by means of acoustic emission. A limit of action needed of 2 hits/cycle is established on the

basis of multiple events where a sudden increase in hitrates beyond the safe limit occured. In case the average hitrate crosses the limit of action needed, there is an indication of wear development in the bearing. Furthermore, the mid-frequency sensor R15α provides a reliable indication of burst wave emission and can used for the detection of wear development.

In summary, acoustic emission can be applied to assess the damage on highly-loaded low-speed roller bearings, by monitoring the average hit-rate of burst waves and by taking in to account the defined action needed limit of 2 hits/cycles.

5.4 Contamination test

The aim of the contamination test is to understand the influence of contaminated lubricant by iron particles on acoustic emission activity. Furthermore, it will be investigated whether AE signals originating from contaminated lubricant do not mask the detectability of another degradation mechanism for example rolling contact fatigue. All testing procedures are described in Chapter 4.4 Test procedures: Lubricant contamination test. The results of this test will answer the following research question:

> What is the influence of contaminated lubricant on the emission of AE signals in highly-loaded low-speed roller bearing?

The AE activity expressed in average hit-rate is presented for all load and speed cases in a histogram and for burst waves as well as continuous waves. In figure 5.14, the AE activity is presented for raw signals, so without applying a SNR-filter. From the results of the 10 gram iron per kg grease, it can be noticed that the AE activity of the R15α sensor is lower in comparison with the 1.5g/kg and 20g/kg contamination level. By investigating the AE activity for each channel, it became evident that only channels 8,10 and 12 measured a comparable AE activity as the other contamination levels and the other channels showed a very low AE activity even lower than the clean grease case. Indications of issues with the sensitivity of the sensors at this contamination level were observed. Therefore, the results of this contamination level are not taken into account to answer the research question. From the results of the raw signals (threshold SNR = 0), it can be observed that there are indications that an increased lubricant contamination level results in an increased raw AE activity of mid-frequency waves (R15α) in comparison with clean grease.

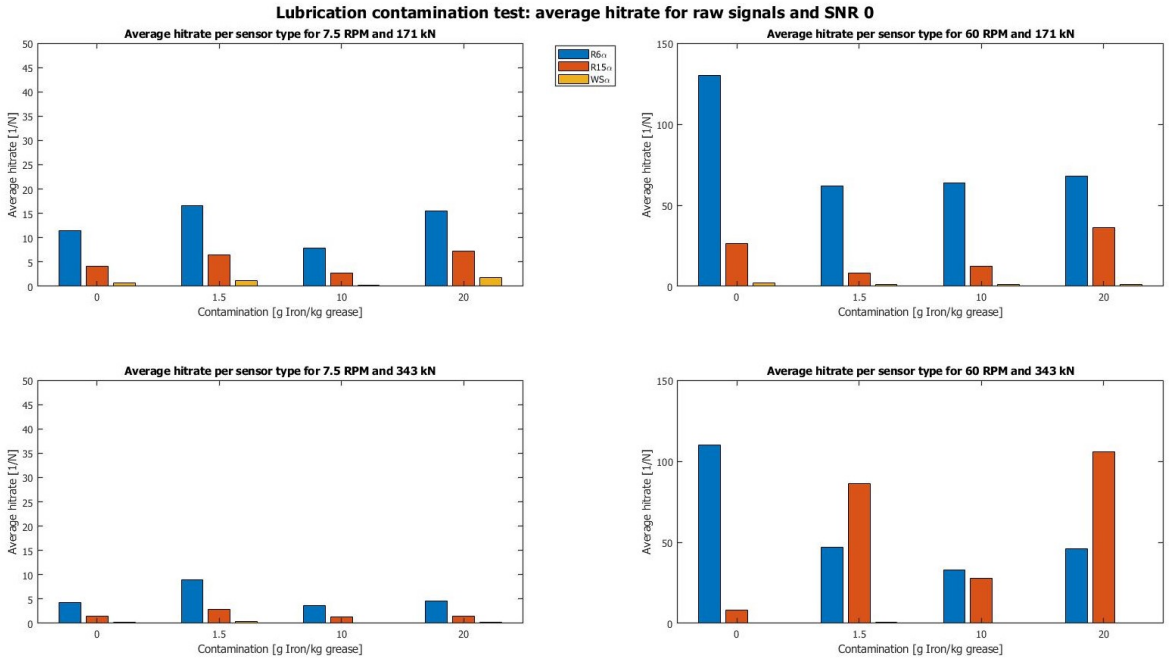

Figure 5.14: Lubrication contamination test: hitrates of raw signals (SNR=0)

For a SNR-threshold of 15, there is no AE activity of burst signals at 60 RPM, see figure 5.15. Comparing this activity with the AE activity during the duration test, contaminated lubricant is not masking the detection of failure due to rolling contact fatigue. For a speed of 7.5 RPM, some AE activity of burst signals is present, however still at a low level that it could not mask the AE signals from the duration test. From the AE activity of the continuous waves shown in figure 5.16, an increase in AE activity with respect to increased contamination levels is observed. By filtering the raw data with a SNR-threshold

of 15, still indications of contaminated lubricant can be observed from the continuous waves. At SNR-thresholds 2 and 5, the AE activity of burst waves is beyond the action needed limit defined from the duration test which may mask the detection of failure due to rolling contact fatigue. The results of the AE activity for SNR-thresholds 2 and 5 are shown in figure C.1 - C.4. Therefore, these SNR-thresholds are not recommended to make observations from the contamination test results.

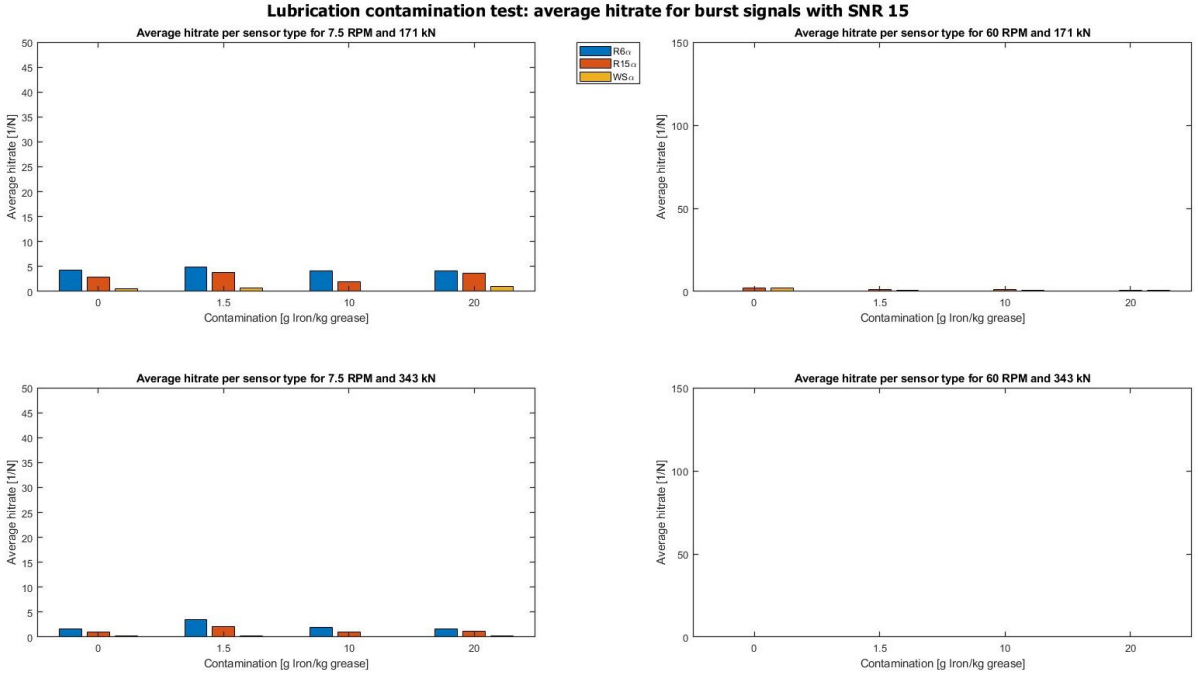

Figure 5.15: Lubrication contamination test: hitrates of burst type signals for SNR-threshold 15

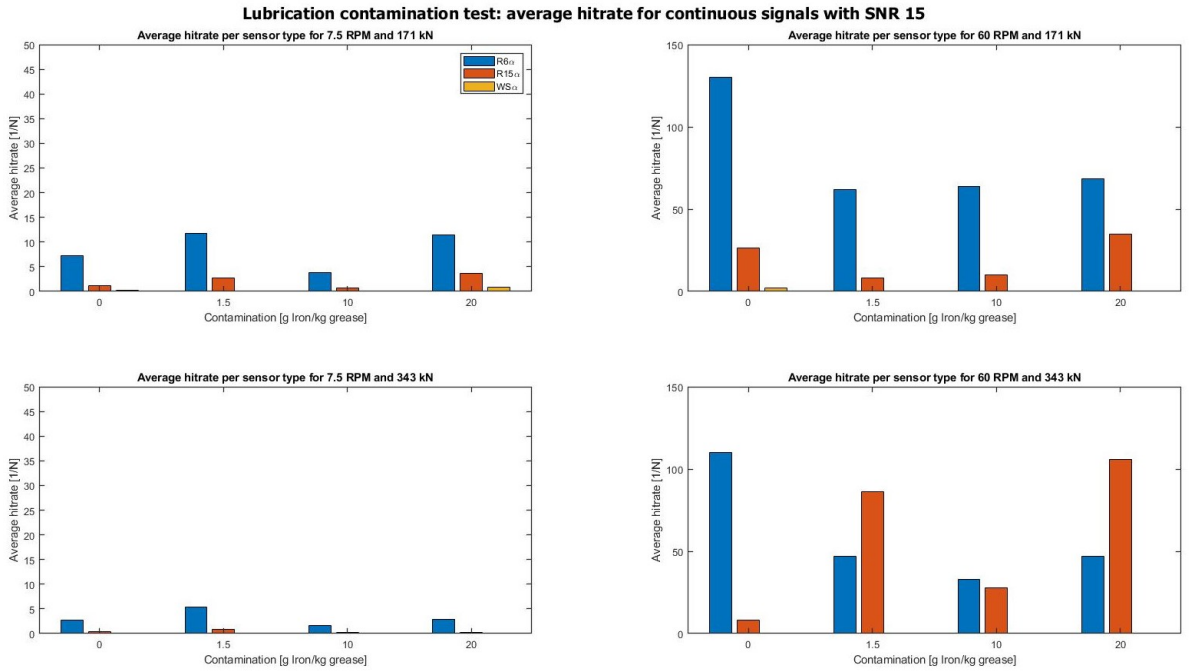

Figure 5.16: Lubrication contamination test: hitrates of continuous type signals for SNR-threshold 15

Observations: Lubrication contamination test

- **General** - From the mid-frequency waves (R15α - sensor), an increase in hit-rate with higher contamination levels is observed for most of the test cases from the raw signals (SNR-threshold 0).
- **Effect of speed**
  - For 60 RPM, an increase in hit-rate of mid-frequency waves (R15α) with respect to higher contamination level was observed, especially in the load case of 343 kN. Furthermore, the hit-rates are higher relative to the 7.5 RPM speed level.
  - For 7.5 RPM, a slight increase in AE activity from the burst waves is observed for contaminated lubricant, however this increased activity is not as evident as for 60 RPM. Furthermore, in general the hit-rates are lower relative to the 60 RPM speed level.
- **Effect of load** - At a load of 171 kN as well as 343 kN, the same increased observation in hit-rate with respect to higher contamination level was observed.
- **Visual inspection and influence of particles** - From visual inspection, it was not visible that wear was developed in the bearing parts, see figures in appendix. Therefore burst waves characteristic for damage development were probably not emitted. The iron particles used were relatively soft particles in comparison with contaminated particles used in other studies. The hardness was not quantified by the manufacturer and was the only supplier of this specific particle size. Since these particles were soft, no clear increasing trend in burst waves characteristic to damage development were observed with higher contamination levels. The soft particles in the lubricant induces more rubbing and friction between the roller and raceway which results in a increased raw AE activity.

From the observations, an answer on the research question posed in the beginning of this section and an answer on the sub-research question posed in the knowledge gap can be provided. An increased AE activity from the mid-frequency waves (R15α) is observed for contamination levels in comparison with clean grease. Furthermore, in most of the test cases it is observed that higher contamination levels result in higher AE activity of mid-frequency content. For higher speeds the AE activity is higher than in lower speeds. The AE activity at lower frequencies originates from rubbing and frictional effects between the rollers and raceway due to the soft iron particles. With these observations, the research question *What is the influence of contaminated lubricant on the emission of AE signals in highly-loaded low-speed roller bearings* is answered.

Comparing the results of the AE activity for burst and continuous waves at a SNR-threshold of 15, it becomes clear that for 60 RPM no burst waves are emitted. From the duration test, a hit-rate of 2 hits/cycle for burst waves with a notable SNR-threshold of 15 were defined as a risk level for the bearing at 60 RPM. For 7.5 RPM and a SNR-threshold of 15, still some AE activity of burst waves is observed which may mask the AE signals from early stages of rolling contact fatigue. However, by increasing the SNR-threshold for this speed level it is expected that nearly no emission of burst wave will occur and clearer observations of contaminated lubricant can be made. The reason for this is that the peak amplitudes of the emitted waveforms due to contaminated lubricant are lower in comparison with the peak amplitudes of the waves emitted due to rolling contact fatigue. Therefore, there is no major masking effect of AE activity due to contaminated lubricant while rolling contact fatigue is developing.

Chapter 6

Conclusion and recommendation

6.1 Conclusion

This research focused on the following two main research questions,

> *1. How can Acoustic Emission be applied to assess the damage of highly-loaded slow-speed roller bearings*?

> *2. What is the influence of contaminated lubricant on the emission of AE signals in highly-loaded low-speed roller bearings?*

of which a summary of the conclusion is provided in relation to the research subquestions.

Damage assessment of highly-loaded low-speed roller bearings with AE

The objective of the first part of this research was to investigate the applicability of AE for the damage assessment in highly-loaded low-speed roller bearings. Condition monitoring of highly-loaded low-speed bearings can detect possible defects and warn machine operators to prevent failure of the bearing which could result in severe consequences. Highly-loaded low-speed roller bearings are frequently used in the offshore industry, e.g. turret bearings in FPSO's, slew-bearings in cranes and windturbines, and sheave bearings. From the analysis in the knowledge gap, it became evident that very limited research was performed on very low speed bearings (<10 RPM) with naturally developed damage. In these limited studies, the size and applied load of the bearings were relatively small in comparison with the commonly applied bearings in the offshore industry.

To investigate how AE can be applied to assess the damage in highly-loaded low-speed bearings, a full scale laboratory experiment has been performed in an existing test set-up. A 400 mm outer diameter roller bearing used as a wheel in the TLS of Allseas's Pioneering Spirit was used as test specimen. It consisted of naturally developed damage due to overloading. In this full-scale laboratory experiment, a duration test on the bearing was performed with the aim to fully consume its L_{10} lifetime while measuring the AE activity. A baseline test was performed to investigate the AE activity on an undamaged bearing to define a safe limit for the AE activity. Another test while loading the worn side of the inner ring was performed to investigate the AE activity in case the bearing contains damage. The measurements are performed with the AMSY-6 measurement system with a measureable frequency range of 40 kHz - 580 kHz with the 3 different types of sensors attached to the inner ring.

The AE activity is expressed in hit-rates. From the results of the baseline test, it can be concluded that a hit-rate of 1 hit/cycle is a safe level for heavy-loaded low-speed bearings. From the results of the test on the worn side of the inner ring, it can be concluded that loading a worn side (without developing damage) does not result in an increased hit-rate with respect to the baseline test. From the duration test,

an increased hit-rate with respect to the number of cycles and L_{10} lifetime is observed. Furthermore, it became evident that wear development occured after performing visual inspection of the bearing parts and lubrication analysis. The increase in hit-rate is related to the developed wear.
This research suggests that acoustic emission monitoring can be applied on highly-loaded low-speed bearings to assess the damage for representative operational conditions.

Influence of contaminated lubricant on AE signals in highly-loaded low-speed roller bearings

The objective of the second part of the research was to investigate the influence of contaminated lubricant with steel particles on AE signals and its possible masking effect during the detection of failure due to rolling contact fatigue. By understanding the influence of contaminated lubricant on acoustic emission, it can be possible to provide a real-time indication of the contamination level by wear debris and it can function as an addition to lubrication analysis.

Lubricant contaminated with 10 μm Iron particles with three representative contamination levels were tested in the same test set up and same type of bearing. As a reference, a test with clean grease is also performed.

An increased AE activity of mid-frequency waves (R15α) with respect to higher contamination levels were observed from the raw signals. The AE activity originates mainly from rubbing and frictional effects between the rollers and raceway due to the soft iron particles. For 60 RPM, nearly no emission of burst waves are observed with the contaminated grease so it does not mask the detection of failure due to rolling contact fatigue during the duration test. For 7.5 RPM, SNR-thresholds higher than 15 can mitigate the masking effect in the detection of failure due to rolling contact fatigue.

So, this research suggests that contaminated lubricant influences the AE activity and indicates that detection of lubricant contamination is possible. Furthermore with a proper choice of the SNR-level, there is no major masking effect of AE by contaminated lubricant while detecting rolling contact fatigue.

6.2 Recommendations

The original plan was to perform the duration test until the bearing would fully consume its L_{10} lifetime. However, due to failure of the 2 components in the test set up and delay in planning it was not possible to finish it. It is recommended to proceed with the test and to let the bearing fully consume its L_{10} lifetime while measuring the AE activity. More knowledge of the relation between hit-rates, wear development and the bearing lifetime will be gained.

More interventions are recommended to relate the AE activity to the results of visual inspection and grease analysis, especially when a sudden increase in hit-rates are observed. However, interventions are highly time consuming so a good balance needs to be made.

Since the average speed of highly-loaded low-speed bearings in the offshore industry is 7.5 RPM, it is recommended to perform future test on this speed. More representative AE activity will be obtained. However reducing the speed leads to more time needed to reach a specified number of cycles and so extends the timeline of the experiment. Furthermore, the electric motor is not suitable to perform the test on this speed level. Replacing the motor is an option.

Dependent on the applicability of the bearings, starting and stopping motion frequently occur during operations. In this experiment, the bearing was continuously rotating with some break times of the motor. It is also recommended to perform tests with starting and stopping motion of the bearing. More understanding of the AE activity will be obtained during this motion.

Influence of contamination on the emission of AE signals

It is recommended to perform the same lubrication contamination test with particles with a hardness comparable with the hardness of the bearing material. This will result in a more representative situation. In the test, soft particles with an unknown hardness were used since manufacturing steel particles of 10 μm of a comparable hardness as the bearing material was too challenging within the scope of this research.

Further, clustering and analysis of the waveforms measured during the contamination test, can result in new findings in how contaminated lubricant and its concentration can be detected and how it can be distinguished from another degradation mechanisms such as rolling contact fatigue.

References

[1] F. Wang, C. Liu, W. Su, Z. Xue, H. Li, and Q. Han. “Condition monitoring and fault diagnosis methods for low-speed and heavy-load slewing bearings: A literature review”. In: *Journal of Vibroengineering* 19 (2017), pp. 3429–3444. DOI: 10.21595/jve.2017.18454.

[2] H.D.M. De Azevedo, A.M. Araujo, and N. Bouchonneau. “A review of wind turbine bearing condition monitoring: State of the art and challenges”. In: *Renewable and Sustainable Energy Reviews* 56 (2016), pp. 368–379. DOI: 10.1016/j.rser.2015.11.032.

[3] S. Glodež, R. Potočnik, and J. Flašker. “Computational model for calculation of static capacity and lifetime of large slewing bearing’s raceway”. In: *Mechanism and Machine Theory* 47 (2012), pp. 16–30.

[4] M.M. Alamdari, T. Rakotoarivelo, and N.L.D. Khoa. “A spectral-based clustering for structural health monitoring based on adaptive kernel spectral clustering”. In: *Mechanical Systems and Signal Processing* 87 (2017), pp. 384–400.

[5] R. Langone, E. Reynders, S. Mehrkanoon, and Suykens J.A.K. “Automated structural health monitoring based on adaptive kernel spectral clustering”. In: *Mechanical Systems and Signal Processing* 90 (2017), pp. 64–78.

[6] S. Sharma and D. Mahto. “Condition Monitoring of Wind Turbines: A Review”. In: *International Journal of Scientific Engineering Research* 4 (2013).

[7] W.X. Yang, P.J. Tavner, C.J. Crabtree, and M. Wilkinson. “Cost Effective Condition Monitoring For Wind Turbine”. In: *IEE Transactions on Industrial Electronics* 57 (2010).

[8] W. Caesarendra, B. Kosasih, A.K. Tieu, H. Zhu, C.A.S. Moodie, and Q. Zhu. “Acoustic emission-based condition monitoring methods: Review and application for low speed slew bearing”. In: *Mechanical Systems and Signal Processing* 72-73.2 (2016), pp. 134–159. DOI: http://dx.doi.org/10.1016/j.ymssp.2015.10.020.

[9] B. Scheeren and L. Pahlavan. *HiTeAM - High Tech Acoustic Monitoring, Phase 1 report*. TU Delft, 2019.

[10] B. Scheeren, A. Huijer, F. Riccioli, N.P. Thakoerdajal, and L. Pahlavan. *HiTeAM - High Tech Acoustic Monitoring, Phase 2 report*. TU Delft, 2021.

[11] G. Zhang, M.Y. Li, C. Sun, J. Zhang, and Zhang H.L. “Load distribution of cross-roller slewing bearing”. In: *Applied Mechanics and Materials* 224 (2012), pp. 268–271.

[12] M. Forsthoffer. *Forsthoffer’s Component Condition Monitoring*. Butterworth-Heinemann, 2019. DOI: https://doi.org/10.1016/B978-0-12-809599-7.00004-X.

[13] *Slew Bearings*. SKF Group, 2017. URL: https://www.skf.com/binaries/pub12/Images/0901d196809590fe-Slewing-bearings_tcm_12-513670.pdf.

[14] Y. Li, X. Wu, and Z. Yang. “A Review of Recent Advances in Wind Turbine Condition Monitoring and Fault Diagnosis”. In: *IEEE Power Electron. Mach. Wind Appli. PEMWA* (2009). DOI: 10.1016/j.triboint.2009.04.033.

[15] B. Jerman, P. Podrzaj, and J. Kramar. “An investigation of slewing-crane dynamics during slewing motion-development and verification of a mathematical model”. In: *International Journal of Mechanical Sciences* 46 (2004), pp. 726–750.

[16] A. Maczynski and S. Wojchiech. “Dynamics of a mobile crane and optimization of the slewing motion of its upper structure”. In: *Nonlinear Dynamics* 32 (2003), pp. 259–290.

[17] P.G. Nikolakopoulos and A. Zavos. “Slew Bearings Damage Detection using Hilbert Huang Transformation and Acoustic Methods”. In: *Tribology in Industry* 37 (2015), pp. 170–175.

[18] J.J. Fitzgerald. “Large-Diameter Slewing Ring Bearing Storage Methods: Comparisons and Cost-Effectiveness”. In: *AISTech 2012 — The Iron Steel Technology Conference and Exposition* (2013), pp. 1439–1447.

[19] M.F. Moyers and W. Lesyna. “Isocenter characteristics of an external ring proton gantry”. In: *International Journal of Radiation Oncology, Biology, Physics* 30 (2004), pp. 1622–1630.

[20] *Bearing Damage and Failure Analysis*. SKF Group, 2017. URL: https://www.skf.com/binaries/pub12/Images/0901d1968064c148-Bearing-failures---14219_2-EN_tcm_12-297619.pdf.

[21] A. van Beek. *Advanced Engineering Design Lifetime Performance and Reliability*. TU Delft, 2019. ISBN: 978-4-431-55072-3.

[22] J. Halme and P. Andersson. “Rolling contact fatigue and wear fundamentals for rolling bearing diagnostics - state of the art”. In: *Proceedings of the Institution of Mechanical Engineers, Part J: Journal of Engineering Tribology* 224 (2010). DOI: 10.1243/13506501JET656.

[23] *ISO 15243 | Rolling bearings - Damage and failures - Terms, characteristics and causes*. ISO, 2004.

[24] J. Schijve. *Fatigue of Structures and Materials*. Springer, 2009. ISBN: 978-1-4020-6808-9.

[25] K. Johnson. *Contact Mechanics*. Cambridge University Press, Cambridge, UK, 1985.

[26] H. Hertz. “Über die Beriihrung fester elastischer Körper”. In: *Journal für die reine und angewandte Mathematik* 92 (1881), pp. 156–171.

[27] W.E. Littmann. “The mechanism of contact fatigue”. In: *Interdisciplinary approach to the lubrication of concentrated contacts - NASA Special report* 237 (1969).

[28] A.V. Olver. “The mechanism of rolling contact fatigueL: an update”. In: *Proceedings of the Institution of Mechanical Engineers, Part J: Journal of Engineering Tribology* 219 (2005). DOI: 10.1243/135065005X9808.

[29] S. Way. “Pitting due to rolling contact”. In: *Journal of applied mechanics* 57 (1935), A49–A58.

[30] D.F. Cannon and H. Pradier. “Rail rolling contact fatigue research by the European Rail Research Institute”. In: *Wear* 191 (1996), pp. 1–13.

[31] J. Kang, B. Hosseinkhani, and P.E.J. Rivera-Díaz-del-Castillo. “Rolling contact fatigue in bearings: a multiscale overview”. In: *Materials Science and Technology* 28 (2011), pp. 44–49. DOI: 10.1179/174328413X13758854832157.

[32] A. Voskamp and E. Mittemeijer. “Crystallographic preferred orientation induced by cyclic rolling contact loading”. In: *Metallurgical and Materials Transactions A* 27 (1996), pp. 3445–3465.

[33] P. Rycerz, A. Olver, and A. Kadiric. “Propagation of Surface Initiated Rolling Contact Fatigue Cracks in Bearing Steel”. In: *International Journal of Fatigue* 27 (2016). DOI: 10.1016/j.ijfatigue.2016.12.004.

[34] H.A. Spikez. “Wear in rolling contacts”. In: *Wear* 112 (1986), pp. 121–144.

[35] J. Williams. “Wear and wear particles - some fundamentals”. In: *Tribology International* 30 (2005), pp. 863–870.

[36] R. Sayles. “Debris damage in rolling bearings and its effect on fatigue life”. In: *Journal of Tribology* 110 (1988), pp. 26–31.

[37] M.M. Kruschov. “Resistance of metals to wear by abrasion as related to hardness”. In: *Proceedings of conference on lubrication and wear* (1957).

[38] J.T. Burwell and C.D. Strang. “On the empirical law of adhesive wear”. In: *Journal of Applied Physics* 23 (1952).

[39] J.F. Archard and W. Hirst. “The wear of materials under unlubricated conditions”. In: *proceedings of the royal society of london series a* 236 (1956).

[40] J.F. Archard. “Contact and rubbing of flat surfaces,” in: *Journal of Applied Physics* 24 (1953).

[41] J.E. Sague and J.H. Rumbarger. “Design Criteria to Prevent Core Crushing Failure in Large Diameter, Case Hardened, Ball and Roller Bearings”. In: *American Society of Mechanical Engineers* (1977).

[42] T.H. Kim, A.V. Olver, and P.K. Pearson. “Fatigue and Fracture Mechanisms in Large Rolling Element Bearings”. In: *Tribology Transactions* 44 (2004), pp. 583–590. DOI: 10.1080/10402000108982498.

[43] S.J. Lacey. *The Role of Vibration Monitoring in Predictive Maintenance*. Schaeffler Group Industrial, 2017. URL: https://www.schaeffler.com/remotemedien/media/_shared_media/08_media_library/01_publications/schaeffler_2/technicalpaper_1/download_1/the_role_of_vibration_monitoring.pdf.

[44] D. Miljkovic. *Brief Review of Vibration Based Machine Condition Monitoring*. Hrvatska elektroprivreda, 2016.

[45] J.C. Jauregui-Correa and A.A. Lozano Guzman. *Mechanical Vibrations and Condition Monitoring*. Elsevier Inc., 2020. DOI: 10.1016/C2019-0-00474-8.

[46] J.D. Smith. “Vibration monitoring of bearings at low speed”. In: *Tribology International* 15 (1982), pp. 139–144.

[47] H. Alian, S. Konforty, U. Ben-Simon, R. Klein, M. Tur, and J. Bortman. “Bearing fault detection and fault size estimation using fiber-optic sensors”. In: *Mechanical Systems and Signal Processing* 120 (2019), pp. 392–407.

[48] X. Bai, H. Xiao, and L. Zhang. “The Condition Monitoring of Large Slewing Bearing Based on Oil Analysis Method”. In: *Key Engineering Materials* 474-476 (2011), pp. 716–719.

[49] J. Zhu, D. He, and E. Bechhoefer. “Survey of Lubrication Oil Condition Monitoring, Diagnostics, and Prognostics Techniques and Systems”. In: *Journal of Chemical Science and Technology* 2 (2013), pp. 100–115.

[50] T.J. Harvey, R.J.K. Wood, and H.E.G. Powrie. “Electrostatic wear monitoring of rolling element bearings”. In: *Wear* 263 (2007), pp. 1492–1501.

[51] M. Craig, T.J. Harvey, R.J.K. Wood, K. Masuda, M. Kawabata, and H.E.G. Powrie. “Advanced condition monitoring of tapered roller bearings, Part 1”. In: *Tribology International* 42 (2009), pp. 1846–1856.

[52] C. James Li and S.Y. Li. “Acoustic emission analysis for bearing condition monitoring”. In: *Wear* 185.2 (1995), pp. 67–74.

[53] A. Rai and S.H. Upadhyay. “A review on signal processing techniques utilized in the fault diagnosis of rolling element bearings”. In: *Tribology International* 96 (2016), pp. 289–306. DOI: 10.1016/j.triboint.2015.12.037.

[54] I. El-Thalji and E. Jantunen. “A summary of fault modelling and predictive heath monitoring of rolling element bearings”. In: *Mechanical Systems and Signal Processing* 60 (2015), pp. 252–272. DOI: 10.1016/j.ymssp.2015.02.008.

[55] P. Shakya, A.K. Darpe, and M.S. Kulkarni. “Vibration-based fault diagnosis in rolling element bearings: ranking of various time, frequency and time-frequency domain data-based damage identification parameters”. In: *International Journal of Condition Monitoring* 3 (2013).

[56] D. Koulocheris, G. Gyparakis, A. Stathis, and T. Costopoulos. “Vibration Signals and Condition Monitoring for Wind Turbines”. In: *Engineering* 5 (2013). DOI: 10.4236/eng.2013.512116.

[57] S. Kim, S. Pakzad, D. Culler, J. Demmel, G. Fenves, S. Glaser, and M. Turon. “Health monitoring of civil infrastructures using wireless sensor networks”. In: *IPSN 2007: Proceedings of the Sixth International Symposium on Information Processing in Sensor Networks* (2007), pp. 254–263. DOI: 10.1145/1236360.1236395.

[58] H. Saruhan, S. Saridemir, A. Çiçek, and I. Uygur. “Vibration Analysis of Rolling Element Bearings Defects”. In: *Journal of Applied Research and Technology* 12.3 (2016), pp. 384–395. DOI: https://doi.org/10.1016/S1665-6423(14)71620-7.

[59] S.J. Lacey. *An Overview of Bearing Vibration Analysis*. Schaeffler Group Industrial, 2017. URL: https://www.schaeffler.com/remotemedien/media/_shared_media/08_media_library/01_publications/schaeffler_2/technicalpaper_1/download_1/vibration_analysis_en_en.pdf.

[60] X.Y. Zhou and D.F. Luo. "Research of amplitude-frequency domain parameters analysis for condition detection and fault diagnosis". In: *Reseach Journal of Applied Sciences, Engineering and Technology* 4 (2012), pp. 3787–3790.

[61] P. Jayaswal and P. Agrawal. "New Trends in Wind Turbine Condition Monitoring System". In: *International Journal of Emerging Trends Engineering and Development* 3 (2011), pp. 133–148.

[62] P. Borghesani, P. Pennacchi, and S. Chatterton. "The relationship between kurtosis- and envelope-based indexes for the diagnostic of rolling element bearings". In: *Mechanical Systems and Signal Processing* 43 (2014), pp. 25–43. DOI: 10.1088/1757-899X/50/1/012026.11.

[63] N. Waters, P.P. Beaujean, and D.J. Vendittis. "Targeting Faulty Bearings for an Ocean Turbine Dynamometer". In: *International Journal of Prognostic Health Management* 21 (2013).

[64] T. Liu, J. Lee, P. Singh, and G. Liu. "Using acceleration measurements and neuro-fuzzy systems for monitoring and diagnosis of bearings". In: *Proceedings of Society of Photo-Optical Instrumentation Engineers (SPIE)* (2013). DOI: 10.1117/12.2035880.10.

[65] M. Sarvajith, B. Shah, S. Kulkarni, and S. Jana. "Condition Monitoring of Rolling Element Bearing Using Wavelet Transform and Support Vector Machine". In: *Conference: NCCM* (2013).

[66] C.K.E. Nizwan, S.A. Ong, M.F.M. Yusof, and M.Z. Baharom. "A wavelet decomposition analysis of vibration signal for bearing fault detection". In: *IOP Conference Series Materials Science Engineering* 50 (2013). DOI: 10.1088/1757-899X/50/1/012026.11.

[67] H. Sun, G.A. Yang, Q. Chen, A. Palazoglu, and K. Feng. "Fault diagnosis of rolling bearing based on wavelet transform and enveloppe spectrum correlation". In: *Journal of Vibration Control* 19 (2013), pp. 924–941. DOI: 10.1177/1077546311435348.

[68] J.B. Ali, N. Fnaiech, L. Saidi, B. Chebel-Morello, and F. Fnaiech. "Application of empirical mode decomposition and artificial neural network for automatic bearing fault diagnosis based on vibration signals". In: *Applied Acoustics* 89 (2015), pp. 16–27.

[69] B. Ma, J.D. Wu, J. Ma, X.D. Wang, and Y.G. Fan. "Fault Monitoring and Classification Method of Rolling Bearing based on KICA and LSSVM". In: *Advanced Material Research* 6 (2014), pp. 971–980.

[70] M. Unala, M. Onatb, M. Demetgulc, and H. Kucukc. "Fault diagnosis of rolling bearings using a genetic algorithm optimized neural network". In: *Measurement* 58 (2014), pp. 187–196. DOI: 10.1016/j.measurement.2014.08.041.

[71] R. Ziani, R. Zagadi, A. Felkaoui, and M. Djouada. "Bearing Fault Diagnosis Using Neural Network and Genetic Algorithm with the Trace Criterion". In: *Condition Monitoring of Machinery in Non-Stationary Operations* (2012), pp. 89–96.

[72] W. Caesarendra, B. Kosasih, A.K. Tieu, and C.A.S. Moodie. "Application of the largest Lyapunov exponent algorithm for feature extraction in low speed slew bearing condition monitoring". In: *Mechanical System and Signal Processing* 50-51 (2015), pp. 116–138. DOI: 10.1016/j.ymssp.2014.05.033.

[73] K.G. Bøving. *NDE Handbook, Non-Destructive Examination Methods for Condition Monitoring*. Butterworth-Heinemann, 1989. ISBN: 978-0-408-04392-2. DOI: https://doi.org/10.1016/B978-0-408-04392-2.50034-5.

[74] M.C. Isaa, N.H.N. Yusoffa, H. Naina, M.S. Yatia, M.S.D. Yatia, M.M. Muhammada, and I.M. Nor. "Ferrographic analysis of wear particles of various machinery systems of a commercial marine ship". In: *Procedia Engineering* 68 (2013), pp. 345–351.

[75] Q.H. Fan and W. Han. "The application of the ferrographic analysis technology in hydraulic system fault analysis for aircraft". In: *Chinese Hydraulics and Pneumatics* 5 (2007), pp. 59–61.

[76] R.X. Qin, L. Bian, and H.L. Zhang. "The application research of ferrograph analysis in marine diesel engine". In: *China Shiprepair* 28 (2015), pp. 36–39.

[77] H.J. Wei, Z.H. Wang, P.T. Sun, H.L. Yu, D.L. Guan, Q.C. Hu, and F. Yin. “Study on the characteristic parameter of oil spectrometric analysis”. In: *Spectroscopy and Spectral Analysis* 25 (2005), pp. 1125–1127.

[78] H.W. Wang, G. Chen, L.B. Chen, K. Song, and A. Li. “A fault monitoring technique for wear of aero-engine rolling bearing”. In: *Journal of Aerospace Power* 29 (2014), pp. 2256–2263.

[79] X. Jiang, F. Liu, and P. Zhao. “Failure Analysis of Rolling Bearing Based on Oil Monitoring Techniques with Mechanics Basis”. In: *Applied Mechanics and Materials* 164 (2012), pp. 401–404. DOI: 10.4028/www.sciencedirect.net/AMM.164.401.

[80] X. Jiang, F. Liu, and P. Zhao. “Gearbox Non-ferrous Metal Bearing Wear Condition Monitoring Based on Oil Analysis”. In: *Applied Mechanics and Materials* 164 (2012), pp. 73–76. DOI: 10.4028/www.sciencedirect.net/AMM.164.73.

[81] P.P. Kherche and S.V. Kshirsagar. “Review of Fault Detection in Rolling Element Bearing”. In: *International Journal of Innovative Research in Advanced Engineering* 1 (2014).

[82] M.S. Weng, S.E. Dunn, W.H. Hartt, and R.P. Brown. “Application of Acoustic Emission to Detection of Reinforcing Steel Corrosion in Concrete”. In: *Corrosion* 38 (1982), pp. 9–14. DOI: 10.5006/1.3577322.

[83] Z. Nazarchuk, V. Skalskyi, and O. Serhiyenko. *Acoustic Emission Methodology and Application*. Springer, 2017. ISBN: 978-3-319-49350-3.

[84] S. Masmoudi, A. El Mahi, and S. Turki. “Use of piezoelectric as acoustic emission sensor for in situ monitoring of composite structures”. In: *Composites Part B* 80 (2015), pp. 307–320. DOI: 10.1016/j.compositesb.2015.06.003.

[85] A. Huijer, C. Kassapoglou, and L. Pahlavan. “Acoustic emission monitoring of carbon fibre reinforced composites with embedded sensors for in-situ damage identification”. In: *Sensors* 21 (2021), pp. 522–529. DOI: 10.3390/s21206926.

[86] C. Van Steen, L. Pahlavan, M. Wevers, and E. Verstrynge. “Localisation and characterisation of corrosion damage in reinforced concrete by means of acoustic emission and X-ray computed tomography”. In: *Construction and Building Materials* 197 (2019), pp. 21–29. DOI: 10.1016/j.conbuildmat.2018.11.159.

[87] The Japanese Society for Non-Destructive Testing. *Slew Bearings*. Springer, 2016. ISBN: 978-4-431-55072-3. DOI: https://doi.org/10.1007/978-4-431-55072-3.

[88] *AMSY-6 System Description*. 2017.

[89] S. Al-Dossary, R.I.R. Hamzah, and D. Mba. “Observations of changes in acoustic emission waveform for varying seeded defect sizes in a rolling element bearing”. In: *Applied Acoustics* 70 (2009), pp. 58–81. DOI: 10.1016/j.apacoust.2008.01.005.

[90] B. Scheeren, M.L. Kaminski, and L. Pahlavan. “Evaluation of Ultrasonic Stress Wave Transmission in Cylindrical Roller Bearings for Acoustic Emission Condition Monitoring”. In: *Sensors* (2022).

[91] B. Scheeren, L. Pahlavan, and M.L. Kaminski. “Condition Assessment of Highly-loaded Low-speed Bearings Using Acoustic Emission Monitoring: A Feasibility Study”. In: *IAES* (2018).

[92] H.L. Balderston. “The Detection of Incipient Failure in Bearings”. In: *Materials Evaluation* 27 (1969), pp. 121–128.

[93] L.M. Rogers. “The application of vibration signature analysis and acoustic emission source location to on-line condition monitoring of anti-friction bearings”. In: *Tribology International* 12 (1979), pp. 51–58. DOI: 10.1016/0301-679X(79)90001-X.

[94] N. Tandon and B.C. Nakra. “Comparison of vibration and acoustic measurement techniques for the condition monitoring of rolling element bearings”. In: *Tribology International* 25 (1992), pp. 205–212. DOI: 10.1016/0301-679X(92)90050-W.

[95] M.W. Hawman and W.S. Galinaitis. “Acoustic emission monitoring of roller element bearings”. In: *International Ultrasonic Symposium Proceedings* 2 (1988), pp. 885–889. DOI: 10.1109/ultsym.1988.49503.

[96] A.M. Al-Ghamd and D. Mba. “A comparative experimental study on the use of acoustic emission and vibration analysis for bearing defect identification and estimation of defect size”. In: *Mechanical System and Signal Processing* 20 (2006), pp. 1537–1571. DOI: 10.1016/j.ymssp.2004.10.013.

[97] D. Cornal, F.G. Guzman, G. Jacobs, and S. Neumann. “Acoustic Response of ROller Bearings Under Critical Operating Conditions”. In: *Lecture Notes Mechanical Engineering* (2020), pp. 740–749. DOI: 10.1007/978-3-030-48021-9_82.

[98] K. Nienhaus, F.D. Boos, K. Garate, and R. Baltes. “Development of Acoustic Emission based defect parameters for slow rotating roller bearings”. In: *Proceedings of the 25th International Congress on Condition Monitoring and Diagnostic Engineering* 364 (2012). DOI: 10.1088/1742-6596/364/1/012034.

[99] C. Riuz-Carcel, E. Hernani-Ros, Y. Cao, and D. Mba. “Use of spectral kurtosis for improving signal to noise ratio of acoustic emission signal from defective bearings”. In: *Journal of Failure Analysis and Prevention* 14 (2014), pp. 363–371. DOI: 10.1007/s11668-014-9805-7.

[100] Y. He, X. Zhang, and M.I. Friswell. “Defect diagnosis for rolling element bearings using acoustic emission”. In: *Journal of Vibration and Acoustics-Transactions of the ASME* 131 (2009), pp. 0610121–06101210. DOI: 10.1115/1.4000480.

[101] D. Mba, R.H. Bannister, and G.E. Findlay. “Condition monitoring of low-speed rotating machinery using stress waves Part 1”. In: *Proceedings of the Institution of Mechanical Engineers, Part E: Journal of Process Mechanical Engineering* 213 (1999), pp. 153–170. DOI: 10.1243/0954408991529906.

[102] J. Miettinen and P. Pataniitty. “Acoustic emission in monitoring extremely slowly rotating rolling bearing”. In: *Proceedings of COMADEM* (1999), pp. 289–297.

[103] D. Mba, R.H. Bannister, and G.E. Findlay. “Condition monitoring of low-speed rotating machinery using stress waves: Part 2”. In: *Proceedings of the Institution of Mechanical Engineers, Part E: Journal of Process Mechanical Engineering* 213 (1999), pp. 171–185. DOI: 10.1243/0954408991529915.

[104] N. Jamaludin, D. Mba, and R.H. Bannister. “Condition monitoring of slow-speed rolling element bearings using stress waves”. In: *Proceedings of the Institution of Mechanical Engineers, Part E: Journal of Process Mechanical Engineering* 215 (2001), pp. 245–271. DOI: 10.1243/0954408011530488.

[105] A. Nair and C.S. Cai. “Acoustic Emission Monitoring of Bridges: Review and case studies”. In: *Engineering Structures* 32 (2010), pp. 1704–1714. DOI: 10.1016/j.engstruct.2010.02.020.

[106] K.M. Holford, A.W. Davies, R. Pullin, and D.C. Carter. “Damage location in steel bridges by acoustic emission”. In: *journal of Intelligent Material Systems and Structures* 12 (2001), pp. 567–576. DOI: 10.1106/KDNY-AJ0U-KP2B-P52R.

[107] J. Yu, P. Ziehl, B. Zrate, and J. Caicedo. “Prediction of fatigue crack growth in steel bridge components using acoustic emission”. In: *Journal of Constructional Steel Research* 67 (2011), pp. 1254–1260. DOI: 10.1016/j.jcsr.2011.03.005.

[108] K. Ohno and M. Ohtsu. “Crack classification in concrete based on acoustic emission”. In: *Construction and Building Materials* 24 (2010), pp. 2339–2346. DOI: 10.1016/j.conbuildmat.2010.05.004.

[109] D.G. Aggelis. “Classification of cracking mode in concrete by acoustic emission parameters”. In: *Mechanics Research Communications* 38 (2011), pp. 153–157. DOI: 10.1016/j.mechrescom.2011.03.007.

[110] F. Zhang, L. Pahlavan, and Y. Yang. “Evaluation of acoustic emission source localization accuracy in concrete structures”. In: *Structural Health Monitoring* 19 (2020), pp. 2063–2074. DOI: 10.1177/1475921720915625.

[111] T. Loutas, N. Eleftheroglou, and D. Zarouchas. “A data-driven probabilistic framework towards the in-situ prognostics of fatigue life of composites based on acoustic emission data”. In: *Composite Structures* 161 (2017), pp. 522–529. DOI: 10.1016/j.compstruct.2016.10.109.

[112] V. Giurgiutiu, A. Zagrai, and J. Bao. “Damage identification in aging aircraft structures with piezoelectric wafer active sensors”. In: *Journal of Intellectual Materials Systems and Structures* 15 (2004), pp. 673–687. DOI: 10.1177/1045389X04038051.

[113] F. Hemmati, M. Miraskari, and M.S. Gadala. “Application of wavelet packet transform in roller bearing fault detection and life estimation”. In: *Journal of Physics: Conference Series* 1074 (2018). DOI: 10.1088/1742-6596/1074/1/012142.

[114] B. Kilindu, X. Chiementin, J. Duez, and D. Mba. “Cyclostationarity of Acoustic Emission for monitoring bearing defects”. In: *Mechanical Systems and Signal Processing* 25 (2011), pp. 2061–2072. DOI: 10.1016/j.ymssp.2011.01.020.

[115] A.A. Azeez, M. Alkhedher, M.S. Gadala, and O.A. Mohamad. “Fault detection of rolling element bearings using advanced signal processing technique”. In: *Advances in Science Technology and Engineering Systems Conference ASET 2020* (2020). DOI: 10.1109/ASET48392.2020.9118398.

[116] F. Hemmati, W. Orfali, and M.S. Gadala. “Roller bearing acoustic signature extraction by wavelet packet transform, applications in fault detection and size estimation”. In: *Applied Acoustics* 104 (2016), pp. 101–118. DOI: 10.1016/j.apacoust.2015.11.003.

[117] D. Mba. “The use of acoustic emission for estimation of bearing defect size”. In: *Journal of Failure Analysis and Pervention* 8 (2008), pp. 188–192. DOI: 10.1007/s11668-008-9119-8.

[118] G. Li, Y. Jiao, and Z. Wu. “Defect Diagnosis of Low-Speed Heavy-Duty Bearings Using Acoustic Emission”. In: *Springer Proceedings Physics* 218 (2017), pp. 249–257. DOI: 10.1007/978-3-030-12111-2_23.

[119] F. Guo, S. Shen, Z. Duan, Z. Fan, and Z. Sun. “Acoustic Emission Fault Diagnosis Of Rolling Bearing Based on Discrete Hidden Markov Model”. In: *Springer Proceedings Physics* 218 (2017), pp. 379–386. DOI: 10.1007/978-3-030-12111-2_35.

[120] M.T. Pham, J.-M. Kim, and C.H. Kim. “Efficient Fault Diagnosis of Rolling Bearings Using Neural Network Architecture Search and Sharing Weights”. In: *IEEE Access* 9 (2021), pp. 98800–98811. DOI: 10.1109/ACCESS.2021.3096036.

[121] F. Konig, C. Sous, A. Ouald Chaib, and G. Jacobs. “Machine learning based anomaly detection and classification of acoustic emission events for wear monitoring in sliding bearing systems”. In: *Tribology International* 155 (2021). DOI: 10.1016/j.triboint.2020.106811.

[122] J. Miettinen and P. Andersson. “Acoustic emission of rolling bearings lubricated with contaminated grease”. In: *Tribology International* 33 (2000), pp. 777–787.

[123] K. Jiang, L. Han, and Y. Zhou. “Quantitative evaluation of the impurity content of grease for low-speed heavy-duty bearing using an acoustic emission technique”. In: *Measurement and Control* 52.7-8 (2019), pp. 1159–1166. DOI: https://doi.org/10.1177/0020294019858214.

[124] M. Naciri and M. Chitrapu. “Turret-Moored FPSO Yaw Motions in a Squall-Prone Region”. In: *Offshore Technology Conference* (2019).

[125] *Pioneering spirit*. 2018. URL: https://allseas.com/equipment/pioneering-spirit/ (visited on 03/12/2021).

[126] *Damage analysis - TLS wheels*. Allseas, Apr. 11, 2017.

[127] *Bogie Wheel Roller Bearing - Engineering Drawing | PI-322V5-500-M-N-013*. Feb. 23, 2011.

[128] *Quenched and Tempered steel 42CrMo4 - Wheels TLS for PS*. Galperti Tech, Mar. 30, 2011.

[129] *Abrasion Resistant Steel - Quard 400*. NLMK - Clabecq.

[130] *ISO 281 | Rolling bearings - Dynamic load ratings and rating life*. ISO, 2004.

[131] *Pioneering Spirit - Topside Lift System - Roller bearings static load rating*. Allseas, Apr. 20, 2017.

[132] L. Yunfeng and J. Lei. “Determination of permissible contact stress of case hardened raceway of roller slewing bearing”. In: *Science Progress* 103 (2020), pp. 1–15. DOI: 10.1177/00368504 20980609.

[133] *Rothe Erde Slewing Bearings - Installation Lubrication Maintenance - Bearing Inspection*. Rothe Erde.

[134] *Grease sampling*. Gulf Marine.

[135] *ASTM D6304 | Standard Test Method for Determination of Water in Petroleum Products, Lubricating Oils, and Additives by Coulometric Karl Fischer Titration*. ASTM, 2020.

[136] *ASTM D6595 | Standard Test Method for Determination of Wear Metals and Contaminants in Used Lubricating Oils or Used Hydraulic Fluids by Rotating Disc Electrode Atomic Emission Spectrometry*. ASTM, 2017.

[137] *ASTM D8184 | Standard Test Method for Ferrous Wear Debris Monitoring in In-Service Fluids Using a Particle Quantifier Instrument*. ASTM, 2018.

Appendix A

Pictures of bearing parts and failures test set up

In this part of the appendix, pictures during visual inspections of the parts of the bearing are provided. Furthermore, pictures of the failed components during testing are provided as well.

A.1 Pictures visual inspection during baseline test

In figure A.1 randomly picked rollers from each raceway are presented. The written letters in green is a symbol for from which raceway the roller originates.

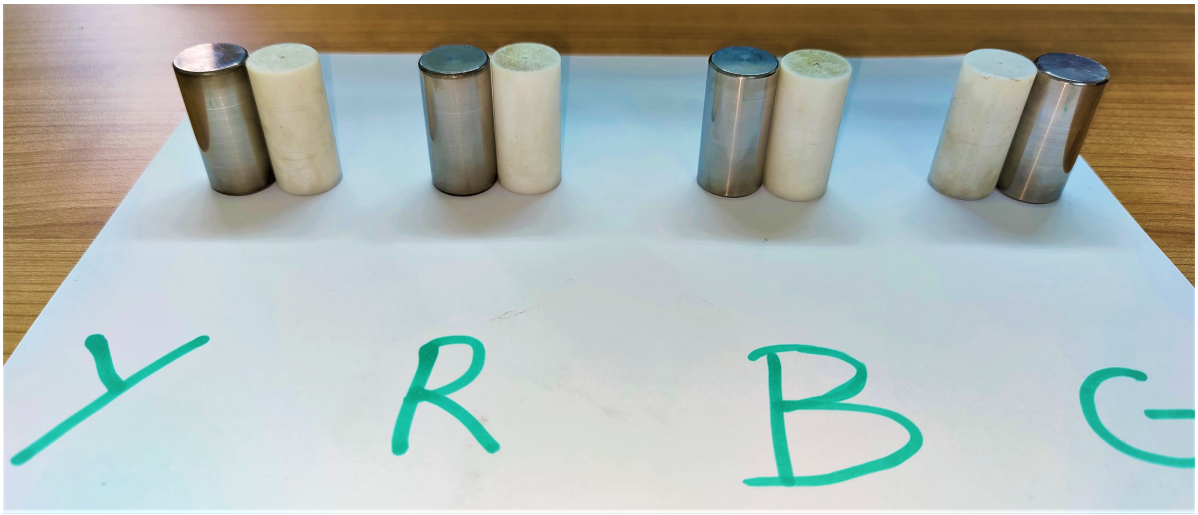

Figure A.1: Rollers after first intervention per raceway, from left to right taken as reference from figure 4.25

Figure A.2: Rollers from first raceway

Figure A.3: Rollers from second raceway

Figure A.4: Rollers from third raceway

Figure A.5: Rollers from fourth raceway

Figure A.6: Outer ring first picture

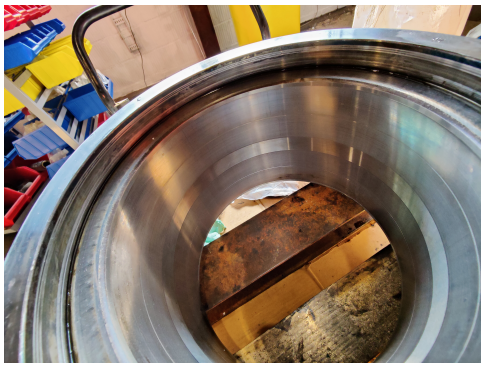

Figure A.7: Outer ring second picture

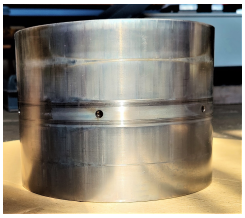

Figure A.8: Inner ring worn side, taken as reference, 0 degrees

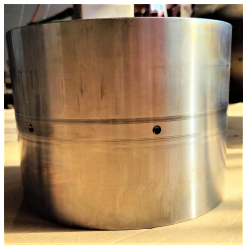

Figure A.9: Inner ring, 90 degrees rotated from A.8

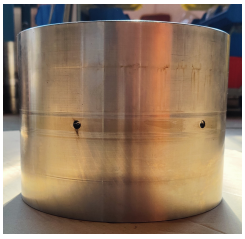

Figure A.10: Inner ring, 180 degrees rotated

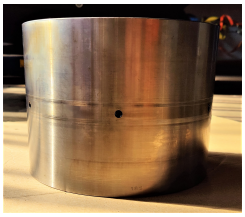

Figure A.11: Inner ring, 270 degrees rotated

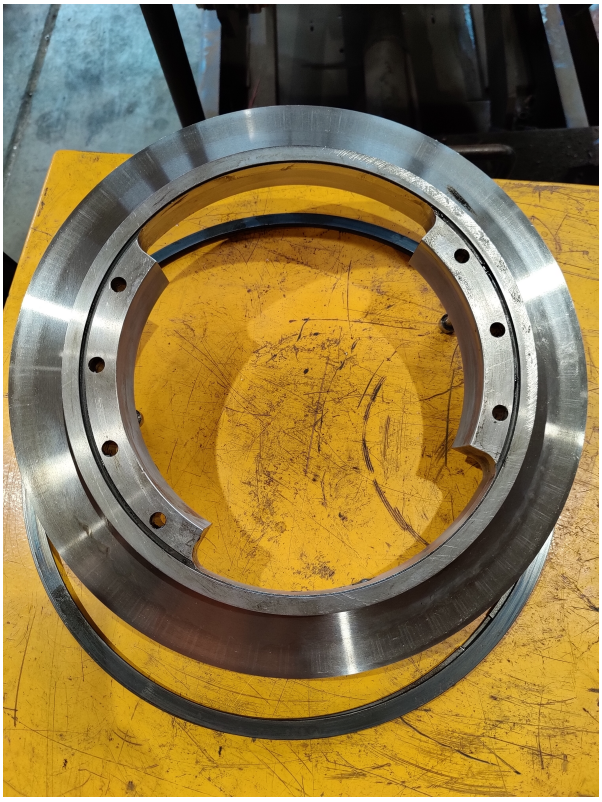

Figure A.12: One of the flanges

A.1.1 Dye penetrant test during baseline test

A dye penetrant test was performed on the inner and outer ring during the baseline test, to identify the presence of cracks. The red marks will be visible in case cracks with a minimum width of 0.01 mm is present. From the pictures A.13 - A.17 it can be observed that no red marks are visible, except at the grease holes on the inner ring. During application and cleaning of the red penetrant fluid, a small amount remained a bit inside the hole. That is the reason why still some red marks are visible. Those marks do not represent cracks.

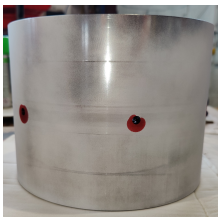

Figure A.13: NDT on Inner ring worn side, taken as reference, 0 degrees

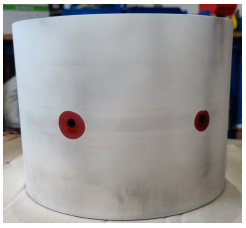

Figure A.14: NDT Inner ring, 90 degrees rotated from A.8

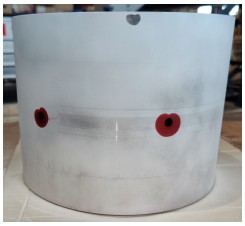

Figure A.15: Inner ring, 180 degrees rotated

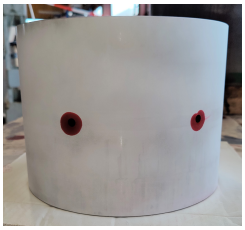

Figure A.16: NDT Inner ring, 270 degrees rotated

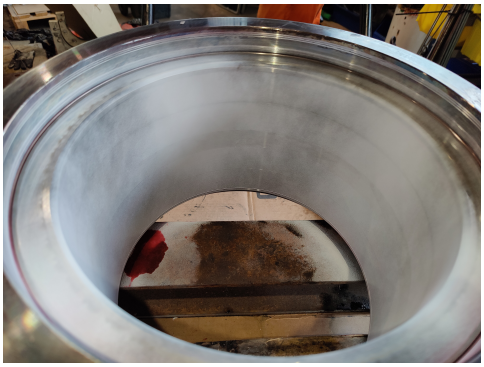

Figure A.17: NDT outer ring

A.2 Visual inspection after duration test

In this section, all pictures of the parts of the bearing after the duration test are provided.

Radial rollers

Figure A.18: Rollers after duration test shown per raceway. Sorted positioning from most left raceway to most right raceway. Directions left and right are taken as reference from figure 4.25.

Figure A.19: Roller from first raceway, after duration test.

Figure A.20: Roller from second raceway, after duration test.

Figure A.21: Roller from third raceway, after duration test.

Figure A.22: Roller from fourth raceway, after duration test.

Outer ring raceways

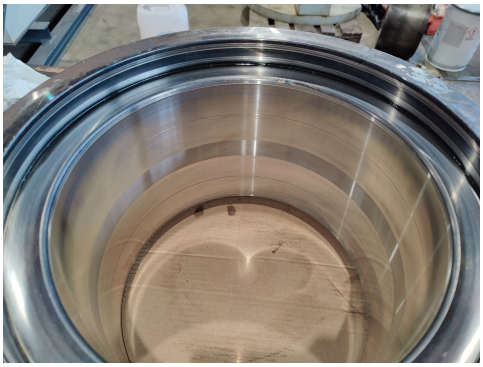

Figure A.23: Outer ring raceways, after duration test

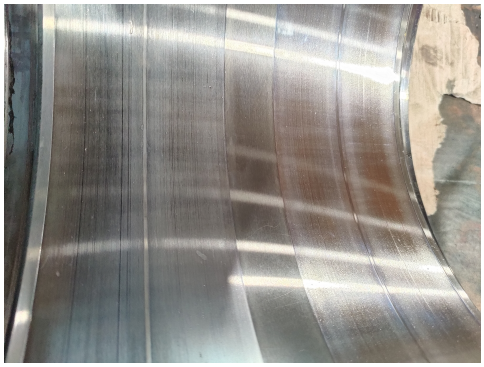

Figure A.24: Outer ring close up picture of developed wear at raceways

Inner ring raceways

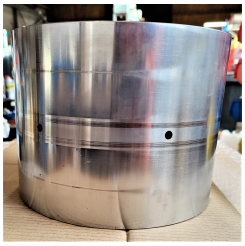

Figure A.25: Inner ring worn side, taken as reference, 0 degrees. After duration test

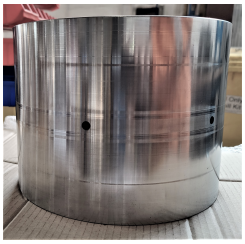

Figure A.26: Inner ring, 90 degrees rotated from A.25

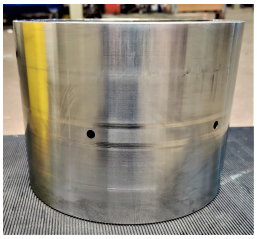

Figure A.27: Inner ring, 180 degrees rotated

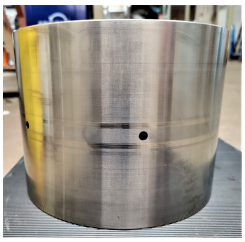

Figure A.28: Inner ring, 270 degrees rotated

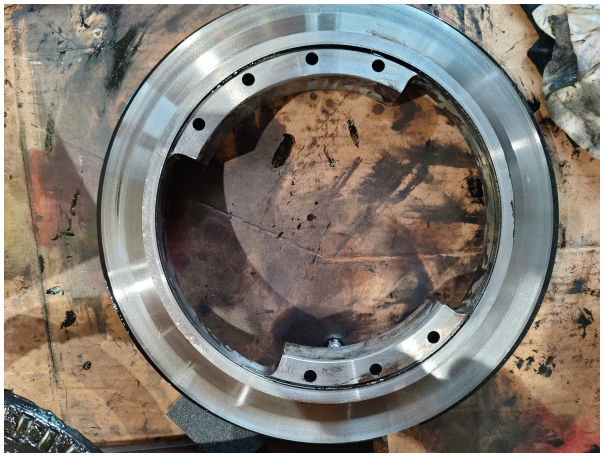

Figure A.29: One of the flanges after duration test

A.2.1 Dye penetrant test after duration test

After the duration test, a dye penetrant test was performed to identify the presence of cracks in the bearing parts. No red marks were visible except at the grease holes. So no cracks were identified, however traces of developed wear are visible which cannot be identified by dye penetrant testing.

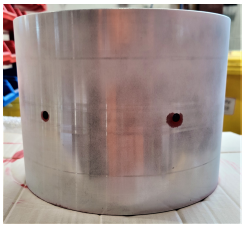

Figure A.30: NDT on Inner ring worn side, taken as reference, 0 degrees

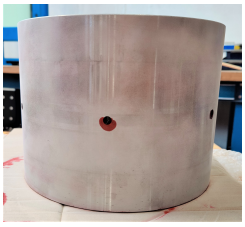

Figure A.31: NDT Inner ring, 90 degrees rotated from A.25

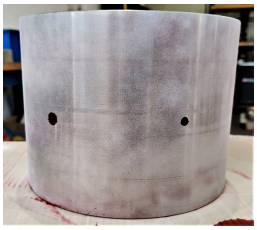

Figure A.32: Inner ring, 180 degrees rotated

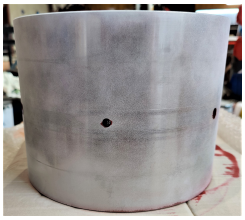

Figure A.33: NDT Inner ring, 270 degrees rotated

Figure A.34: NDT outer ring

A.3 Visual inspection contamination test

Pictures of the bearing before the contamination test started are provided in figures A.35 - A.40.

A.3.1 Pictures bearing before testing

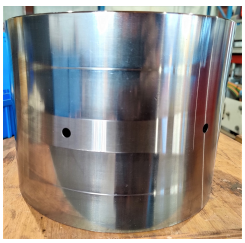

Figure A.35: Worn side of the inner ring taken as reference at 0 degrees. Damage state before contamination test

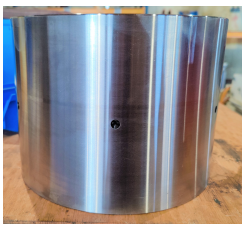

Figure A.36: Inner ring contamination test, 90 degrees rotated from A.35

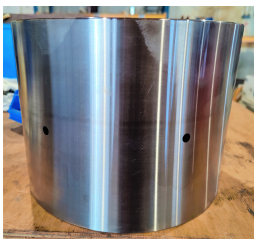

Figure A.37: Inner ring contamination test, 180 degrees rotated from A.35

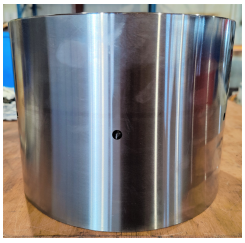

Figure A.38: Inner ring contamination test, 270 degrees rotated from A.35

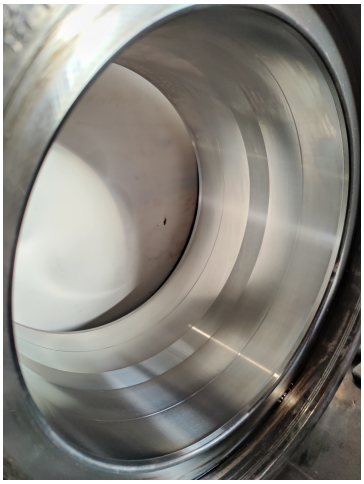

Figure A.39: Outer ring of contamination test; Left view

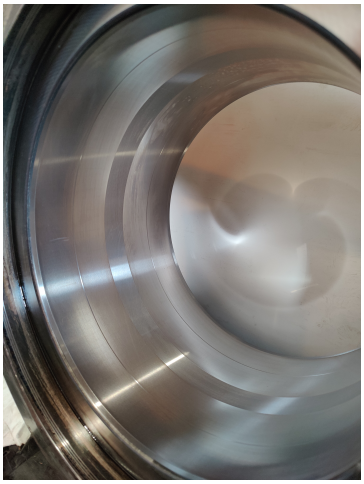

Figure A.40: Outer ring of contamination test; Right view

A.3.2 Pictures bearing after contamination tests

Pictures of the bearing before the contamination test started are provided in figures A.41 - A.46.

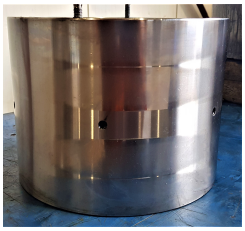

Figure A.41: Worn side of the inner ring taken as reference at 0 degrees. Damage state after contamination test

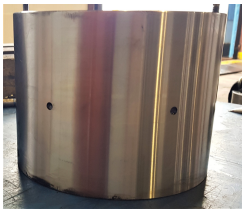

Figure A.42: Inner ring contamination test, 90 degrees rotated from A.41

Figure A.43: Inner ring contamination test, 180 degrees rotated from A.41

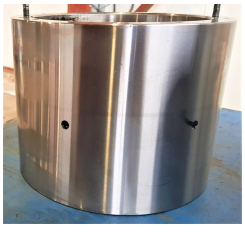

Figure A.44: Inner ring contamination test, 270 degrees rotated from A.41

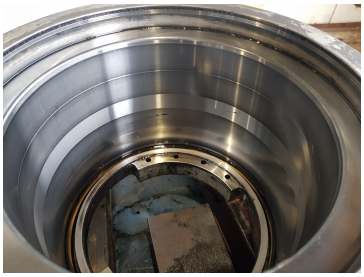

Figure A.45: Outer ring after contamination test; Left view

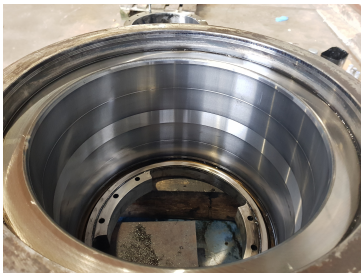

Figure A.46: Outer ring after contamination test; Right view

A.4 Failed components of test set up

Figure A.47: Warped cylinder hinge connection beam

Figure A.48: New design of cylinder hinge connection beam

Figure A.49: Failure of test wheel: welded connection between wheel structure and shaft broken

Figure A.50: New designed test wheel

Appendix B

Appendix B: Results of FEM analyses

B.1 Contact stress of modified test wheel

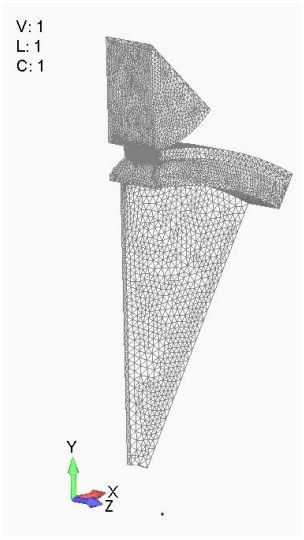

Figure B.1: General model of finite element analysis of contact stress between test wheel en bearing

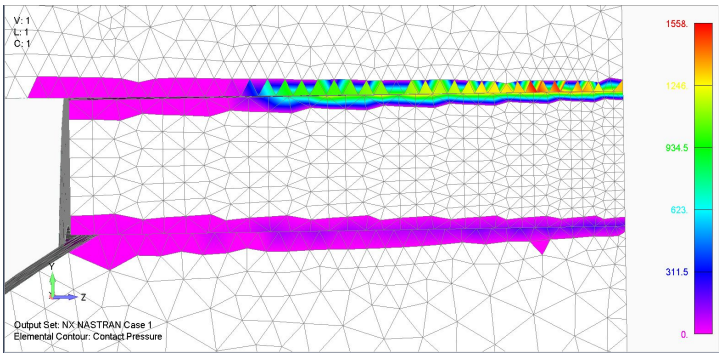

Figure B.2: Results of FEA contact stress between test wheel and bearing

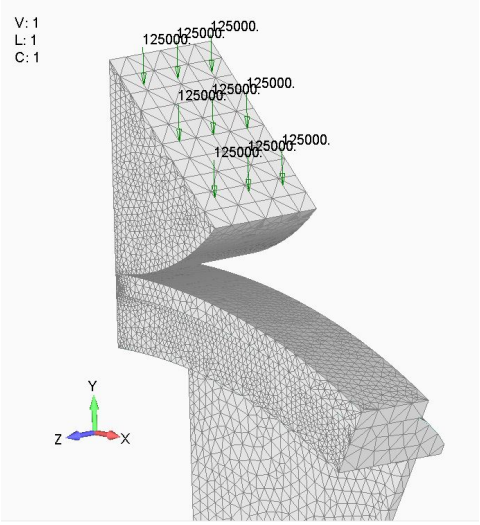

Figure B.3: Location of applied load on FEM model contact stress calculation modified test wheel

In this FEM model, a 10-node tetraeder element was used with a mesh size of 1.33 mm at the contact between the bearing and modified test wheel. A linear elastic model with Young's modulus of 210,000 MPa and poisson ratio of 0.3 was used. A load of 125 kN was applied in negative y-direction as shown on the surface in figure B.3. A maximum load of 500 kN will be exerted on the bearing in the test set up. Since a quarter of the bearing and test wheel is modelled for the sake of computational efficiency, 125 kN applied in the model corresponds to 500 kN for the full model. Translational constraints are applied at the symmetry planes. Contact connections were applied between the contact surface of the bearing and test wheel and between the hardened ring and flattened test wheel with zero friction and only penetration restricted.

B.2 Contact stress of inner ring raceway and roller

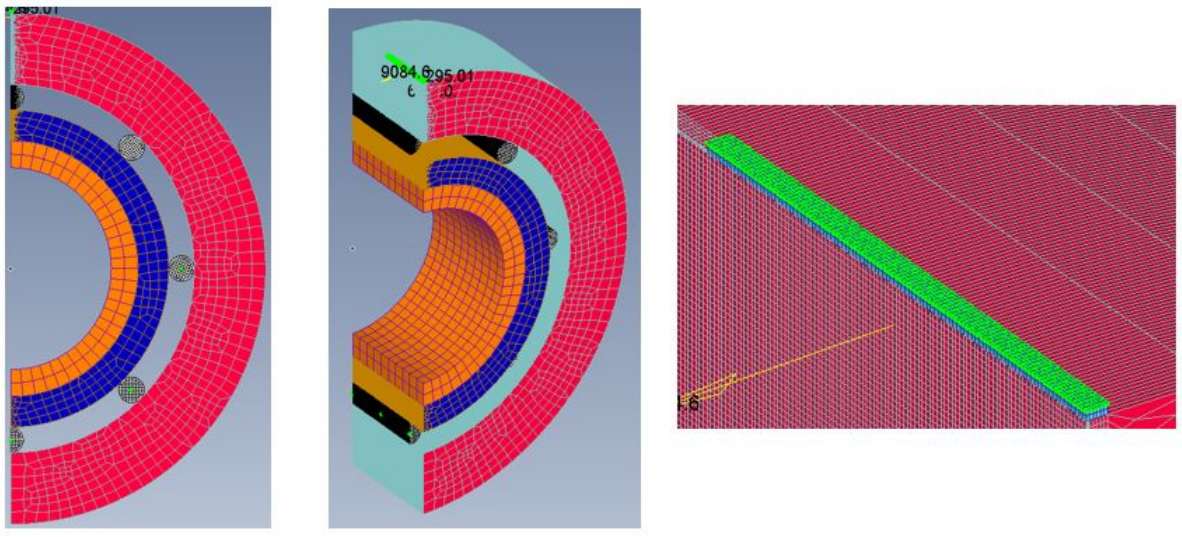

Figure B.4: FEM model of test specimen to determine the contact stress, (left) front view bearing model; colors represents bearing parts, (center) isometric view of model and (right) fixed plate geometry

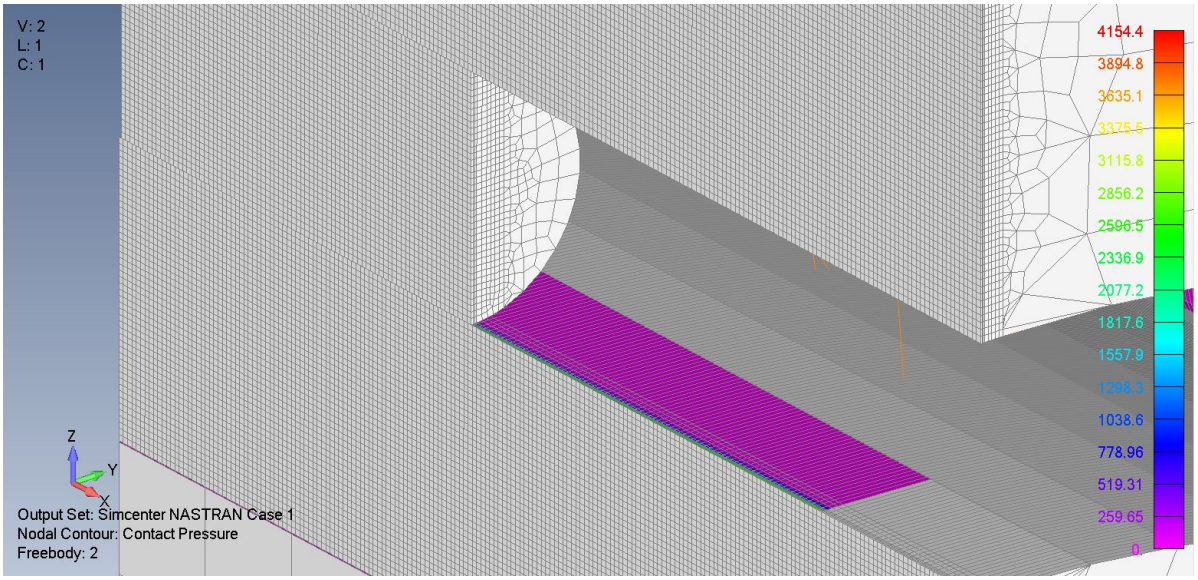

Figure B.5: Results of FEA contact stress on the inner ring of the bearing

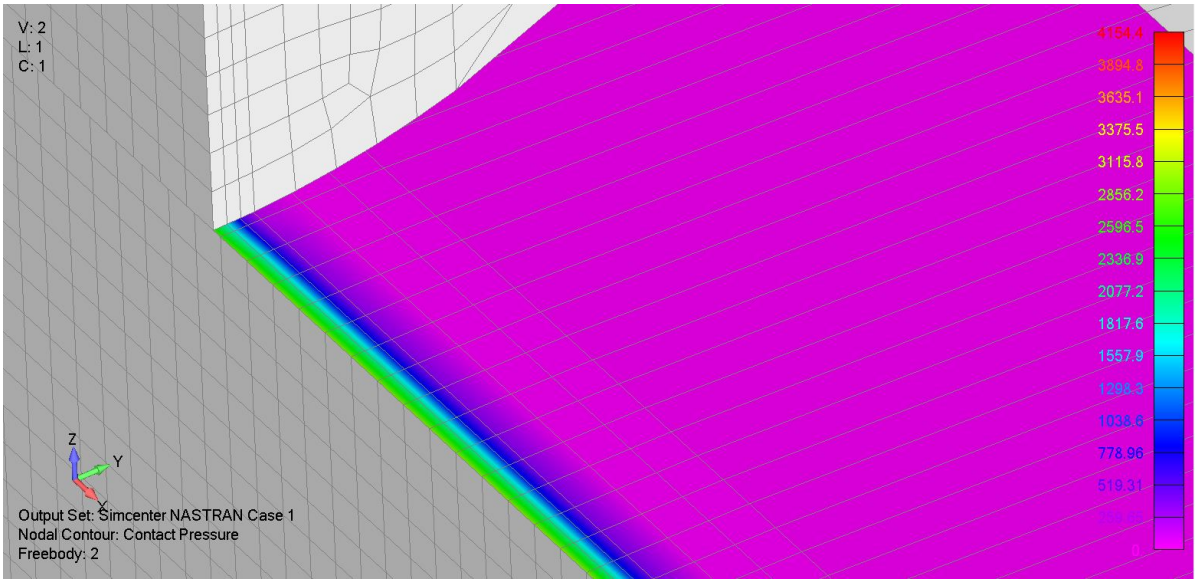

Figure B.6: Results of FEA contact stress on the inner ring of the bearing, zoomed in picture of figure B.5

In this FEM model, a 8-node hexagonal element was used with element size of 0.75mm x 0.20 mm. A linear elastic model with Young's modulus of 210,000 MPa and Poisson ratio of 0.3 was used. The orange colored part is is the modelled shaft which can freely move. The load is applied on the inner surface of the shaft which pushes in positive z-direction against the green colored plate. The plate has been constraint in all translational directions. The dark blue colored part represents the inner ring. The bearing geometry has been symmetrically cutted in 4 pieces for the sake of computational efficiency. Contact connections were applied between the outer surface of the shaft and inner surface of the inner ring and roller and raceways. The contact properties consisted of zero friction and only penetration restricted.

Appendix C

Additional results of data processing

C.1 Histograms contamination test results

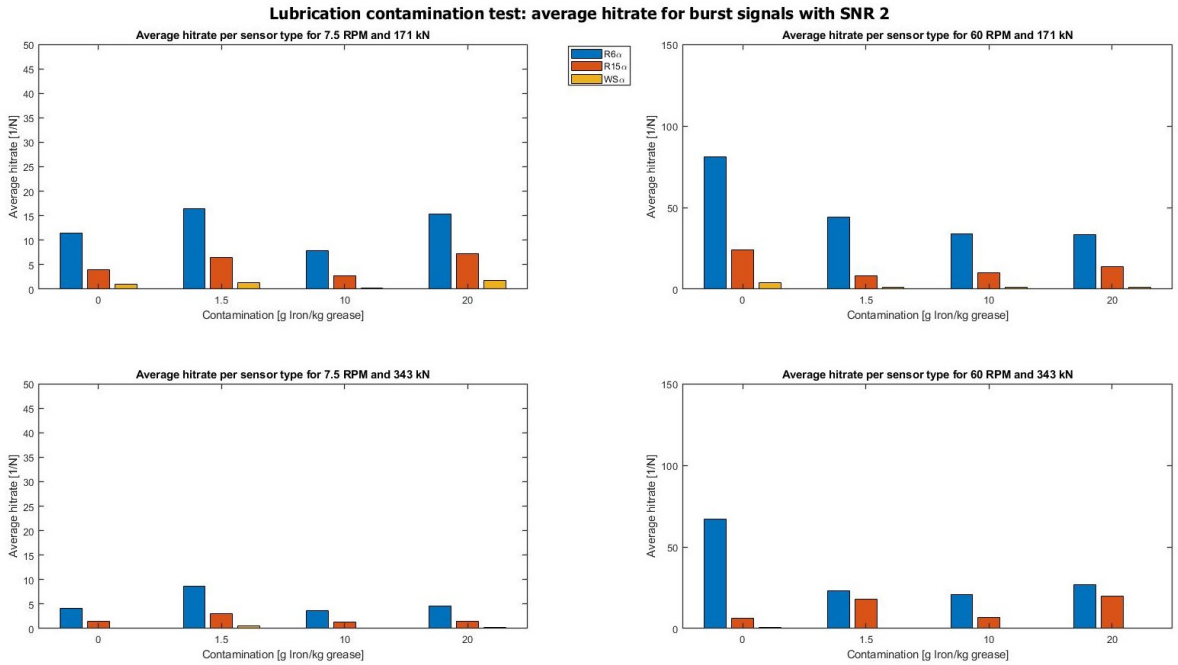

Figure C.1: Lubrication contamination test: hitrates of burst type signals for SNR 2

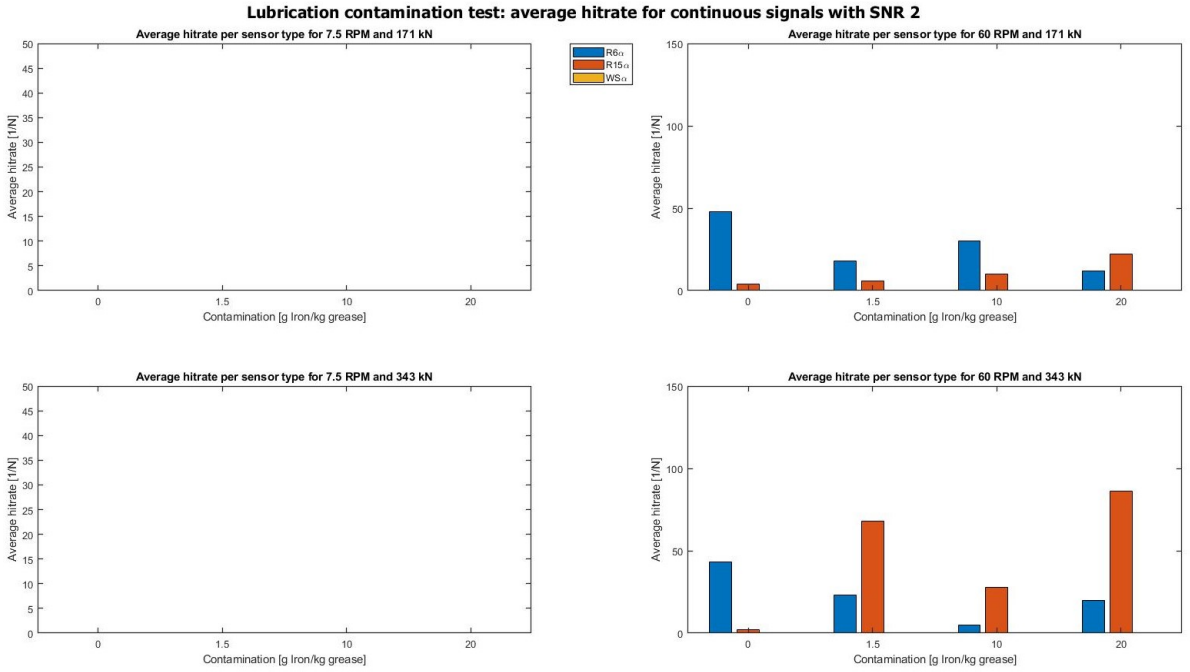

Figure C.2: Lubrication contamination test: hitrates of continuous type signals for SNR 2

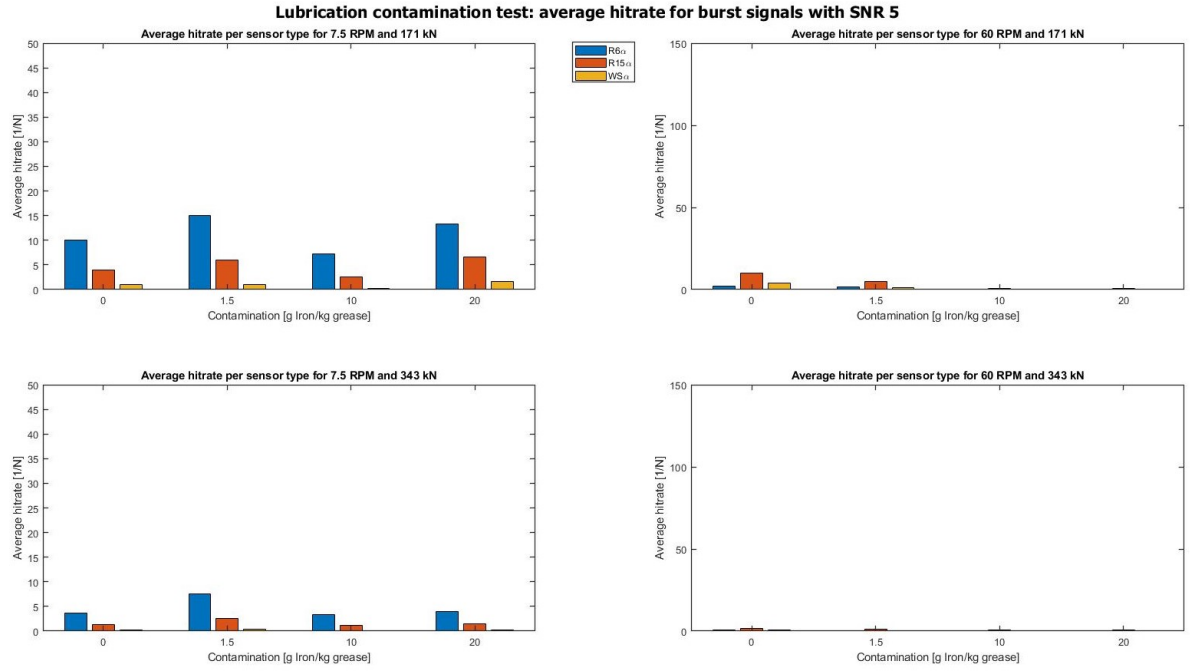

Figure C.3: Lubrication contamination test: hitrates of burst type signals for SNR 5

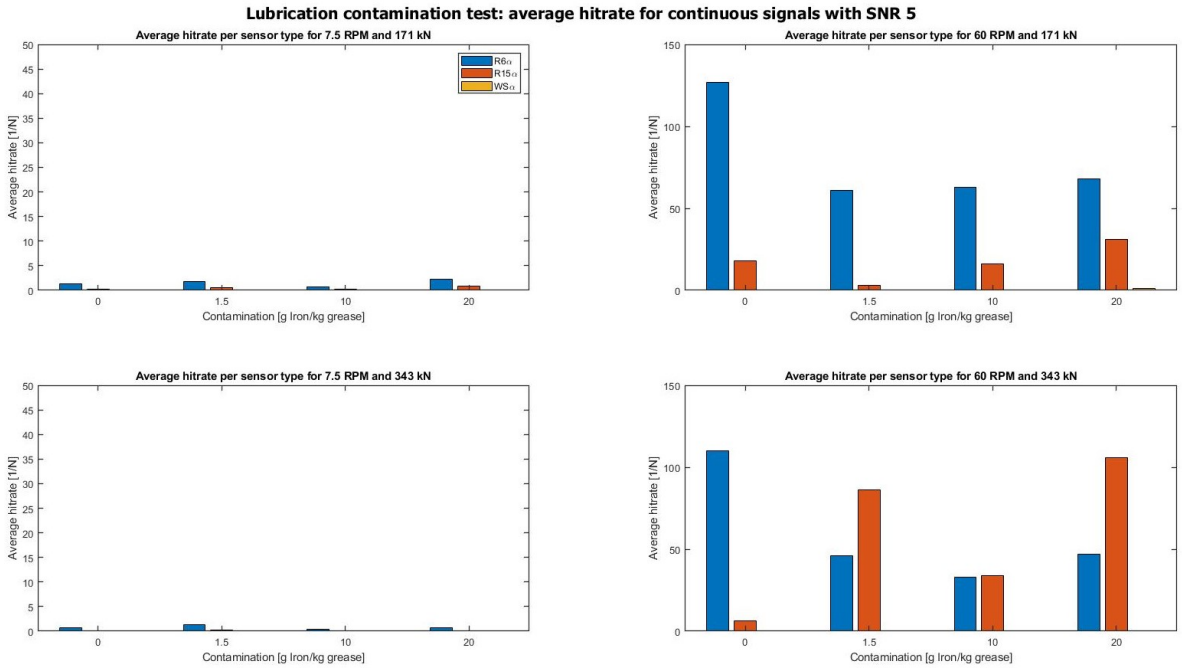

Figure C.4: Lubrication contamination test: hitrates of continuous type signals for SNR 5